UNIVERSITÀ
degli STUDI
di CATANIA

Dipartimento
di Fisica
e Astronomia
"Ettore Majorana"

PhD programme in physics

Tommaso Fazio

Multi-scale study of point-defects induced spin and electron states in wide band gap semiconductors and Perspectives for Quantum Technologies

PhD thesis

Supervisors:
Chiar.ma Prof.ssa E. Paladino
Dr. A. La Magna

Co-Supervisor:
Dr. I. Deretzis

---

academic year 2022/2023

Contents

Abstract

Our main focus is the analysis of point-defects in Wide Band Gap semiconductors. We first study them from first principles through the use of *ab initio* methods based on Density Functional Theory, and then utilize other means of analysis for finding possible applications in the realm of nanoelectronics (defect-free Al_2O_3/AlGaN capacitors) or Quantum Technologies (point-defects in 4H- and 3C-SiC having a large decoherence time). E.g., after a defect's model Hamiltonian *ab initio* calibration, we shed light on the coherent dynamics of such systems (in the bulk or confined in 3D nanostructures). The defects' atomic structures are well-characterized and optimized during the calibration phase by using the Quantum Espresso code. Silicon Carbide and Gallium Nitride are the Wide Band Gap semiconductors we study from the point of view of Quantum Technologies and nanoelectronics, respectively. For what concerns nanoelectronics, we examine the deleterious effect Frenkel defects could play in Al_2O_3/AlGaN junctions. Al_2O_3/AlGaN Metal Oxide Semiconductor capacitors show a hysteretic behavior in their Capacitance vs Voltage characteristics, often attributed to near-interface traps deriving from defects within the oxide layer. The origin as well as the structural/electronic properties of such defects are still strongly debated in the literature. In our research we use *ab initio* molecular dynamics and the climbing-image nudged elastic band method to show that Aluminum

Frenkel defects give rise to bistable trap states in disordered and stoichiometric Al_2O_3. Based on these results, we propose a calibrated polaron model representing a distribution of individually interacting energy levels with an internal reconfiguration mode and coupled to continuous bands of carriers to explain the hysteresis mechanism in Al_2O_3/AlGaN capacitors. As for Quantum Technology, we propose a defect whose experimental identification is yet to be accomplished, i.e. the neutral silicon vacancy in 3C-SiC. We study the silicon vacancy (V_{Si}) in 3C-SiC as a promising color center, modeling it as an electron spin (behaving as a qubit in appropriate conditions) magnetically interacting with the SiC nuclear spin bath containing ^{29}Si and ^{13}C nuclei in their natural isotopic concentration. We calculate the energetics of the neutral and charged V_{Si} with ab initio methods, identifying its neutral charge state as the most favorable for p-doped 3C-SiC systems. Magnetic properties are calculated as well for the V_{Si}^0 in 3C- and 4H-SiC, both in the k and h crystal sites, and the results are compared. We thereby evaluate the Free Induction Decay and the Hahn-echo sequence of control pulses on the electron spin interacting with the nuclear spin bath. We shed light on the Electron Spin Echo Envelope Modulation phenomenon and the decoherence effect by means of the Cluster Correlation Expansion theory. We find a non-exponential coherence decay, which is a typical feature of solid-state qubits. We extend the outlined analysis to silicon vacancies in different 3C-SiC nanoparticles for Quantum Sensing applications. We apply the Hahn-echo sequence to the electron spin interacting with the nuclear spin bath and use the Cluster Correlation Expansion theory (by assumption) to calculate the coherence of the total system. We analyze several nanoparticle shapes as environments for the qubit. We apply the thermodynamic Wulff construction, both the original and the modified one, to determine the proper 3C-SiC nanoparticle shape in thermodynamic equilibrium and after a particular growth process has been followed, respectively. We modify Masullo's Kinetic Crystal Shape until we find two

visibly different structures. Furthermore, we show that in a pyramidal nanoparticle the qubit behaves differently far from the tip as opposed to near it. We find that the qubit within the most peaked nanoparticles is more sensitive to the bath configuration with respect to the other shapes.

Introduction

During the three years of PhD research activity our main focus has been the analysis of point-defects in Wide Band Gap (WBG) semiconductors, at first studied from first principles through the use of *ab initio* methods based on Density Functional Theory (DFT), for applications in the realm of Quantum Technologies (QT). Ours is a study that starting from accurate first-principle calculations allows to obtain those Hamiltonian parameters that are necessary in order to shed light on the dynamics of systems based on WBG semiconductors, whose behavior deviates from the ideal due to the presence of point-defects (in the bulk or confined in 3D nanostructures). The defects' atomic structures are well-characterized by using DFT. Among the most technology-friendly WBG semiconductors we find silicon carbide and gallium nitride, which are the ones we have studied in our research.

Silicon carbide (SiC) is widely recognized as an interesting material for technological applications, also due to its capacity to work in harsh environments under high temperatures, yielding faster switching speeds, lower power losses and higher blocking voltages with respect to silicon [1]. Within this context, SiC-based architectures have been already used as shields in accelerators [2], power devices in electronics [3] and quantum sensors of magnetic fields and temperature gradients [4]. The latter is just one of a number of different and emerging applications for

SiC, which regard its use in QT and manifest themselves in devices at scales and having properties that differ from their electronic technology counterparts. Here, color centers generated by point-like defective configurations like divacancies or Si/C vacancies (V_{Si} or V_C) can provide the active states in which quantum information is encoded, processed and stored. Out of the many SiC polytypes, where the difference lies in the structure of the stacking layers, the most studied are the hexagonal 4H- and 6H-SiC [5] ones, due to the significant progress made in their epitaxial growth and the availability of high-quality samples. On the other hand, the cubic 3C-SiC polytype could potentially be an interesting and convenient alternative due to the possibility to be heteroepitaxially grown on silicon substrates, along with a series of physical characteristics which are appealing for electronic devices (lower band gap, absence of deep level stacking-fault defect states, higher electron and hole mobilities, etc.) [6, 7]. However, the low quality of 3C-SiC crystals during the past has largely hindered its technological use and slowed down its further theoretical study. Recently though, the fabrication techniques and the control of defectivity for cubic 3C-SiC during growth processes have been greatly enhanced [7, 8]. Consequently, QT driven investigations dedicated to 3C-SiC based systems could raise an increasing interest in the near future.

On the other hand, gallium nitride (GaN) has huge applications in electronics, in particular in the vast field of metal-GaN contact technology [9]. Moreover, the stability of GaN's electronic properties to extreme temperature environments allows for its use within microelectronic devices in fields as diverse as aerospace, military, automotive and deep-well drilling [10]. Finally, GaN and its variants find proficient use in the Metal-Oxide-Semiconductor (MOS) industry [11], for instance in Al_2O_3/AlGaN MOS capacitors [12] (to which a thesis chapter is dedicated).

Up to now two distinct application realms are emerging in this Introduction, which are nanoelectronic technology and quantum technology.

The consequent contrast between different but related viewpoints constitutes a constant theme throughout the thesis, being an important part of our research activity. The two pathways within technology-driven efforts certainly present similarities and differences. In both of them, e.g., point-defects are fundamental actors in any conversation regarding their technological applications. However, although in nanoelectronics defects are viewed as challenges to overcome in that they induce anomalies in nanodevices' behavior [13, 12] (Chapter 2), in the quantum domain defects are considered as opportunities [14] (Chapters 3 and 4). In particular, the understanding of dynamic behavior in the quantum states of the defect and the controlled generation (in both type and location) of defects opens up a number of perspectives in the QT field [15, 16]. In both approaches the *ab initio* calculations and the defect plus environment model Hamiltonian derivation are similar. On the other hand, the interest in QT for the defect's coherent evolution makes them differ when dealing with the defect's out-of-equilibrium kinetics (stationary and bias-induced in nanoelectronics, while being protocol-induced in QT).

For what concerns the field of nanoelectronics, the first types of defects we have analyzed are present for instance in metals, i.e. Frenkel defects [17]. These in general could be formed by electronic excitation in amorphous SiO_2 [18]. In our case, we are interested to their formation in Al_2O_3/AlGaN junctions and to the corresponding consequences of inserting such defected junctions in a MOS device. Taking a step back, it is known in the literature that there is an hysteresis behavior in Al_2O_3/AlGaN MOS devices' Capacitance-Voltage (C-V) characteristics [19]. What we were able to show is that the hysteretic behavior is due to Al Frenkel defects in Al_2O_3. These give rise to bistable trap states in disordered and stoichiometric Al_2O_3. Furthermore, we proposed a calibrated polaron model in which there is a distribution of individually interacting energy levels having an internal reconfiguration mode. These energy levels are coupled to continuous bands of carriers to explain the

hysteresis mechanism in Al_2O_3/AlGaN capacitors. As anticipated above, in this case defects are detrimental to the correct functioning of MOS devices in that they cancel the expected monotonous nature of CV characteristics through hysteresis. This work is published in the Journal of Applied Physics [12].

On the other hand, in the QT field our research theoretically focused on point-defects in 4H- and 3C-SiC having a low rate of quantum information loss [20, 15], even at room temperature [21]. In particular, we have considered the neutral and charged silicon vacancies (V_{Si}^{0}, V_{Si}^{-1} and V_{Si}^{-2}) magnetically interacting with the SiC nuclear spin bath, constituted by naturally occurring ^{29}Si and ^{13}C paramagnetic nuclei. Such system can be optically driven for coherent control purposes [4]. Furthermore, its energetics [22] and hyperfine interaction [23] properties can be calculated via *ab initio* methods based on DFT. We note here that the silicon vacancy in its neutral state has been experimentally verified in 3C-SiC [24], but has received no attention in the theoretical literature. In 3C-SiC only the V_{Si}^{-1} defect has been addressed [25, 26]. The V_{Si} center, in its neutral charge configuration, can be modeled as a spin-1 defect that evolves in the magnetic environment constituted by the spin-1/2 nuclear spin bath around it. Highly transition-selective microwave control pulses [5] can be used to effectively reduce the three electron spin's eigenstates to two in the resulting dynamics, so that it can be considered as a qubit. Therefore, from now on (especially in Chapters 3 and 4) we consider qubit and electron spin as interchangeable words.

The nuclear spin bath induces noise at low frequencies for the point-defect. This is typically the case in Nuclear Magnetic Resonance (NMR), where the interesting experimental signal is generated by nonequilibrium electron spin magnetization (equivalent to its coherence) precessing about an external magnetic field [27]. Due to the spatial field inhomogeneity, the measured signal in a Free-Induction Decay (FID) process is defocused and displays a characteristic non-exponential decay resulting

in inhomogeneous broadening of the spectral lines. Analogous effects occur in solid-state implementations of qubits and originate from time-inhomogeneities due to repetitions of measurement protocols [28, 29, 30]. The same happens when the degree of freedom of the examined system is electronic in nature, as opposed to nuclear. This is the case in Electron Paramagnetic Resonance (EPR), in which one applies NMR techniques to an electron spin [31]. One way of refocusing can be achieved by the Hahn-echo sequence, an established technique applied recently to investigate the residual decoherence of divacancy defects in 4H-SiC in ref. [20]. In Chapter 3 we consider both the FID and Hahn-echo sequences applied to the considered defect (in the bulk of 3C-SiC) by utilizing the Cluster Correlation Expansion (CCE) theory [32]. CCE theory allows to split the bath in clusters with a given number of interacting nuclear spins. Since the clusters by hypothesis are *uncorrelated* with each other, the qubit coherence is obtained as a product of the contributions of each cluster. Part of this work is published in the Materials Science Forum journal [15] and a preprint of the other part is on the arXiv [16].

At this point, the next step (Chapter 4) for us has been the application of all this analysis machinery to various defected 3C-SiC nanoparticles coming in different shapes for sensing applications, as opposed to the bulk material to which Chapter 3 is dedicated. In particular, SiC nanodevices have been used in the literature for sensing [33, 34]. However, to the best of our knowledge, no one has ever used the defect's sensitivity to the nuclear spin bath configuration for sensing applications in 3C-SiC. The idea is to exploit this sensitivity and to examine different somewhat sharp nanoparticle shapes in order to see which one of them has the stronger response to the environment configuration, for applications in Atomic Force Microscopy (AFM). Since the defect magnetically interacts only with the paramagnetic nuclei possessing a non-zero nuclear spin, this theoretical analysis could be used to devise experiments whose objective is the measurement of the paramagnetic nuclei concen-

tration in a given material. Although the application of CCE theory to a defect in a nanoparticle is somewhat speculative, a bit of initial support, to be confirmed by theoretically/computationally experimenting with it, comes from the theory's high convergence property with respect to small baths [32] (see Chapters 3 and 4). For what concerns the nanoparticle shapes, there are various ways to obtain them in the literature [35, 36]. First we proceeded to simulate the behavior of the nanoparticle shape in thermodynamic equilibrium, obtained through the thermodynamic Wulff construction [37, 38]. This is the reference for an ideal preparation process which tends to stabilize the thermodynamic shape of a given object. Then we examined three nanoparticles whose shape is the result of kinetic effects accumulated during their growth. For the first one we have put ourselves in the same growth conditions as Masullo et al. [39], whereas for the two remaining we have modified these conditions until a visibly different shape has been reached (see Chapter 4 for details). Growth processes giving rise to kinetic crystal shapes are usually Chemical Vapor Deposition [40] (CVD) and Physical Vapor Deposition [41] (PVD). Finally, we have studied a pyramidal 3C-SiC nanoparticle, i.e. the simplest shape for the tip of the microscope in an AFM experiment. This could be obtained through attachment processes [42]. The calculation of the decoherence time associated to the defect in each nanoparticle allowed us to establish which nanoparticle shape is more suitable to be used for sensing. This part of our work is in its preliminary form and once it will be mature enough we will submit it to a QT journal.

The results we have obtained during my PhD are listed in the following. We have calculated the energetic and magnetic properties of the various defects with *ab initio* methods based on DFT in Chapter 1. The Car-Parrinello molecular dynamics and the nudged elastic band method have been used to calculate energetic and electronic properties of Aluminum Frenkel defects in Al_2O_3/AlGaN junctions. Moreover, moving on to the analysis of defects in SiC, we identify the neutral charge state of

the silicon vacancy as the most favorable one for p-doped 3C-SiC systems [15, 16]. We have compared these parameters with the same for a neutral V_{Si} in 4H-SiC, both in k and h site, for gaining insight into the intrinsic geometric and structural differences between the two SiC polytypes. Our results on the hyperfine tensor components show significant deviation with respect to the semiclassical estimates of the model parameters, whereas the results on the Zero-Field Splitting (ZFS) tensor components are not present in the literature. These magnetic parameters are what we need to calibrate the system's Hamiltonian. Then, in Chapter 2 we show that Aluminum Frenkel defects may form bistable centers that can act as traps of electrical charges in disordered and stoichiometric α-Al_2O_3. Furthermore, the application of a polaronic model representing a distribution of individually interacting energy levels with an internal reconfiguration mode and coupled to continuous bands of carriers has shown that such trap states can explain the hysteresis mechanism in the CV measurements of Al_2O_3/AlGaN capacitors. We acknowledge that this bistable-hysteretic behavior can emerge from different types of oxide defects, whose experimental and theoretical investigation could enhance the understanding of MOS devices based on the Al_2O_3 gate dielectric [12]. In Chapter 3 we have evaluated the Free Induction Decay and the Hahn-echo sequence on the electron spin (V_{Si}) interacting with the nuclear spin bath in 3C-SiC. Here, the Electron Spin Echo Envelope Modulation phenomenon, due to single nuclear spin flipping processes, and the overall qubit coherence decay (or decoherence) are highlighted in the context of CCE theory. We have obtained estimates for the qubit's decoherence time in the FID and Hahn-echo cases. Furthermore, we have found a non-exponential coherence decay, which is a typical feature of solid-state qubits subjected to low frequency 1/f-type noise from the environment [16]. Finally, for what concerns the defected 3C-SiC nanoparticles (Chapter 4), our results suggest the use of nanoparticles with sharp tips, the sharpest being the pyramidal one, for sensing of paramagnetic

nuclear spins' properties.

The rest of the PhD thesis is organized as follows: in Chapter 1 we introduce the *ab initio* methods we have used, the corresponding results and the relevant literature. After an Introduction, in Section 1.2 we report the calculations associated to the Frenkel defects in α-Al_2O_3, whereas in Section 1.3 we do the same for neutral and charged V_{Si} in 4H- and 3C-SiC. In Chapter 2 our work on Frenkel defects causing hysteretic behavior in Al_2O_3/AlGaN capacitors is resumed starting where we left in Section 1.2. After an Introduction (Section 2.1), in Section 2.2 the polaron theory is laid out, which is then applied in Section 2.3 to model Frenkel defects by substituting in it our *ab initio* calibrated parameters regarding the structural properties of the defects. At the end, in Section 2.4 a final discussion is provided. In Chapter 3 we report our results on the coherence function calculated by using CCE theory, starting from where we left in Section 1.3. Here, based on the system's parameters derived via *ab initio* methods, we calculate both analytically and numerically the spin coherence after free evolution and under the Hahn-echo sequence in Section 3.2, at first and second order of the CCE expansion. Finally, in Chapter 4 our results on the topic of sensing via a defected 3C-SiC nanoparticle can be found, with an Introduction in Section 4.1. The full framework of the thermodynamic Wulff construction is applied in Section 4.2, both at equilibrium and accounting for kinetic effects. A pyramidal shape is studied in Section 4.3. At the end (Section 4.4), our conclusions and ideas for further work are discussed.

Chapter 1

Ab initio methods based on DFT

1.1 Introduction

In this first chapter our calculations from first-principles (or *ab initio*) on different kinds of point-defects in both the oxide layer (Al_2O_3) in GaN-based MOS devices (Section 1.2) and SiC (Section 1.3) can be found. These calculations are based on Density Functional Theory.

DFT is one of the most widely used methods for ab initio calculations of the structure of atoms, molecules, crystals, surfaces, and their interactions [43]. In order to obtain valuable information on the electronic, structural and energetic properties of such systems one has to solve the many-body Schroedinger equation. Due to the practical unfeasibility of the task, DFT has been developed on the basis of the Hohenberg-Kohn theorems [44]. Furthermore, its most known and utilized implementation, the Kohn-Sham equations, was introduced soon thereafter [45]. Although until this point the treatment is exact, it turned out that in order to perform practical calculations one of the functionals being the cornerstone of the theory, the exchange-correlation (xc) one, must be treated in an approximate form. Various approximation schemes have been introduced in the literature, the Local Density Approximation [46] (LDA) and

the Generalized Gradient Approximation [47] (GGA) being two of them. Therefore, as any approximate method, DFT has some issues. Most notably, its most known implementation is merely a ground state theory and is not able to predict the correct band gap for insulators and semiconductors [48]. Attempts can be found in the literature that deal with those issues [49, 50]. However, for what we are interested in the ordinary Kohn-Sham equations are more than enough.

As a matter of fact, DFT allows one to perform atomistic simulations at the molecular [51] and solid-state [52] level. That is the reason why a number of codes implementing DFT has been developed during the last decades, like the Density Functional based Tight-Binding (DFTB+) [53], the Vienna Ab initio Simulation Package (VASP) [54] and Quantum Espresso (QE) [22]. Whereas DFTB+ is derived from a simplification of Kohn–Sham DFT to a tight binding form, VASP and QE are proper ab initio implementations of Kohn-Sham DFT in that they work on the actual geometric structure of molecules and solids. In order to use DFT for practical calculations on real systems, one needs to solve the Kohn-Sham equations numerically with a computer, which means that the equations must be discretized as a finite size problem. Furthermore, it is advantageous to cast the problem in a way that is computationally efficient, and that allows the numerical accuracy to be controlled in a sensible way. These codes ensure that by using the so-called plane wave pseudopotential approach. This involves using a plane wave basis set to represent the orbitals, and pseudopotentials to represent the nuclei and core electrons. There are various different pseudopotentials to choose from, like ultrasoft [55], norm-conserving [56] and projector augmented-wave [57] ones, offering a smooth version of the nuclei and core electrons wave functions, which do not actively enter the given system's dynamics. Each of them gives a certain advantage over the others that is preferable in some contexts and not in others (cfr. Chapters 2 and 3). Alternative approaches to the plane wave pseudopotential exist. These involve using

basis functions that are localised around individual atoms [58, 59]. While computationally cheaper, they suffer from the problem that the basis set is incomplete, thereby giving rise to convergence issues with respect to the basis. Out of the many DFT ab initio codes available, during the PhD we have focused on the use of QE.

The free and open-source QE code is mainly used to calculate energetics, band structure, structural relaxation and density of states properties of molecules and solids [22]. Some less frequent calculations allowed with QE are the ones involving thermo-mechanical properties [60], and others made possible via the inclusion of advanced capabilities within the code [61] and/or improved treatment of exact exchange [62].

The rest of the chapter unfolds in the following way: in Section 1.2 we present the calculations associated to the Frenkel defects in α-Al_2O_3. Information about the Car-Parrinello molecular dynamics simulations of such defects can be found in Subsection 1.2.1. In Subsections 1.2.2 and 1.2.3 we describe the calculation scheme used to obtain the system's electronic properties during the dynamics and the transition states between stable and metastable defect configurations, respectively. Then, in Section 1.3 we do the same for neutral and charged V_{Si} in 4H- and 3C-SiC. The model of V_{Si} interacting with a nuclear spin bath, the model parameters and their convergence properties, their calculation via *ab initio* methods and the techniques used to control these kinds of defects are introduced in the corresponding subsections. We note here that in the context of ab initio calculations (and in QE in particular) convergence is achieved as a consequence of the self-consistent field method at a given iteration giving a result that differs from the one at the previous iteration by less than 10^{-4}, at which point the simulation stops running.

1.2 Frenkel defects in α-Al_2O_3

In nanoelectronics, one of the most utilized dielectrics in order to control devices' electrostatics is Al_2O_3. Usually inserted in junctions containing III-V semiconductors, it is employed to reduce losses of current and in general for its excellent mechanical and chemical features [63]. On the flip side, Al_2O_3 in Al_2O_3/AlGaN junctions causes hysteretic behavior in MOS capacitors [64, 65, 66, 67, 68], thereby undermining the device's electronic properties. This is usually the result of bistable defects effectively behaving as charge traps [65] in the oxide layer (near the interface between Al_2O_3 and AlGaN), whose state can be switched by applying a gate voltage. We want to get rid of these types of defects in order to improve the devices' performance in the nanoelectronics industry, as we will see shortly.

Our main objective is to shed light on the structural and electronic properties of Al_2O_3, in order to single out the defect causing the peculiar charging effect in Al_2O_3/AlGaN junctions. To this end, we initially set up an undefected Al_2O_3 supercell to which we apply high temperature annealing through Car-Parrinello [69] molecular dynamics (CPMD) to create structural defects. We select the α polytype of Al_2O_3 for our simulated supercell, owing to its low formation energy and proclivity to form homogeneous films [70] (as opposed to γ-Al_2O_3 displaying unsurmountable problems with grain size [71]). Our calculations show that stoichiometric Al_2O_3, under the conditions in our simulations, forms Al Frenkel defects, which are pairs of Al vacancies and Al-Al interstitials. They also manifest a bistable energy level configuration under our chosen charging conditions (more on this topic in Chapter 2).

1.2.1 Car-Parrinello molecular dynamics

The Car-Parrinello method is extremely important in that it allows one to perform molecular dynamics simulations in a feasible way by computing

interaction potentials as two-component classical interactions [72]. Describing molecular interactions as classical processes is indeed a good approximation giving accurate results for the system's dynamics. Furthermore, it is a flexible approach that can be expanded in order to be used in path integral molecular dynamics [73] and for describing nonadiabatic molecular processes [74]. A natural pseudopotential to be used within the Car-Parrinello method is the ultrasoft one [75], which we have used abundantly in our research.

We used Car-Parrinello [69] molecular dynamics (CPMD) to study the formation of the defect in stoichiometric Al_2O_3 and its kinetic properties. We set up a trigonal α-Al_2O_3 $3 \times 3 \times 3$ supercell containing 270 atoms, whose space group is $R\bar{3}c$, for the *ab initio* calculations (see Fig. 1.1a). The simulations were performed by utilizing the PBE implementation [47] of the generalized gradient approximation for the description of the exchange-correlation functional. We used ultrasoft pseudopotentials to model the core electrons [76], whereas we chose the kinetic energy and the augmented charge density cutoffs to be 47 Ry and 323 Ry, respectively. We performed the simulations within the canonical ensemble, fixing the target temperature by means of a Nose thermostat [77]. We followed the dynamics for a total of 22.26 ps in steps of $\sim$ 0.1 fs through the Verlet algorithm [78]. During the time of the simulation we let the atoms and lattice parameters freely move without constraints. For convenience the effective mass of electrons was fixed to 100 a.u., while the mass of ions was set to its real value. Initially we made the system relax for $\sim$ 4 ps at 300 K, and after that we subjected it to temperature annealing in steps of 250 K until T $\sim$ 3300 K was reached (see Fig. 1.1c). Finally, after this first annealing period and an ultrafast quenching at 300 K took place, the system underwent a second annealing up to a temperature of 1050 K.

1.2.2 Electronic properties

We calculated the electronic features of defects formed during the temperature annealing period of the CPMD simulation in an α-Al_2O_3 $3 \times 3 \times 3$ supercell by means of *ab initio* methods based on DFT, using the already described setup. Structural relaxation towards the energy minimum was carried out by utilizing the PBE functional [47] on a $2 \times 2 \times 2$ Monkhorst-Pack grid [79]. After that, we evaluated the total energy of the relaxed atomic structure in order to calculate the electronic levels by means of the hybrid PBE0 functional [80, 81], with an exchange fraction of 0.25, to gain a more precise value of the α-Al_2O_3 band gap. We reached convergence through a Γ-point sampling of the Brillouin zone.

1.2.3 Nudged elastic band method

The nudged elastic band (NEB) is a useful method allowing to find saddle points and minimum energy paths within reactants and products [82]. It is an optimization method finding the intermediate images along the reaction path. The images that are found constitute the lowest energy images possible while maintaining equal spacing between each other. Furthermore, the method can be generalized to determine reaction pathways for transformations from solid to solid, including both atomic and unit-cell degrees of freedom. The combination of atomic and cell degrees of freedom makes the reaction paths insensitive to the choice of periodic cell [83].

However, we employed a slightly modified approach called the climbing image nudged elastic band method [84] to calculate the transition states between stable and metastable defect configurations. The main modification consists in one of the images climbing up along the elastic band to converge exactly to the highest saddle point. Moreover, by utilizing variable spring constants it is possible to increase the density of images near the top of the energy barrier, thus obtaining an improved

version of the reaction coordinate at the saddle point. In the process, we considered two defect charge states with electron concentrations of $n = 0$ and $n = 7.97 \times 10^{20}$ cm^{-3} (equivalent to 2 electrons per supercell, an extremely high doping that is feasible whenever the supply is a MOS device). Convergence was reached through a $2 \times 2 \times 2$ sampling of the Brillouin zone and a PBE exchange-correlation functional [47] was used in the calculations. QE was utilized for all simulations in this chapter [22].

1.2.4 Results

By following the *ab initio* calculation scheme outlined in the previous subsections, we are able to simulate the annealing process and demonstrate the consequent formation of Frenkel defects in the oxide layer of an Al_2O_3/AlGaN capacitor. The results of our calculations are thus reported in the remainder of this subsection.

It is known in the literature that hysteresis is a frequent challenge to overcome in AlGaN-based microelectronic devices [64, 65, 66, 67, 68], since it compromises operational balance in forward and reverse bias regimes. For instance, Fig. 1.1b shows C-V measurements performed on Al_2O_3 films deposited by Plasma Enhanced ALD onto AlGaN/GaN heterostructures (see ref. [64] for experimental details). In our system, modifying the gate bias from negative values towards the accumulation regime and backwards generates hysteresis, which is linked to trapped charges in the Al_2O_3 layer. The hysteretic behavior remains at high temperatures ($\sim$ 100 °C), creating a persistent positive shift in the C-V characteristics of transistors with high electron mobility [85]. Our objective is thus to identify those defects in stoichiometric Al_2O_3 that are responsible for this electrical behavior. We identify two steps in the Al_2O_3/AlGaN/GaN system's C-V curves. The first step at a negative bias is caused by the depletion of the two-dimensional electron gas at the AlGaN/GaN interface. The second step is instead located in the positive part of the gate bias

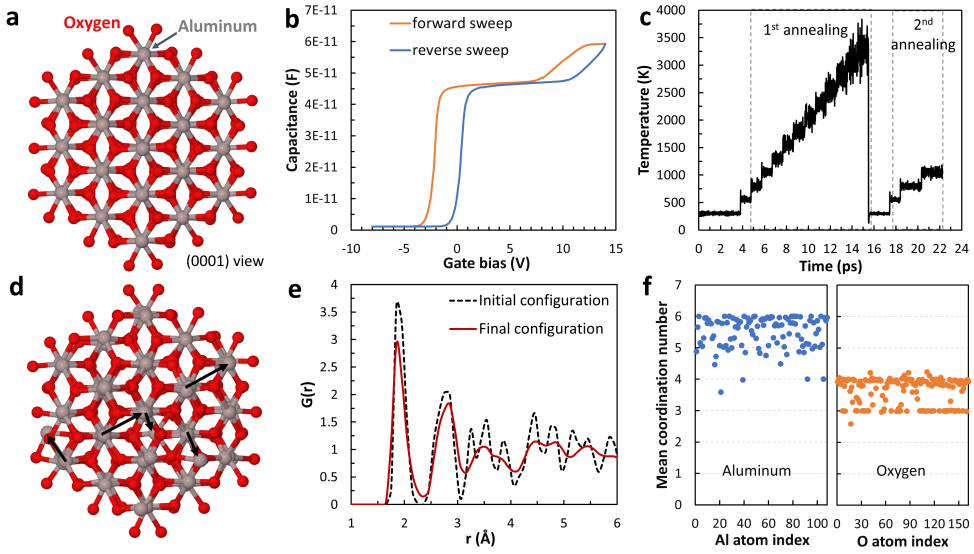

Figure 1.1: (a) Scheme of the α-Al_2O_3 supercell used in the CPMD simulations. (b) Experimental C-V curve in an Al_2O_3/AlGaN/GaN MOS capacitor. (c) Temperature as a function of time for the entire CPMD simulation. (d) Schematic representation of diffusive events and the creation of Al Frenkel defects during the CPMD simulation. (e) Pair correlation function for the initial (dotted line) and the post 1^{st}-annealing configuration at T=300 K. (f) Mean coordination number for all Al (left) and O (right) atoms after the 1^{st} annealing process of the CPMD simulation.

and is due to the charge accumulation at the Al_2O_3/AlGaN interface. In the remainder of the chapter we will focus on theoretically modeling the Al_2O_3/AlGaN interface. In Figure 1.1c it is reported the ultrafast heating process taking place within the CPMD simulations for periodic α-Al_2O_3 supercells containing 270 atoms. The process is simulated by initiating at a temperature of 300 K and going up to temperatures ($\approx$ 3300 K) that are necessary for the first atomic diffusion events to happen, with steps of 250 K per picosecond. Once this phase is over, the system is subjected to a quasi-instantaneous quenching down to room temperature in order to test the stability of the defects formed under thermodynamic conditions, which are similar to those found in experiments. Our results show that this procedure creates a partially defective lattice as opposed to a completely amorphous one, which is coherent with a previous experimental study demonstrating short-range order in amorphous Al_2O_3 [86]. Furthermore, we perform a second annealing procedure at lower temperatures in order to identify bistable configurations in the oxide layer (see below).

We note that after the first thermal annealing period Frenkel defects are formed via diffusive mechanisms exclusively for the Al atoms, demonstrating their capability of reaching local minimum configurations and establishing complex chemical bonds in nonideal Al-O environments. Such finding can be compared with first-principles calculations of known defects in Al_2O_3 in the literature [87, 88], where Al vacancies or interstitials (depending on the relative Fermi level position) appear to have the lowest formation energy among the main point defects in this system. In Fig. 1.1d we show a schematic representation of the diffusive phase associated to the heating process, in which Al cations were often displaced via double diffusive steps from their position along the α-Al_2O_3 [0001] direction to neighboring sites (either Al-rich or O-rich). Results show that a similar diffusive phenomenon does not happen for O atoms within the simulated temporal window. The Al atoms reaching a new position

induce a rearrangements of local bonds, which in turn gives rise to a defective environment that is stable even at room temperature. The radial distribution function of the initial and final crystal structure in thermodynamic equilibrium can be seen in Fig. 1.1e. The distribution function is calculated along the molecular dynamics trajectory for 1 ps at a temperature of 300 K. In the initial state a set of characteristic peaks corresponding to average atomic pair distances is visible (dotted line), where the first peak represents the distribution of neighboring Al-O pairs. The ideal crystalline structure of the α-Al_2O_3 supercell is reflected in the high degree of resolution and sharpness of the aforementioned peaks. After the annealing procedure, the curve (line) retains its qualitative characteristics at least for the first two peaks of the distribution, whereas changes in the others reflect a longer range disorder of the post-annealed structure. In Fig. 1.1f we show the mean atomic coordination for Al and O at the end of the first annealing period in the CPMD simulation. In order to count the neighboring atoms for obtaining the coordination parameter, a cutoff value of 2.25 Å for the Al-O bond was chosen, based on the Car-Parrinello calculation of the pair distribution function. An important thing to note is that while in the ideal α-Al_2O_3 all Al and O atoms have a unique coordination parameter (6 for Al and 4 for O), a reduced one was found at the end of the annealing period (5 and 4 for Al, 3 for O). The presence of 5-coordinated Al and 3-coordinated O is a known fact in the literature [89, 90].

Then we performed a second annealing process at lower temperatures until $T = 1050$ K was reached (see Fig. 1.1c). This way we explored possible bistable configurations in Al Frenkel defects. The second annealing caused partial vacancy-interstitial recombinations, or elimination of Frenkel defects, in particular for 5-coordinated Al atoms. However, 4-coordinated Al interstitials survived the whole simulation process. Furthermore, a single 4-coordinated Al interstitial displayed a bistable behavior by acquiring two distinct local configurations (one stable and one

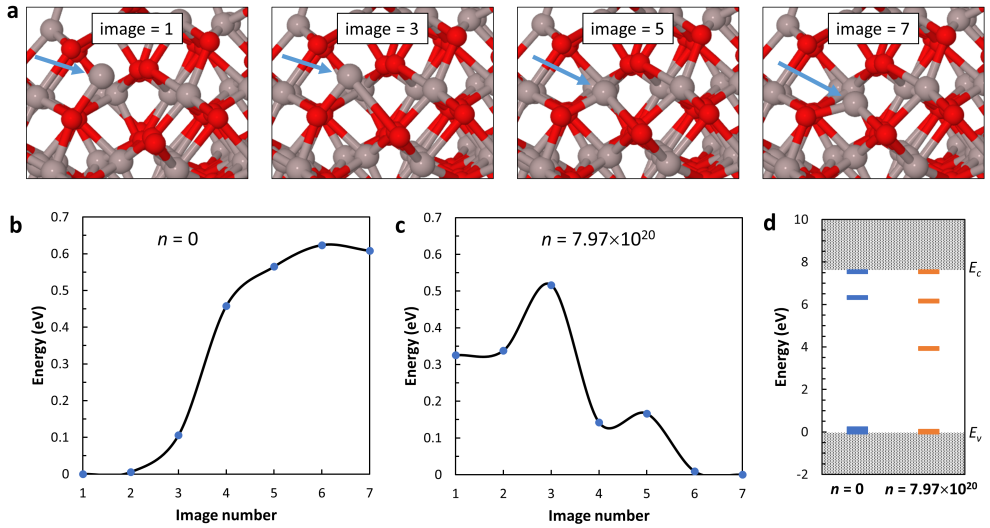

Figure 1.2: (a) Scheme of the minimum energy path between the stable and metastable configurations of a bistable Al Frenkel defect in disordered Al_2O_3. (b) Energy barrier for the transition between the stable and metastable configuration, in the absence of charging. (c) Similar to (b) but for an electron concentration $n = 7.97 \times 10^{20}$ cm^{-3}. (d) Al_2O_3 intragap states for the stable configurations of the bistable Al Frenkel defect at $n = 0$ (corresponding to image 1) and $n = 7.97 \times 10^{20}$ cm^{-3} (corresponding to image 7) at the Γ-point of the Brillouin zone.

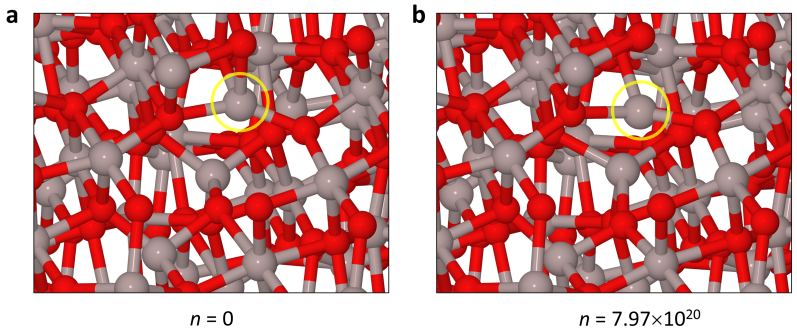

Figure 1.3: Structural configuration of the bistable Al atom corresponding to the last image of the minimum energy path of the NEB calculations (image 7) (a) at $n = 0$ (uncharged) and (b) at $n = 7.97 \times 10^{20}$ cm^{-3} (charged). The strong electron charging induces a structural reconfiguration and a further lowering of the atomic coordination.

metastable, see Fig. 1.2a) during the simulation. From this point forward, we focused on such bistable defect by calculating first the diffusion energy barrier between the stable and metastable configurations via *ab initio* methods and the climbing-image nudged elastic band method [84]. Our calculations show that the energy barrier between the stable configuration and the metastable one (first and last images in Fig. 1.2a, respectively) without charging (see Fig. 1.2b) is equal to 0.62 eV. On the other hand, by applying a strong electron doping $\sim 10^{20}$ cm^{-3} we have witnessed an inversion of the stable and metastable configurations, which are now separated by 0.52 eV (Fig. 1.2c). At this point, an important aspect to note is the significance of the degree of doping in the context of energy mismatch between the stable and metastable configurations, as for lower doping concentrations we did not find visible changes with respect to the undoped scenario. Thus, the formation of bistable Al Frenkel defects and the switching between the two configurations by means of strong electron charging could be the potential cause of hysteretic behavior in the C-V characteristics of Al_2O_3/AlGaN capacitors under gate bias. The electronic properties of both of the defects' stable configurations

were calculated from first principles by utilizing the PBE0 hybrid functional [47, 80, 81], for the two distinct charge conditions (see Fig. 1.2d). For the doped sample a deep level is formed ($\sim$ 3.9 eV from the valence band maximum E_v) as a consequence of the splitting of two levels that are close to E_v. This is due to the Al atom's coordination parameter reduction caused by the excess electrons introduced through doping. This aspect can be more clearly explained by looking at Fig. 1.3, where the last frame of the minimum energy path of the NEB calculation depicting the structural configuration for the two charge states is shown. As can be seen, the coordination parameter of the Al atom forming the Frenkel defect changes from 4 to 3 due to the strong doping. Finally, our computations suggest that, beyond O vacancies [91], also Al defects may give rise to charge traps in amorphous Al_2O_3, along with being subjected to structural rearrangement in case of strong charging upon gate bias.

1.3 V_{Si} in SiC

1.3.1 Model

Ab initio methods based on DFT are important to calculate, among others, the structural, electronic, optical and magnetic properties of molecules and solids [92]. They may be used also to calibrate EPR Hamiltonians associated to electron spins interacting with nuclear spin baths, allowing to calculate, for instance, the hyperfine tensor components [93] and the ZFS tensor components [94]. Our system's Hamiltonian can be written as [4]

$$\mathcal{H} = \mathcal{H}_e + \sum_i \mathbf{S} \cdot \boldsymbol{\mathcal{A}}_i \cdot \mathbf{I}_i - \sum_i \mu_n \mathbf{B} \cdot \mathbf{g}_i \cdot \mathbf{I}_i + \sum_{i<j} \mathbf{I}_i \cdot \boldsymbol{\mathcal{B}}_{ij} \cdot \mathbf{I}_j, \tag{1.3.1}$$

$$\mathcal{H}_e = D\left[S_z^2 - \frac{1}{3}S\left(S+1\right)\right] + E\left(S_x^2 - S_y^2\right) - \mu_e \mathbf{B} \cdot \mathbf{g}_e \cdot \mathbf{S}. \tag{1.3.2}$$

The first term in Eq. 1.3.1 is the electron spin Hamiltonian, which is composed by the ZFS terms (first and second term of Eq. 1.3.2), arising from the magnetic dipolar interaction between multiple unpaired electrons, and the Zeeman interaction with an external applied magnetic field (last term of Eq. 1.3.2). The last three terms of Eq. 1.3.1 (where $i, j = 1, \ldots, N$ indicate the nuclear spin and μ_n is the nuclear magneton) are the magnetic hyperfine interactions between the electron spin and the ^{29}Si and ^{13}C nuclear spins, the Zeeman terms for each nuclear spin and the dipolar interactions between nuclear spins, respectively. From now on, the pure-dephasing approximation [95] is performed on Eq. 1.3.1, so that no transition of the electron spin takes place by exchanging energy with the environment. Our working Hamiltonian is (the choice of putting $E = 0$ is justified in Appendix A) [95]

$$\mathcal{H} = DS_z^2 + \gamma_e B_z S_z + \sum_{i=1}^{N} \gamma_i B_z I_{iz} + S_z \otimes \sum_{i=1}^{N} (A_i I_{iz} + B_i I_{ix}) + \mathcal{H}_{n-n}, \quad (1.3.3)$$

where $\mathcal{H}_{n-n}$ is the last term of Eq. 1.3.1, $A_i \equiv A^i_{zz}$ and $B_i \equiv \sqrt{A^{i2}_{zx} + A^{i2}_{zy}}$, whereas A_{zx}, A_{zy} and A_{zz} are the elements of the third row of the hyperfine tensor. Note that Hamiltonian 1.3.3 commutes with the electron spin S_z operator, so that it can be expressed in the spin operator eigenbasis $\{|1\rangle, |0\rangle, |-1\rangle\}$, giving rise to [20]

$$\mathcal{H} = \sum_{m_S=1,0,-1} |m_S\rangle\langle m_S| \otimes \mathcal{H}_{m_S}, \quad (1.3.4)$$

where

$$\mathcal{H}_{m_S} = \omega_{m_S} + \mathcal{H}_{\mathrm{B}} + m_S \sum_{i=1}^{N} (A_i I_{iz} + B_i I_{ix}). \quad (1.3.5)$$

Furthermore, $\mathcal{H}_B = \sum_{i=1}^{N} \gamma_i B_z I_{iz} + \mathcal{H}_{n-n}$ is the bath Hamiltonian. Finally,

$$\omega_1 = D + \omega_e, \tag{1.3.6}$$

$$\omega_0 = 0, \tag{1.3.7}$$

$$\omega_{-1} = D - \omega_e, \tag{1.3.8}$$

where $\omega_e = \gamma_e B$ is the Larmor frequency of the electron spin, are the eigenvalues of the electron spin Hamiltonian $\mathcal{H}_e$ (first and second term of Eq. 1.3.3). A direct consequence of the form of Hamiltonian 1.3.4 is that, by opportunely initializing the electron spin (more on that in Chapter 3) and appropriately choosing the control pulses as having precisely the right frequency ω_1, the $|-1\rangle$ state can be frozen out of the dynamics since no transitions are allowed towards it. Therefore, the electron spin effectively behaves as a qubit [20], and we will call it qubit from this point forward.

In this context, *ab initio* methods are used to capture physical effects due to the 3D distribution of the spin density in the vicinity of the qubit, which mainly extends until the third neighbor shell in 3C-SiC crystal structure (see Fig. 1.4). These effects are not included in the semiclassical approximation, where the electron and nuclear spins are considered as classical magnetic point-dipoles interacting with each other [96]. In the semiclassical approximation, the hyperfine tensor can be written as

$$\boldsymbol{\mathcal{A}}_i = \frac{\mu_0 \gamma_i \gamma_e}{4\pi r_i^3} \left(1 - \frac{3\mathbf{r}_i \mathbf{r}_i}{r_i^2} \right), \tag{1.3.9}$$

where μ_0 is the vacuum magnetic permeability, γ_i and γ_e are the i-th nuclear spin and electron spin gyromagnetic ratios, respectively, whereas $\mathbf{r}_i$ is the position vector of the i-th nuclear spin with respect to the qubit, its modulus r_i being the distance between the two. Of course, as noticed, Eq. 1.3.9 is no longer applicable in the immediate vicinity of the qubit.

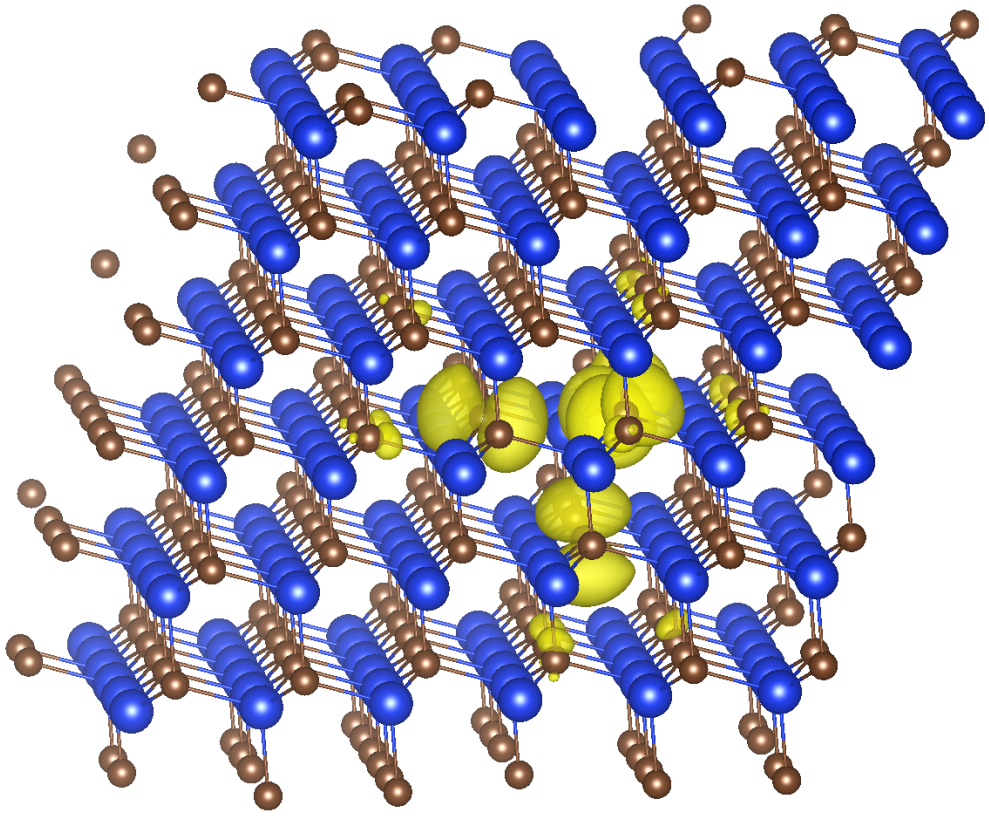

Figure 1.4: 3D spin density around a neutral V_{Si} in 3C-SiC. The spin density differences are mainly extended until the third neighbor shell. The wave functions are calculated for a $6 \times 6 \times 6$ 3C-SiC supercell.

1.3.2 Parameter Calibration

The introduction by Pickard and Mauri of the Gauge-Including Projector Augmented-Wave (GIPAW) method [23] made it possible to calculate all-electron NMR/EPR parameters in solids, i.e. accounting for periodic boundary conditions [97]. Since the GIPAW method roots itself in the plane wave pseudopotential formalism of the DFT, Ceresoli et al. [98, 99] wrote a QE module, known as QE-GIPAW, implementing it and working with the QE output wave functions. We have used QE-GIPAW to cal-

culate EPR-related parameters such as the hyperfine tensor components appearing in Eq. 1.3.3, thereby calibrating our Hamiltonian. Other parameters like the ZFS D and E components appearing in Eq. 1.3.2 are instead calculated by using the free and open-source PyZFS code from the Galli group [100].

The way in which QE-GIPAW goes beyond the semiclassical approximation of Eq. 1.3.9 is by modeling the non-zero spin density around the defect, which is shown in Fig. 1.4. This is immediately clear when analyzing the equations implemented in the code. First of all, the hyperfine tensor can be decomposed in an isotropic component, also known as Fermi contact term, and a traceless anisotropic component, also called dipolar term [101], i.e.

$$\boldsymbol{\mathcal{A}}_i = \mathcal{A}_i^{\text{iso}}\mathbf{1} + \boldsymbol{\mathcal{A}}_i^{\text{dip}}, \tag{1.3.10}$$

where $i = 1, \ldots, N$ again indicates the nuclear spin and $\mathbf{1}$ is the unit tensor. The Fermi contact term can be written as

$$\mathcal{A}_i^{\text{iso}} = \frac{8\pi}{3}\frac{\mu_0\gamma_i\gamma_e}{2S}\int \mathrm{d}\mathbf{r}\,\rho_s(\mathbf{r})\delta_T(\mathbf{r}), \tag{1.3.11}$$

where in our case $S = 1$ and $\delta_T(\mathbf{r})$ is the Thomas delta function (resulting from scalar relativistic corrections), which is equal to the Dirac delta in the non relativistic limit, and is defined as

$$\delta_T(r) = \frac{1}{4\pi r^3}\frac{2}{Z\alpha^2}\frac{1}{\left(1+\frac{2}{Z\alpha^2}\right)^2}. \tag{1.3.12}$$

In Eq. 1.3.12 Z is the atomic number and α is the fine structure constant. In general, QE-GIPAW computes the Fermi contact term both in the non-relativistic and relativistic limit, the latter being called ZORA (it stands for Zeroth-Order Regular Approximation). As for the dipolar term, we

have

$$\mathcal{A}^{\mathrm{dip}}_{i,\alpha\beta} = \frac{\mu_0 \gamma_i \gamma_e}{2S} \int \mathrm{d}\mathbf{r}\, \rho_s(\mathbf{r}) \frac{3 r_\alpha r_\beta - \delta_{\alpha\beta} r^2}{r^5}. \tag{1.3.13}$$

The difference between Eq. 1.3.9 and Eqs. 1.3.11 and 1.3.13 is precisely the spin density $\rho_s(\mathbf{r})$. Therefore, the hyperfine tensor components can be computed by a PAW-reconstruction of the ground state spin density $\rho_s(\mathbf{r})$. This, in turn, can be achieved by using the QE output wave functions, which are obtained through the DFT, a ground state theory in its original version [102]. In Section 1.3.6 our results on the hyperfine tensor components in Eq. 1.3.3 by using QE-GIPAW can be found.

1.3.3 Convergence of QE parameters

For our computational study we have used the density functional theory as implemented in the open-source QE code [22] for the calculation of the energetic and magnetic properties of the V_{Si} in 3C-SiC.

For what concerns the optimization of the supercell for our system, which is bulk cubic SiC or 3C-SiC, we started from the conventional unit fcc cell containing two atoms and made a 3x3x3 scaling until we have obtained a 53 atom supercell (considering the silicon vacancy). Then we performed a structural relaxation without the spin degree of freedom, the output of which we exploited to read the initial positions of a new calculation (of the same type), this time including the spin degree of freedom. We chose a broken symmetry starting point with an initial magnetization of 0.5 Bohr mag/cell for the four first-neighbor carbon atoms to the vacancy and 0 Bohr mag/cell otherwise (for a neutral vacancy). Then we repeated this protocol for an increasingly large supercell, obtained by changing the scaling factor. This optimization protocol produces a kind of decrease of the computational weight for the desired calculation.

The following four tables show the effect of the variation of a few important parameters and of the details of the pseudopotentials on the convergence of a single scf (self-consistent field) cycle of a 53 atom fcc

supercell	atoms	k points	Ener.(eV)	Mag.(Bohr mag/cell)
3x3x3 np	53	4 4 4	7.30	not defined
3x3x3 nc	53	4 4 4	7.30	(0.00 0.00 0.09)
3x3x3 soc	53	4 4 4	7.30	(0.00 0.00 0.09)
4x4x4 np	127	4 4 4	7.72	not defined
4x4x4 nc	127	4 4 4	7.61	(0.00 0.00 2.00)
4x4x4 soc	127	4 4 4	7.61	(0.00 0.00 2.00)
5x5x5 np	249	4 4 4	7.89	not defined
5x5x5 nc	249	4 4 4	7.65	(0.00 0.00 2.00)
5x5x5 soc	249	4 4 4	7.64	(0.00 0.00 2.00)
5x5x5 np	249	L	7.89	not defined
5x5x5 nc	249	L	7.65	(0.00 0.00 2.00)
5x5x5 soc	249	L	7.65	(0.00 0.00 2.00)
6x6x6 np	431	4 4 4	7.93	not defined
6x6x6 np	431	L	7.93	not defined
6x6x6 nc	431	L	7.66	(0.00 0.00 2.00)
6x6x6 soc	431	L	7.65	(0.00 0.00 2.00)
7x7x7 np	685	3 3 3	7.94	not defined
7x7x7 np	685	L	7.94	not defined
7x7x7 nc	685	L	7.66	(0.00 0.00 2.00)
7x7x7 soc	685	L	7.65	(0.00 0.00 2.00)

Table 1.1: Formation energies of a neutral silicon vacancy in 3C-SiC and total magnetization for different fcc supercells and k-point sets. Different calculation schemes for the defect's spin are examined, such as the non-polarized (np), non-collinear (nc) and spin-orbit coupling (soc) schemes.

(face-centered cubic) supercell. The standard values for each parameter are $\beta = 0.7$, degauss $= 0.01$ Ry, mixing mode "plain" (default value) and paw pseudopotentials. The variation of each parameter has been performed keeping the other ones fixed to their standard values.

In Table 1.1 we showed the formation energy of a neutral silicon vacancy and the total magnetization for various fcc supercells. These calculations are performed using informations obtained from structural optimization calculations on those supercells. As explained in the first paragraph, to alleviate the computational burden we've used the equilibrium positions of the non-polarized geometry to get the final positions of the non-collinear one, etc.

1.3.4 Methodology

We considered a $7 \times 7 \times 7$ 3C-SiC supercell starting from a primitive fcc unit cell, containing 686 atoms, for the calculation of the formation energy [103], whereas a $6 \times 6 \times 6$ supercell, containing 432 atoms, was employed for the evaluation of the EPR-related parameters like the hyperfine and ZFS tensor components. We used the Perdew-Burke-Ezernhof implementation [47] of the generalized gradient approximation for the description of the exchange-correlation functional. Ultrasoft pseudopotentials [76] were used for standard ground-state properties, whereas hyperfine interactions and ZFS tensors were computed with norm-conserving pseudopotentials [104], as the latter showed a better agreement with respective experimental results [25]. The formation energy was evaluated for the V_{Si} in various charged configurations considering a non-collinear scheme for the magnetization. EPR calculations were instead performed by using a collinear magnetization along the $[001]$ lattice direction, in order to better comply with usual experimental setups, where the external magnetic field is applied along the growth direction (which coincides with the $[001]$ crystal direction for most 3C-SiC growths [7]). Convergence was achieved with an asymmetric $3 \times 3 \times 3$ k-point grid [79] hav-

ing an offset with respect to the Γ point. Upon completion of the DFT calculations, the QE wave functions were used as an input in the QE Gauge-Including Projector Augmented-Wave (QE-GIPAW) code [23, 99], to calculate the hyperfine tensor components describing the V_{Si}-nuclear spins interaction. In addition, they were used to calculate the ZFS tensor components with the aid of the PyZFS code [100]. Finally, in order to better understand if the stacking sequence of the SiC polytype has important implications in the magnetic properties of the defect, hyperfine tensor calculations were also performed for a neutral V_{Si} in hexagonal 4H-SiC (for both k and h sites).

1.3.5 Formation Energy

An important issue for the determination of the stability of a particular defect under given thermodynamic conditions regards the energetic competition between its various charged states. Here we have calculated the formation energy of the neutral, and charged, V_{Si} within a 3C-SiC $7 \times 7 \times 7$ supercell, with a $3 \times 3 \times 3$ asymmetric k-point grid. The formation energy E_f of a defect X can be defined as the energy difference between the investigated defected system and the components in their reference states [105], i.e.

$$E_f\left[X^q\right] = E_{\text{tot}}\left[X^q\right] - E_{\text{tot}}\left[\text{bulk}\right] - \sum_i n_i\mu_i + \frac{q}{e}\left(E_{\text{VBM}} + \mu_e\right) + E_{\text{corr}}. \tag{1.3.14}$$

$E_{\text{tot}}\left[X^q\right]$ is the total energy of the host crystal with the defect with charge q, where $e > 0$ is the elementary charge of the electron, $E_{\text{tot}}\left[\text{bulk}\right]$ is the total energy of the same cell of crystal without the defect, and $n_i\mu_i$ is the reference energy of added (or subtracted with a change of sign) atoms of element i at chemical potential μ_i. The term in parenthesis accounts for the chemical potential of the electron(s) involved in charging the defect. E_{VBM} is the valence band maximum as given by the QE band structure

calculation for the bulk material, and μ_e is the electron chemical potential defined here with respect to the top of the corresponding valence band. The μ_e parameter can then be treated as a free parameter, allowing to account for a shift of the Fermi level, e.g., due to doping. Note that $\mu_e = E_{\text{gap}}/2$ corresponds to the undoped semiconductor case, where E_{gap} is the intrinsic semiconductor band gap. Finally, E_{corr} is a sum of relevant correction terms, the most important of which is the monopole correction term, taking into account the electrostatic interaction between the charged defect and its periodic replicas within the *ab initio* simulations. The monopole correction term can be written as [106]

$$E_{\text{corr}} = \frac{q^2 \alpha}{2\epsilon L}, \tag{1.3.15}$$

where q is the charge of the defect, α is the Madelung constant associated to our crystal structure, ϵ is the SiC experimental dielectric constant and L is the distance between the defect and its periodic replicas. For the neutral V_{Si} we have calculated $E_{\text{tot}}\left[V_{Si}^0\right] - E_{\text{tot}}\left[\text{bulk}\right]$ and μ_{Si} by using QE, whereas for the charged defects, for which q is different from zero, we have also calculated the valence band maximum (see Eq. 1.3.14). Upon structural relaxation inducing a local reconstruction around the defected site [107], the calculated magnetization for the V_{Si}^0, V_{Si}^{-1} and V_{Si}^{-2} defects was the one expected for a defect with electron spin-1, 3/2 and 1, respectively [108]. Fig. 1.4 shows the spin density around the central V_{Si}, which extends until the third neighbor shell. This nonzero spin density is modeled and implemented in the QE-GIPAW code and allows us to go beyond the semiclassical magnetic point-dipole approximation of Eq. 1.3.9 (see the next section).

As we can see in Fig. 1.5, in which the formation energy of a V_{Si} with different charge states is shown as a function of the Fermi level with respect to the valence band maximum (corrected with the monopole correction term given in Eq. 1.3.15), our *ab initio* results demonstrate the

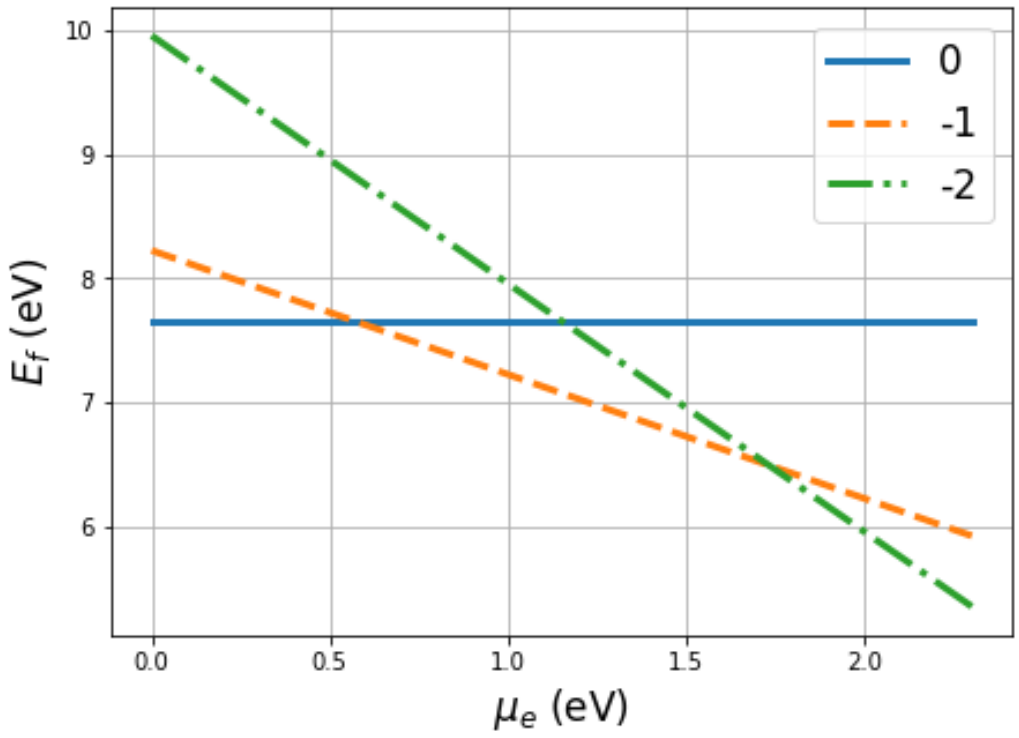

Figure 1.5: Formation energies of a neutral, -1 and -2 charged V_{Si} as a function of the electrochemical potential within the bandgap, for non-collinear calculations in a 686-atom 3C-SiC supercell.

atom	A_{xx}	A_{yy}	A_{zz}
C_1	26.2	26.2	84.5
C_2	27.4	27.4	85.6
C_3	28.8	28.8	87.1
C_4	27.5	27.5	85.7
$Si_1 - Si_{12}$	7.3	7.6	6.8

Table 1.2: *Ab-initio* calculated values (in MHz) for the hyperfine tensor components describing the interaction between a neutral V_{Si} in 3C-SiC and the nuclear spins in the first and second neighbor shells. The values are obtained by using the QE-GIPAW code [99].

stability of the neutral state for *p*-doped 3C-SiC samples. These results are in good agreement with previous studies [103, 107, 106] and along with the experimental verification of the defect in its neutral state [24] the theoretical study of its hyperfine interactions is motivated. Another motivation for studying defects that are stable in *p*-doped 3C-SiC samples is the great potential in applications of Al-doped 3C-SiC three gates devices in the MOSFET industry [109]. We note instead that focus has been mainly put to the V_{Si}^{-1} charged state in previous reports [25, 26, 110, 24], or to the neutral vacancy only for hexagonal SiC [111]. Within this context, in the next section the hyperfine interactions for a V_{Si}^{0} in 4H- and 3C-SiC are calculated by means of the DFT. Moreover, the ZFS tensor components of a V_{Si}^{0} in 3C-SiC are calculated as well.

1.3.6 Hyperfine interactions and Zero Field splitting

The results of our *ab initio* calculations can be used to define the hyperfine and ZFS tensors from first principles with the aid of the QE-GIPAW and PyZFS codes, respectively. Table 1.2 shows the hyperfine tensor components describing the interaction between a neutral V_{Si} in 3C-SiC and the nuclear spins in the first and second neighbor shells. In Tables 1.3 and 1.4, we show the same components for a neutral V_{Si} in 4H-SiC, lo-

cated in the two nonequivalent 4H sites (i.e., *k* and *h*), respectively. It is important to notice the different crystal structures (cubic and hexagonal) and basal plane orientations ([001] for 3C-SiC and [0001] for 4H-SiC) of the two SiC polytypes, which have an impact on the values obtained for the hyperfine interactions. For example, the 4H-SiC polytype shows hyperfine tensor components for one of the first neighbor ^{13}C nuclei (i.e., the one corresponding to the [0001]-axis of the hexagonal cell, or C_3 for the k site and C_2 for the h site) that have different values with respect to the other components. This is due to the parallel collinear magnetization along the [0001] direction imposed in the DFT calculations, along with the nonequivalent position of the vacancy sites in 4H-SiC. In 3C-SiC, the same behavior is not present due to the equivalent position (same distance from the defect) occupied by each ^{13}C nucleus in the first neighbor shell, forming a tetrahedron around the central V_{Si}. Moreover, the z-axis along which the external magnetic field is applied, coincides with the [001] direction, not with the [111] one (which is the equivalent of the [0001] direction in the cubic polytype). Instead, the surrounding of each ^{29}Si nucleus in the second neighbor shell is approximately invariant in the three cases, giving rise to similar hyperfine tensor components for the two crystal sites in 4H-SiC and for both polytypes. Note that our results in Tables 1.3 and 1.4 are in good agreement with the results of reference [25], whereas the calibration in Table 1.2 is missing in the literature.

Concerning the ZFS tensor components of the electron spin associated to a V_{Si} in 3C-SiC, the values obtained for the axial and transversal components are $D = 1.68\,\text{MHz}$ and $E = -0.41\,\text{MHz}$, respectively. In Appendix A we demonstrate that with our choice of parameters, the presence of both components (D and E) leads to similar results for the electron spin dynamics as when $E = 0$. Therefore, in the rest of the paper we will consider $E = 0$ for simplicity.

atom	A_{xx}	A_{yy}	A_{zz}
C_1	24.5	24.4	76.3
C_2	24.5	24.4	76.2
C_3	34.4	34.4	110.4
C_4	24.5	24.4	76.2
$Si_1 - Si_{12}$	7.5	7.8	6.9

Table 1.3: *Ab-initio* calculated values (in MHz) for the hyperfine tensor components describing the interaction between a neutral V_{Si} (k site) in 4H-SiC and the nuclear spins in the first and second neighbor shells. The values are obtained by using the QE-GIPAW code [99].

atom	A_{xx}	A_{yy}	A_{zz}
C_1	24.3	24.2	75.1
C_2	34.2	34.2	112.3
C_3	24.4	24.3	76.0
C_4	24.7	24.6	77.1
$Si_1 - Si_{12}$	7.5	7.8	6.9

Table 1.4: *Ab-initio* calculated values (in MHz) for the hyperfine tensor components describing the interaction between a neutral V_{Si} (h site) in 4H-SiC and the nuclear spins in the first and second neighbor shells. The values are obtained by using the QE-GIPAW code [99].

1.3.7 Control Techniques

Since the birth of Quantum Computing (QC) and the need to perform quantum information processing tasks, control techniques have been devised and developed to avoid unwanted errors in the procedure [112]. Among the different fields in the quantum landscape of research, NMR is the one that made the most significant progress in the application of control techniques [113]. As a matter of fact, control protocols have been borrowed from NMR and applied to multiple-qubit gates taken from various different pieces of hardware and arranged in different architectures [114], including ion traps [115], superconducting qubits [116, 28] and quantum dots [117].

In particular, NMR/EPR systems can be driven with microwave laser pulses that are highly transition-selective for coherent control purposes [4, 5]. The reason why in NMR these pulses are so effective in triggering transitions boils down to the single systems' property of having well-defined eigenfrequencies [118, 27], like one has in atomic physics. Consequently, that is also the reason why using transition-selective control pulses for other types of solid state qubits, like superconducting qubits, is more challenging. One has to devise a clever architecture to be able to increase the system's anharmonicity and single out two energy levels over the others [119]. Otherwise, multiple transitions are excited with a single pulse and the analysis becomes more complex.

However, the laser pulses are not the end of the story. They have to be cleverly put together in a quantum control protocol to shield the qubit from environmental noise [120, 121]. In NMR/EPR systems environmental noise takes the form of magnetic field noise that results from the effect of accumulating disturbances from each nuclear spin-generated magnetic field (such static magnetic field inhomogeneity causes inhomogeneous broadening of the spectral lines [28]). This strong sensitivity to magnetic field noise and temperature variations is also used as a tool for the emerging field of Quantum Sensing of magnetic field and tempera-

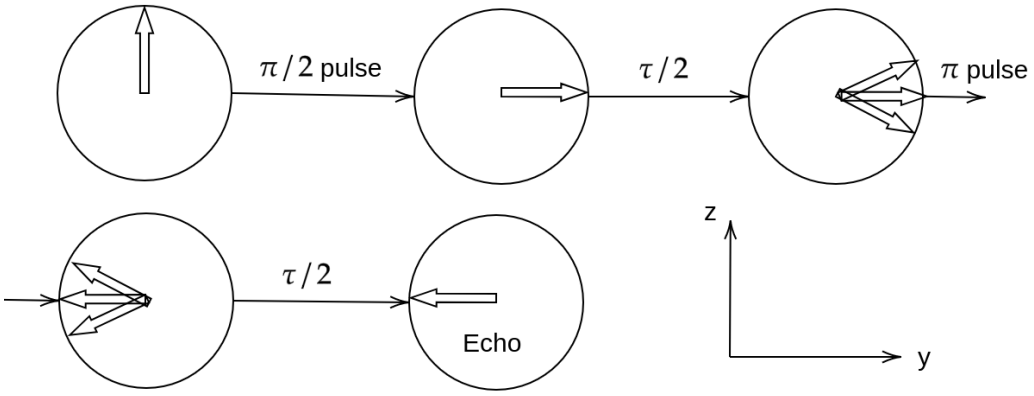

Figure 1.6: Graphical depiction of the Hahn-echo sequence in the representation of the Bloch sphere, with the two pulses achieving initialization and refocusing, respectively.

ture gradients [122, 123, 124, 125, 126]. To limit inhomogeneous broadening (FID), during my PhD we have studied the effect of the Hahn-echo sequence [127, 20, 128], an established control technique allowing to refocus the spin coherence, or the non-diagonal component of the qubit's density matrix, which is our objective.

An interesting case to study is the qubit's free evolution, known as FID [129]. In the literature experiments are described that elucidate the quantum mechanical origins of the FID signal and of spin noise [130]. FID has also been used as a means of controlling the phase and amplitude of extreme ultraviolet photons [131]. Here, after an initial $\pi/2$ pulse achieving initialization, the qubit's state keeps precessing on the equatorial plane of the Bloch sphere undergoing oscillations that are known in the literature as Rabi oscillations [132]. However, the presence of magnetic noise is manifest during free evolution, so that the introduction of noise-removing techniques like the Hahn-echo sequence is necessary (next paragraph). Our study of the FID signal of a neutral V_{Si} interacting with a bath of ^{29}Si and ^{13}C nuclear spins in 3C-SiC, as a function of free evolution time and in the frequency domain, can be found in Chapter 3.

Viewed in the Bloch sphere representation, the Hahn-echo sequence is easily pictured [27, 128] (Fig. 1.6). The qubit's density operator is initially represented by a vector pointing towards the north pole (the initial state is pure). Then a $\pi/2$ pulse brings the vector onto the equatorial plane, where it precess due to the external magnetic field. The precession proceeds for a finite waiting time known in the literature as free evolution time [20, 15], or τ. During this time one realizes that the vectors are more than one, each associated to a different component of the coherence, and the final vector is a mean of all the component vectors. Specifically, to various transitions that are sensitive to the magnetic field inhomogeneity in a different way [128]. Consequently, they acquire a non-zero phase with respect to one another. At this point, a π pulse is applied to invert the coherence y component, thus inverting also the phases of the precessing vectors. Finally the vectors return in phase along the $-y$ axis after a second free evolution time τ. Our application of the Hahn-echo sequence to a neutral V_{Si} interacting with a bath of ^{29}Si and ^{13}C nuclear spins in 3C-SiC can be found in Chapter 3. On the other hand, its application to a defected 3C-SiC nanoparticle for sensing applications is presented in Chapter 4.

Furthermore, when microwave pulses are applied to control the qubit, or the electron spin in this case, the nuclear spin bath surrounding it is consequently affected. A phenomenon known in the literature as Electron Spin-Echo Envelope Modulation (ESEEM), and dependent upon interactions between the electron spin and single nuclear spins, has been studied for a long time [133]. In particular, the mere reorientation of the electron spin moment by a microwave pulse causes non-adiabatic changes in the local dipolar field felt by the neighboring nuclear spins. Consequently, the modified nuclear spin precession creates in turn oscillations in the coherent, or quantum, nuclear dipolar field at the electron spin site that modulate the electron spin Larmor frequency [128, 133]. This results in fast oscillations of the signal in the time domain [15], either the abso-

lute value of the coherence or its imaginary part, which are modulated in a beating pattern and are clearly visible, as we will see. We study the ESEEM phenomenon as well in Chapter 3.

Chapter 2

Aluminum Frenkel defects as bistable traps in Al_2O_3/AlGaN junctions

2.1 Introduction

The classic sentiment towards defects in the literature has mainly been one of concern for performance. In the field of nanoelectronics, e.g., defects within Metal-Oxide-Semiconductor (MOS) devices are known to undermine their electrical properties [134]. In this chapter we take a traditional approach by proposing Frenkel defects in Al_2O_3 as a cause of hysteresis in MOS devices based on Al_2O_3/AlGaN junctions, and suggest their elimination for improving performance, before arguing in the next chapter, on the flip side, that defects can also be useful.

Frenkel defects can form in silicon carbide along with the other defects we have been analyzing up to this point [135, 136, 137]. For instance, in Snead et al. [138] Si- and C-Frenkel defects are utilized to store energy in SiC, $\sim$ 74% of storage being due to C-Frenkel defects and the rest being equally shared between the silicon ones and antisite defects, respectively.

Furthermore, Frenkel and antisite defects are at the basis of mechanical properties of amorphous SiC [139]. Frenkel defects also appear in MOS capacitors, specifically in the oxide layer (SiO_2 for SiC MOS devices), e.g. being used as hydrogen sensors in harsh environments [140]. Here, the need arises of materials whose electronic properties' thermal stability is excellent. These include silicon carbide, group-III nitrides like AlN, GaN and AlGaN, and diamond. Among them, Aluminum based MOS capacitors possess a longer history in the literature, and in particular the influence of defects in Al_2O_3 films on them [141]. However, to the best of our knowledge we are not aware of many works on Frenkel defects in the oxide layer of Al_2O_3/AlGaN junctions causing hysteretic behavior in the C-V characteristics of the corresponding MOS device. Consequently, we have been motivated in studying an Aluminum MOS capacitor in ref. [12], even though a work on SiC MOS capacitors constitutes a possible future project.

As noted in Chapter 1, Al_2O_3 is frequently utilized as dielectric in order to control microelectronic devices' electrostatics, and for its excellent mechanical and chemical properties [63]. In order to produce Al_2O_3 stoichiometric layers having high quality at the junction interface, Atomic Layer Deposition (ALD) at low temperatures may be used. They possess thicknesses ~ 10 nm and have structural properties typical of amorphous materials [142, 143]. We have also seen that Al_2O_3 in Al_2O_3/AlGaN junctions causes hysteretic behavior in MOS capacitors [64, 65, 66, 67, 68], which in turn hinders the device's electronic properties. This is due to Frenkel bistable defects effectively behaving as charge traps [65] in the oxide layer (localized at the interface between Al_2O_3 and AlGaN), whose state can be controlled by means of a gate voltage. An energy barrier separates the defect's stable state from a metastable one. Therefore, we have determined the electronic and structural properties of amorphous Al_2O_3 through *ab initio* methods (Section 1.2), which is important for understanding hysteresis in Al_2O_3/AlGaN capacitors.

We have performed a theoretical as well as a computational analysis to shed light on the structural and electronic characteristics of Al_2O_3, in order to single out the defect causing the peculiar charging effect in Al_2O_3/AlGaN junctions. In the literature DFT has been utilized to calculate formation energies and transition energies between different charge states for various defects in Al_2O_3 [144, 87, 88, 145]. On the other hand, molecular dynamics techniques are useful for analyzing the relaxation of atomic structures until an energy minimum is reached [145, 146, 147]. In a previous study neutral oxygen vacancies have been singled out as defects with bistable energy level configuration in α-Al_2O_3 [91]. As it turns out, however, an overwhelming concentration of this defect would result in a substoichiometric behavior in the oxide layer, whereas ALD-generated films mainly display stoichiometric behavior [148]. Thus, it is crucial to examine whether there exist additional oxide defects exhibiting bistable configuration behavior, which do not modify the balanced O/Al ratio of Al_2O_3. Therefore, in Chapter 1 we prepared an undefected α-Al_2O_3 supercell that underwent a high temperature annealing through Car-Parrinello [69] molecular dynamics to create structural defects. Moreover, the spectroscopic properties of core-level electrons in α-Al_2O_3 are similar to those of amorphous Al_2O_3 [64]. During the annealing procedure our stoichiometric Al_2O_3 supercell formed Al Frenkel defects ($V_{Al}Al_i$). Furthermore, a bistable energy level configuration under our chosen charging conditions was manifest. At this point, we introduce a model that features a distribution of individually interacting energy levels having an internal reconfiguration mode. Each energy level is in turn coupled to continuous bands of charge carriers in order to explain the hysteresis effect in Al_2O_3/AlGaN capacitors.

The chapter is organized as follows: in Section 2.2 we introduce the polaron theory that is then applied in Section 2.3 to model the interface trap states in the oxide layer of Al_2O_3/AlGaN junctions, explaining the hysteresis effect in the corresponding MOS devices. Finally, in Section 2.4

our conclusions are discussed.

2.2 Polaron theory

A polaron is a quasiparticle formed by the interaction between electrons and phonons. Indeed, whenever an electron moves in a dielectric crystal the atoms approach it (forming a phonon cloud) to effectively screen its charge, lower its mobility and increase its effective mass. In the literature, bistability has been attributed only to the effects of trap charging during C-V or I-V analyses. However, our study goes beyond by analyzing the role of atomic reconfiguration linked to charge states (polaronic effect). On a practical level, in the presence of a polaronic effect the system remains in one of the two trap states even after the voltage sweep. To the best of our knowledge, this aspect of our work is absent in the specialized literature.

As it turns out, polarons are central in the understanding of hysteresis in these systems. Thus, to probe the consequences of hysteretic behavior in the characteristics of an Al_2O_3/AlGaN MOS capacitor, we have utilized a simplified model whose calibrated parameters facilitate its representation of the fundamental interactions of the trap levels (in which polarons are formed). The model is composed by a distribution of singularly interacting levels having an internal reconfiguration mode coupled to continuous bands (baths) of carriers, which describe the semiconductor and metal regions of the junctions. The influence of bistable traps (see Fig. 1.2) in the C-V characteristics is thus modeled by calculating the modification of the corresponding energy level distribution due to the interaction with local phonon modes, which reflect the atomic reconfiguration in uncharged and charged states. The process can be formulated by the following Hamiltonian, which is a generalization of Anderson's Hamiltonian describing a single spinless electron level coupled to a single vibrational mode and to the leads [149] (here substituted by a set of

electron bands, or baths):

$$\begin{aligned}\mathcal{H} &= \sum_{n,\sigma} \epsilon_n c^\dagger_{n,\sigma} c_{n,\sigma} + \sum_n \hbar\omega_n a^\dagger_n a_n \\ &+ \sum_{n,\sigma} \chi_n (a^\dagger_n + a_n) c^\dagger_{n,\sigma} c_{n,\sigma} + \sum_{\mathbf{k},\sigma' \in \text{ baths}} \{E(\mathbf{k})\}\, c^\dagger_{\mathbf{k},\sigma} c_{\mathbf{k},\sigma} \\ &+ \sum_{\mathbf{k},\sigma' \in \text{ baths}} V^i(\mathbf{k}) c^\dagger_{\mathbf{k},\sigma} c_{i,\sigma} + \text{h.c.} \quad .\end{aligned} \tag{2.2.1}$$

In Eq. 2.2.1, $c^\dagger_{n,\sigma}(c_{n,\sigma})$ is the creation (annihilation) operator of an electron in the n^{th} energy level ϵ_n. On the other hand, $a^\dagger_n(a_n)$ is the creation (annihilation) operator of the energy reconfiguration mode $\hbar\omega_n$ (assuming a parabolic increase in energy with respect to the minimum of a generalized reconfiguration coordinate), whereas χ_n is the Holstein-type coupling constant between the mode and level n [150]. Finally, $\{E(\mathbf{k})\}$ is the dispersion relation of the carrier bands coupled to the levels, whereas $V^i(\mathbf{k})$ are the coupling constants between levels and bands related to hopping $(c^\dagger_{\mathbf{k},\sigma} c_{i,\sigma})$ from the level and the band and *vice versa* (h.c. being the hermitian conjugate).

As it turns out, only by reducing the number of bosonic modes within the reconfiguration one can obtain exact numerical solutions of Eq. 2.2.1 in systems having few levels. Alternatively, approximate solutions can be found by utilizing appropriately structured coherent states for the variables describing the reconfiguration process, in order to reach a good estimate of the solutions. Another useful approximation in this context is the adiabatic approximation (Born-Oppenheimer), which is applicable since the amplitude W of the electronic bands $E(\mathbf{k})$ is much greater than $\hbar\omega_n$. However, what differentiates this from the general case is the mandatory inclusion of the coupling constants $V^i(\mathbf{k})$ within electronic-type variables, which can correspond to energies $\sim \hbar\omega_n$ for carriers transiting from metal and semiconductor bands to the levels in the oxide. In the single level case, a thorough approach has been introduced in Ref. [150] for these conditions by introducing coherent states with three pa-

rameters rather than one, associated to the adiabatic case. In that work, an effective Hamiltonian was obtained by applying first a translation transformation accounting for static distortion,

$$U_1 = \exp\left[-\sqrt{\frac{\lambda}{\hbar\omega}}(a^\dagger - a)\tilde{x}_0\right], \tag{2.2.2}$$

where $\lambda = \chi^2/\hbar\omega$ and $\tilde{x}_0$ is the dimensionless distortion. Then, the dynamic distortion was dealt with by means of a Lang-Firsov transformation [151, 152],

$$U_2 = \exp\left[-\sqrt{\frac{\lambda}{\hbar\omega}}\theta(a^\dagger - a)(c_0^\dagger c_0 - \tilde{x}_0)\right], \tag{2.2.3}$$

where θ is a measure of the weight corresponding to the Small Polaron (SP) anti-adiabatic character of the solution. Finally, anomalous fluctuations averaging the transformed Hamiltonian were introduced by considering a squeezed phonon state,

$$|\Phi_{\text{ph}}\rangle = \exp\left[-\alpha(aa - a^\dagger a^\dagger)\right]|0_{\text{ph}}\rangle, \tag{2.2.4}$$

where α measures the phonon quantum state's displacement from the standard Gaussian fluctuations. This method can thus be generalized in order to obtain from Eq. 2.2.1 a purely electronic model Hamiltonian depending on parameters linked to the structural reconfiguration, which can in turn be optimized by using the variational principle. The effective model determined in this way is the following:

$$\begin{aligned}\mathcal{H}_{\text{eff}} = &\sum_{n,\sigma}\tilde{\varepsilon}_n c_{n,\sigma}^\dagger c_{n,\sigma} + \sum_{\mathbf{k},\sigma'\in\text{ baths}}\{E(\mathbf{k})\}\, c_{\mathbf{k},\sigma}^\dagger c_{\mathbf{k},\sigma} \\ &+ \sum_{\mathbf{k},\sigma'\in\text{ baths}}\widetilde{V}^i(\mathbf{k})c_{\mathbf{k},\sigma}^\dagger c_{i,\sigma} + \text{h.c.} \\ &+ \sum_n \lambda_n\chi_n^2(1-\theta_n)^2 + 0.25 + \hbar\omega_n(\tau_n^2 + \tau_n^{-2}),\end{aligned} \tag{2.2.5}$$

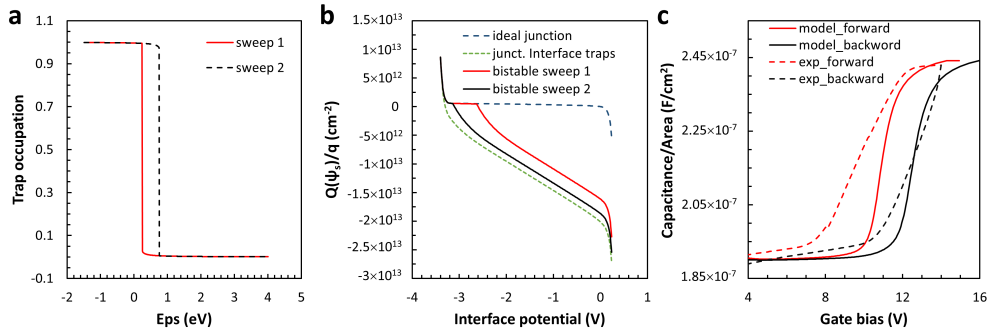

Figure 2.1: (a) Occupation state of the trap level $\rho^{1,2}$ as a function of the local electrochemical potential $(\tilde{\epsilon}_n - \mu)/\hbar\omega_n$ as solution for the parameters indicated in Table 2.1. (b) Charge $Q(\psi_s)$ at the oxide semiconductor interface as a function of the interface potential for various models of the MOS capacitor: ideal junction (blue), traditional interface traps (green), bistable states of the model formalized in this work (red and black). (c) Experimental C-V characteristics measured with forward and reverse sweeps of the gate potential in an Al_2O_3/AlGaN MOS structure compared to the predictions of the model with bistable states. The experimental curves are taken from an earlier work [64].

where $\lambda_n = \chi_n^2/\hbar\omega_n$ and $\tau_n = \exp(-2\alpha_n)$, while the functions that are modified during the variational procedure are

$$\tilde{\epsilon}_n = \epsilon_n - \lambda_n + \lambda_n(1-\theta_n)^2(1-2\chi_n), \tag{2.2.6}$$

$$\widetilde{V}^i(\mathbf{k}) = V^i(\mathbf{k})\exp[-(\lambda_n/2\hbar\omega_n)\theta_n^2\tau_n^2]. \tag{2.2.7}$$

By assigning appropriate values to the parameters entering these equations, various regimes may be reached that represent different physical situations.

2.3 Model of hysteresis in Al_2O_3/AlGaN capacitors

Now we are ready to apply the polaron theory from the previous section to shed light on the hysteresis mechanism in an Al_2O_3/AlGaN capacitor. We use the single-particle model of Eq. 2.2.5 in order to study the electrostatic and transport properties of MOS capacitors. In particular, the theoretical analysis is applied to the C-V characteristics of an Al_2O_3/AlGaN MOS capacitor. This section contains our approach at finding the solutions of the one-dimensional Poisson equation on the semiconductor side of the junction and along the z direction orthogonal to it,

$$\frac{\partial^2 \psi}{\partial z^2} = \frac{q}{\epsilon_s} \left(n(z) - p(z) + N_A(z) - N_D(z) \right). \tag{2.3.1}$$

In Eq. 2.3.1 N_A and N_D are the concentrations of ionized acceptors and donors, respectively, n and p are the electron and hole concentrations, ϵ_s is the dielectric constant of AlGaN, and q is the elementary charge. Within the model, we introduce a distribution of traps inside the insulating layer as a modification of the boundary solution of Eq. 2.3.1 at the semiconductor/oxide interface,

$$\epsilon_{ox} \frac{\psi_s - V_{gs}}{t_{ox}} - \epsilon_s \frac{\partial \psi}{\partial z}\Big|_{z=0} = \gamma Q_{trap}(\psi_s), \tag{2.3.2}$$

V_{gs} being the gate voltage, whereas t_{ox} and ϵ_{ox} are the thickness and dielectric constant of the oxide and ψ_s is the interface electrostatic potential at $z = 0$. On the other hand, Q_{trap} measures the density of charged traps and γ is a parameter depending on the spatial distribution of charges ($\gamma = 1$ whenever the charges are placed within the examined interface).

A direct relationship between the variational solutions of Eq. 2.2.5 and Eq. 2.3.2 may be established. Without loss of generality, three assumptions are in order: first we assume that the interaction parameters

Parameter	Description	Function	Value
$\hbar\omega_n$	Energy of the structural reconfiguration mode	-	25 meV
$\lambda_n/\hbar\omega_n$	Mode-level coupling constant	-	20
$W/\hbar\omega_n$	Bandwidth	-	200
$\Delta/\hbar\omega_n$	Band-level coupling constant	-	0.5
N_V	Density of states in the valence band of AlGaN	$2.3 \times 10^{14} \times T^{1.5}\text{cm}^{-3}$	-
N_C	Density of states in the conduction band of AlGaN	$4.4 \times 10^{14} \times T^{1.5}\text{cm}^{-3}$	-
$N_A - N_D$	Constant density of donors in the AlGaN layer ($N_D \equiv 0$)	-	10^{16} cm^{-3}
E_{Gap}	Band gap of AlGaN	-	3.4 eV
T	Temperature	-	300 K
ϵ_s	Relative dielectric constant for AlGaN	-	9.5
ϵ_{ox}	Relative dielectric constant for Al_2O_3	-	8.4
t_{ox}	Thickness of Al_2O_3	-	30 nm
A_{ox}	MOS junction area	-	0.41 cm^2
$D_{it}^{Simm}(\epsilon)$	Density of trap states	$0.9 \times 10^{13}\left[\left(\frac{\epsilon - E_{Gap}}{E_{Gap}}\right)^6 \times 0.45 + 0.55\right]$ cm^{-3}	-

Table 2.1: Parameters used in the polaron model of the Al_2O_3/AlGaN capacitor. The parameters are calibrated to reach a qualitative agreement between the C-V curves obtained from the model and the experimental ones.

are independent from the position of the level, second that the width of the W band is much greater than the other energies involved, and third that the double occupation of the level is negligible. In the electrostatic limit and by applying these assumptions the solution of the variational equations is given by [150]

$$x_n = \rho_n = 0.5 - \pi^{-1} \tan^{-1}\left[(\tilde{\epsilon}_n - \mu)/\widetilde{\Delta}\right], \tag{2.3.3}$$

$$\theta_n = \frac{\rho_n\,(1-\rho_n)}{\rho_n\,(1-\rho_n) - \tau_n^2 (S/2\hbar\omega_n)}, \tag{2.3.4}$$

$$\tau_n^2 = \sqrt{\left\{1 - \left[2\lambda S/(\hbar\omega_n)^2\right]\theta_n^2\right\}^{-1}}, \tag{2.3.5}$$

where the band parameter is constituted by

$$S = \frac{\widetilde{\Delta}}{2\pi} \log\left[\frac{(\tilde{\epsilon}_n - \mu)^2 + \widetilde{\Delta}^2}{(\tilde{\epsilon}_n - W)^2 + \widetilde{\Delta}^2}\right], \tag{2.3.6}$$

and the mean transfer constant is given by

$$\begin{aligned}\widetilde{\Delta} \cong \widetilde{\Delta}(E) = 2\pi \times \exp\left[-(\lambda_n/2\hbar\omega_n)\theta_n^2\tau_n^2\right] \times \\ \sum_{\mathbf{k}\in\text{baths}} |V(\mathbf{k})|^2 \delta_{\text{Dirac}}\left(E - E(\mathbf{k})\right),\end{aligned} \tag{2.3.7}$$

with the relative electrochemical potential of the level μ depending on the potential ψ_0. Noteworthy is the fact that the normalized generalized coordinate x_n is equal to the occupation function of the level ρ_n. In appropriate ranges of parameters, the variational Eqs. 2.3.3-2.3.5 can give rise to bistable solutions associated to local minima of the reconfiguration energy that are separated by an energy barrier. As a consequence of such bistable behavior, it is possible that the single trap level falls into one of the two solutions depending on the charging process, as opposed to the case without interactions being characterized by a given energy ϵ_n. Therefore, such level can show a different occupancy for the same

value of the electrochemical, or equivalently electrostatic, potential at the semiconductor/oxide interface. That is why we give in Fig. 2.1a an example of the dependence of the trap level occupation state provided by the model on the electrochemical potential, for a specific set of parameter values shown in Table 2.1.

In order to evaluate the effect of bistable occupation we have modified the expression utilized in conventional models for calculating the charge density due to the presence of traps within the interface,

$$Q_{trap}^{1,2}(\psi_s) = q\int_{E_v-q\psi_s}^{E_c-q\psi_s}[(1-f(\epsilon))\rho^{1,2}(\epsilon)D_{it}^{D}(\epsilon+q\psi_0) - f(\epsilon)\rho^{1,2}(\epsilon)D_{it}^{A}(\epsilon+q\psi_0)]\mathrm{d}\epsilon, \tag{2.3.8}$$

where E_v and E_c are the valence and conduction band energies, respectively, and $f(\epsilon) = 1/\left[1+\exp\left(\frac{\epsilon-\mu}{kT}\right)\right]$ is the Fermi-Dirac distribution as a function of energy. Finally, $D_{it}^{D}(\epsilon)$ and $D_{it}^{A}(\epsilon)$ are the densities of donor and acceptor states extracted from a single power expression symmetrized with respect to the center of the band $D_{it}^{Simm}(\epsilon)$ (shown in Table 2.1 for a particular set of values for the parameters), in which the contribution of donors has been neglected. An important thing to note is that there appear two different trapped charge functions depending on ψ_s and corresponding to the bistable solutions $\rho^{1,2}(\epsilon)$. Here, the continuum expressions utilized in Eq. 2.3.8 to estimate charging in the two cases could be the realistic counterpart of the discrete levels calculated by using the idealized *ab initio* machinery associated to two fixed charging conditions (see Fig. 1.2d), considering how relatively well-aligned are the Al_2O_3 and GaN bands [88]. Thus, in Fig. 2.1b we show the charge density $Q(\psi_s)$ at the semiconductor/oxide interface as a function of the potential at the interface and corresponding to various models of the MOS capacitor. The ideal junction case is shown as a dashed blue line, whereas the addition of traditional interface traps $\rho^{1,2}(\epsilon) \equiv 1$ is witnessed by the dashed green line. Finally, also the cases where the bistable states are obtained from

our model for a sweep of the potential from inversion to accumulation conditions (red line) and vice versa (black line) are shown. The parameters utilized to generate the lines in the graph are displayed in Table 2.1. The deviation of the charge density $Q(\psi_s)$ with respect to the ideal case is in turn an explicit demonstration for the deviation of the junction from its ideal behavior, which is caused by the contribution of the interface traps $Q_{trap}(\psi_s)$. Note also that the reconfiguration model we have introduced and formalized provides not only the appearance of bistability but also an energy shift (called polaronic ground state) with respect to the reference level. In Fig. 2.1c we compare the C-V characteristics calculated by means of our model with the experimental curves associated to an Al_2O_3/AlGaN MOS capacitor in the accumulation region. In such region, both display hysteretic behavior that could be justified by a bistability of the trap states. Due to its usefulness, the model can be further improved by means of a better calibration of the function $D_{it}^{Simm}(\epsilon)$ and by releasing the approximations introduced in the derivation of Eqs. 2.3.3-2.3.5 from Eq. 2.2.5, if it is supported by other independent evidence.

2.4 Discussion

In this chapter our work has been directed upon giving an atomistic interpretation of hysteresis in Al_2O_3/AlGaN MOS capacitors whenever a gate bias is applied. In particular, we have performed kinetic *ab initio* calculations showing that Aluminum atoms possess higher bonding capabilities with respect to the less mobile Oxygen atoms within the disordered Al_2O_3 corundum structure. This feature allows for the formation of complex defects depending on both the local environmental configuration and on the amount of charge present in the sample. In turn, such defects constitute the cause of the hysteresis behavior in Al_2O_3/AlGaN heterojunctions, as bistable configurations in Al Frenkel defects can generate deep trap levels within the band gap of AlGaN at given charging regimes, thus inducing

hysteresis in the corresponding MOS devices. However, our effort to single out a particular defect responsible for the hysteresis mechanism does not exclude the possibility of other bistable defects contributing to it in MOS capacitors. Instead, it highlights that even in the case of nominally stoichiometric Al_2O_3 thin films (for instance having an extremely low concentration of oxygen vacancies), the presence of Al complex defects can manifest itself in the appearance of hysteresis. Finally, it is important to note that similar defects may form in other oxide-semiconductor interfaces (e.g. SiO_2/SiC heterojunctions), whose study could lead to the limitation of hysteresis effects in the corresponding microelectronic devices.

In conclusion, our approach consisted in using Car-Parrinello molecular dynamics along with the nudged elastic band method in order to demonstrate that Al Frenkel defects can form bistable defects acting as charge traps in disordered and stoichiometric α-Al_2O_3. Furthermore, by means of a polaron model consisting of a distribution of individually interacting energy levels with an internal reconfiguration mode that are coupled to continuous bands of carriers, we have shown that such trap states can explain the hysteresis mechanism in the capacitance vs voltage measurements of Al_2O_3/AlGaN capacitors. Note that the probable emergence of similar bistable hysteretic behavior in different types of oxide defects is to be expected. Moreover, the experimental and theoretical study of such defects could enhance the understanding of MOS devices based on the Al_2O_3 gate dielectric.

Chapter 3

Cluster Correlation Expansion Theory

3.1 Introduction

We have seen in Chapter 2 a semiconductor material host of defects whose presence in the crystal structure causes misbehavior in the nanoelectronics field. In this chapter we change perspective by examining a different and rapidly emerging field where the coherent dynamics of point-defects is an opportunity for encoding, processing and read quantum information, i.e. the field of quantum technologies. In particular, we propose and focus on a defect whose experimental identification is missing in the literature, which is the neutral silicon vacancy in 3C-SiC (also indicated as V_{Si}^{0}).

Silicon Carbide (SiC) is a technological material that is widely studied in the literature [153]. Beyond its known application in the power electronics industry [154], in recent years it is gaining attention in the quantum technologies community [4] as a host of qubits [20] or a source of single photons [155]. SiC is found in a variety of polytypes differing by their stacking sequences, and although the most studied are the hexago-

nal ones [156, 157] due to growth issues, the cubic 3C-SiC polytype has the advantage to be heteroepitaxially grown on silicon substrates, along with a series of physical characteristics which are appealing for electronic devices (lower band gap, absence of deep level stacking-fault defect states, higher electron and hole mobilities, etc.) [6, 7]. In particular, point defects in 3C-SiC like silicon vacancies are promising candidates for qubits due to their decoherence times in the milliseconds range [15]. Furthermore, a recent study shows that out of the possible V_{Si} charge states the neutral one is energetically favored in a given electrochemical potential range [15]. The strong sensitivity of such defects to properties of the bath has been used in the literature for quantum sensing applications [4, 158].

In this chapter we focus on a neutral silicon vacancy magnetically interacting with the SiC nuclear spin bath, constituted by naturally occurring ^{29}Si and ^{13}C paramagnetic nuclei. The V_{Si}^{0} center can be modeled as a spin-1 defect, or electron spin, that evolves in the magnetic environment constituted by the spin-1/2 nuclear spin bath around it. Highly transition-selective microwave control pulses [5] are used to reduce the three electron spin's eigenstates to two in the resulting dynamics, so that it effectively behaves as a qubit. Such pulses are integrated in control procedures aimed at shielding the qubit against the magnetic noise coming from the environment. Inhomogeneity in the magnetic field felt by the qubit is one of the factors causing its loss of *coherence* [28]. To limit this phenomenon the Hahn-echo sequence has been introduced in the literature [127], an established control technique allowing to refocus the spin coherence.

However, in 3C-SiC samples there are thousands of paramagnetic nuclear spins, each of which exerts an influence on our qubit. In order to deal with nuclear spins in large baths, various theories have been introduced in the literature. Among them, CCE theory is particularly useful to calculate the qubit's coherence, which is our objective. CCE theory has been developed in reference [32] and is perfectly suited for qubits experi-

encing random interactions within a bath of finite size. As a matter of fact, whenever there are few nuclear spins in the bath, the qubit may not end its decoherence process within the nuclear spin flip-flop time and higher-order cluster correlations (cfr. Fig. 3.1) could be necessary to model the dynamics. In this case, among the various theories developed such as the density matrix Cluster Expansion (CE) [159], the pair-correlation approximation [160] and the Linked-Cluster Expansion (LCE) [161], only the CCE converges to the exact coherent dynamics of clusters containing multiple spins. In particular, a cluster in this context is defined as a group of fully interacting nuclear spins. CCE theory owes its high convergence property to the fact that it is a bridge between the LCE and CE approaches. One is not required to evaluate Feynman diagrams and is simultaneously free from the large-bath requirement of the CE. However, typically CCE theory does not converge whenever its N-th truncation, or CCEN (see below), is not sufficient to model the dynamics. In this case a term in the recursive expansion in the denominator of Eq. 3.2.5 below may become arbitrarily small, thus causing an overshoot of the final result, which lies outside of the expected range for coherence. The coherent dynamics of finite clusters of nuclear spins in the bath is relevant in systems with random couplings between the qubit and bath. Interesting examples are nitrogen-vacancy (NV) centers in diamond and V_{Si} in SiC, which are magnetically coupled to a bath containing randomly located nuclear spins [32]. For such systems, the analysis in reference [160] taking into account only pair-correlations is not sufficient, e.g., to describe free evolution (FID), which is governed by single interactions between the qubit and each nuclear spin in the bath. CCE theory has the advantage of being in principle exact (see below), while simultaneously being of great practical utility as an approximation scheme whenever many-body correlations within the bath are not relevant *and* being more flexible than pair-correlation approaches when higher-order correlations are needed.

The remaining part of this chapter is organized as follows: in Section

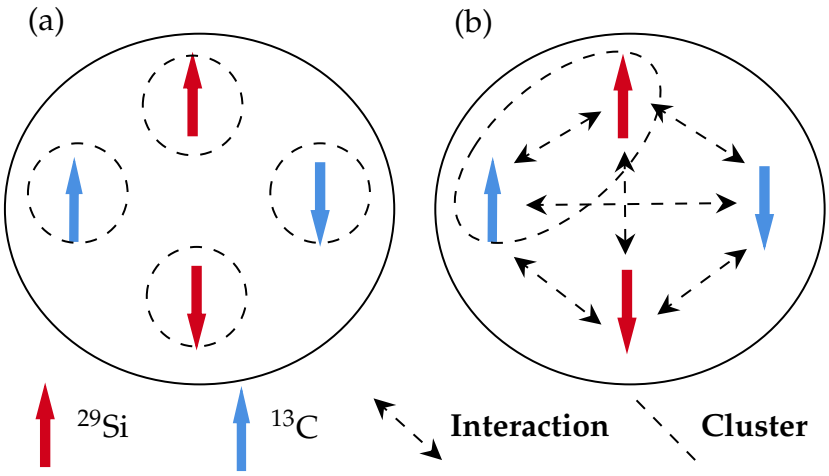

Figure 3.1: Functioning scheme of the CCE theory, for a generic bath in 3C-SiC containing two ^{29}Si nuclear spins (in red) and two ^{13}C nuclear spins (in blue). The spins are in general all interacting with each other via the last term of Eq. 1.3.1 and are represented in the up or down states with respect to the magnetic field axis. (a): CCE1 approximation in which clusters contain a single nuclear spin. (b): CCE2 approximation containing also two-dimensional clusters (for simplicity only one is shown).

3.2 CCE theory is introduced in detail, whereas in Subsections 3.2.1 and 3.2.2 such theory is applied to model the dynamics of the defect interacting with the entire nuclear spin bath surrounding it after a FID and Hahn-echo processes are implemented, respectively. In these subsections the results of our simulations on such control sequences are presented and our conclusions drawn.

3.2 CCE Theory

In general, the qubit coherence is defined as the off-diagonal component of the density matrix, or [20]

$$\mathcal{L}(t) \equiv \frac{\mathrm{tr}\left\{\rho_{\mathrm{tot}}(t) S_{+}\right\}}{\mathrm{tr}\left\{\rho_{\mathrm{tot}}(0) S_{+}\right\}}, \tag{3.2.1}$$

where $\rho_{\mathrm{tot}}(t)$ is the total qubit plus bath density operator at time t, $S_{+} = S_x + iS_y$ is the qubit raising operator and $\rho_{\mathrm{tot}}(0) = \rho_{\mathrm{S}}(0) \otimes \rho_{\mathrm{B}}(0)$ is the initial state of the overall system. In the dipolar approximation of Eq. 1.3.3 the qubit eigenbasis coincides with a subset of the S_z spin operator eigenbasis, i.e. $\{|1\rangle, |0\rangle\}$. The qubit is prepared in the pure state $\rho_{\mathrm{S}}(0) = |\Psi\rangle\langle\Psi|$, where

$$|\Psi\rangle = \frac{1}{\sqrt{2}}\big(|1\rangle + i|0\rangle\big), \tag{3.2.2}$$

so that $\langle S_y\rangle(0) = 1$ and $\langle S_x\rangle(0) = 0$. The preparation in state 3.2.2, together with the chosen form for the control pulses (see below) and the pure-dephasing approximation in Hamiltonian 1.3.3, ensures that the $|-1\rangle$ state stays out of the dynamics. The coherence $\mathcal{L}(t)$ is a complex function having the expectation values of the qubit S_x and S_y operators as real and imaginary parts, respectively. Furthermore, Eq. 3.2.1 becomes intractable rather quickly as the number of nuclear spins in the bath increases. The objective of CCE theory is then to provide a reasonable and computationally achievable approximated version of the whole coherence given in Eq. 3.2.1. In order to do so, the first step is the implementation of a numerical procedure generating a random bath of nuclear spins. The ^{29}Si and ^{13}C nuclear spins are thereby randomly put in our simulated 3C-SiC lattice, by using a random number generator, according to their natural abundance of 4.7 and 1.1%, respectively. In typical EPR experiments the temperature of the examined sample is $\sim 10\,\mathrm{K}$ [20, 128], allowing us to consider completely randomized baths in our CCE code,

whose collective state at $t = 0$ can be written as the mixed state

$$\rho_{\mathrm{B}}(0) = \bigotimes_{i=1}^{N} \frac{I_i}{2}, \tag{3.2.3}$$

where I_i is the i-th nuclear spin identity operator. Furthermore, in order to obtain a correct statistical sampling of the random bath-generating procedure, we calculate the qubit coherence as an average of the coherences associated to $\mathcal{N}$ different random baths, or $\mathcal{N}$ different realizations of the numerical procedure. Hence, in calculating the qubit coherence we confirmed that the converged value [20] for $\mathcal{N}$ in our simulations is $\mathcal{N} = 50$ (see Appendix A). In the generation of the random baths, other numerical parameters whose convergence is necessary are the radius of the spherical bath, R_{bath}, and the distance between nuclear spins beyond which they are no longer interacting, or nuclear spin connectivity, r_{dipole}. The converged values for these parameters (see Appendix A) are found to be $R_{\mathrm{bath}} = 5$ nm and $r_{\mathrm{dipole}} = 0.8$ nm, as in reference [20].

Once all of this is taken care of, we have implemented CCE theory through the equations [162]

$$\rho_C(t) = U_C \rho_C(0) U_C^{\dagger}, \tag{3.2.4}$$

$$\tilde{\mathcal{L}}_{\{C\}} = \frac{\mathcal{L}_{\{C\}}(t)}{\prod_{C'} \tilde{\mathcal{L}}_{\{C' \subset C\}}}, \tag{3.2.5}$$

$$\mathcal{L}(t) = \tilde{\mathcal{L}}_{\{0\}} \prod_i \tilde{\mathcal{L}}_{\{i\}} \prod_{i,j} \tilde{\mathcal{L}}_{\{ij\}} \cdots . \tag{3.2.6}$$

Eq. 3.2.4 describes the dynamics of the density matrix of the qubit interacting with a given cluster of nuclear spins C, the Hamiltonian in the time evolution operator U_C being given by Eq. 1.3.3 restricted to the sole presence of the nuclear spins within cluster C. Eq. 3.2.4 enters in Eq. 3.2.5

through $\mathcal{L}_{\{C\}}(t)$, which can be written as

$$\mathcal{L}_{\{C\}}(t) = \frac{\mathrm{tr}\left\{\rho_C(t)S_+\right\}}{\mathrm{tr}\left\{\rho_C(0)S_+\right\}}. \tag{3.2.7}$$

Eq. 3.2.5 describes the contribution of cluster C to the coherence. Since the clusters are uncorrelated, the coherence in Eq. 3.2.6 is defined as the product of each cluster's contribution. As a consequence, we can stop the expansion in Eq. 3.2.6 at a given order of approximation of the theory, which is represented by the number of nuclear spins within the largest clusters we choose to divide the bath in. Therefore, CCEN is the implementation of CCE theory where the biggest clusters we consider contain N different nuclear spins. In the remainder of the paper we focus exclusively on the CCE1 and CCE2 approaches, with clusters containing single and interacting pairs of nuclear spins, respectively (see Fig. 3.1 for the functioning scheme of the CCE1 and CCE2 approaches).

3.2.1 Free Induction Decay

In this subsection we focus on the FID process [128], i.e. we let the system freely evolve after the preparation of the qubit. The preparation is obtained via the application of a $\pi/2$ pulse to the qubit in the $|0\rangle$ state, so that the initial state is the one given in Eq. 3.2.2, and the entire FID process can be described as

$$\rho_{\mathrm{FID}}(\tau) = U_{\mathrm{FID}}(\tau)\rho_{\mathrm{S}}(0)U^{\dagger}_{\mathrm{FID}}(\tau), \tag{3.2.8}$$

where $U_{\mathrm{FID}} = e^{-i\mathcal{H}\tau}e^{-i\pi/2S_x}$ is the FID propagator, $\rho_{\mathrm{S}}(0) = |0\rangle\langle 0|$ and the system's Hamiltonian is given by Eq. 1.3.3. The real and imaginary parts of the coherence can be analytically calculated in the pure-dephasing approximation and CCE1 case, i.e. whenever we can write the Hamiltonian in the form of Eq. 1.3.4 and safely neglect the $\mathcal{H}_{n-n}$ interaction between nuclear spins inside the bath Hamiltonian in 1.3.5. Then we substitute

Eq. 1.3.4 in Eq. 3.2.1 through $\rho_{\text{tot}}(t)$, and the analytical expressions we obtain are the following,

$$\langle S_x \rangle_{\text{FID}}(\tau) = -\sin\left[(\omega_1 - \omega_0)\,\tau\right] \text{f}_\text{B}(\tau), \tag{3.2.9}$$

$$\langle S_y \rangle_{\text{FID}}(\tau) = \cos\left[(\omega_1 - \omega_0)\,\tau\right] \text{f}_\text{B}(\tau), \tag{3.2.10}$$

where

$$\text{f}_\text{B}(\tau) = \prod_{i=1}^{N} \left[\cos\left(\frac{\omega_{I_i}\tau}{2}\right)\cos\left(\frac{\Omega_{I_i}\tau}{2}\right) + \sin\left(\frac{\omega_{I_i}\tau}{2}\right)\sin\left(\frac{\Omega_{I_i}\tau}{2}\right)\frac{\omega_{I_i} + A_i}{\Omega_{I_i}}\right] \tag{3.2.11}$$

is a factor depending on the nuclear spins, and

$$\Omega_{I_i} = \sqrt{\left(\omega_{I_i} + A_i\right)^2 + B_i^2}. \tag{3.2.12}$$

In Eq. 3.2.11,

$$\omega_{I_i} = \gamma_i B \tag{3.2.13}$$

is the Larmor frequency of the i-th nuclear spin, where B is the external magnetic field.

Our results on FID, obtained with our customized code, are displayed in Figs. 3.2 and 3.3. In Fig. 3.2 we show a comparison between the coherence modulus of the qubit at the CCE1 and CCE2 levels of the theory, for two different external magnetic fields. The CCE1 curves exactly coincide with the analytical ones obtained as a graph of Eqs. 3.2.9 and 3.2.10. Note that there is no interesting effect that is modeled in the passage from CCE1 to CCE2, and the two versions give pretty close results. In Fig. 3.3 we present the same curves at the CCE2 level, both with semi-classical and *ab initio* hyperfine tensor components, for different external magnetic fields. As can be seen, the presence of even one single nuclear spin in the first shells of next-neighbors causes an appreciable change in the coherence, due to the difference in the hyperfine tensor components and therefore in Ω_{I_i} (remember that FID can be well-modeled already at

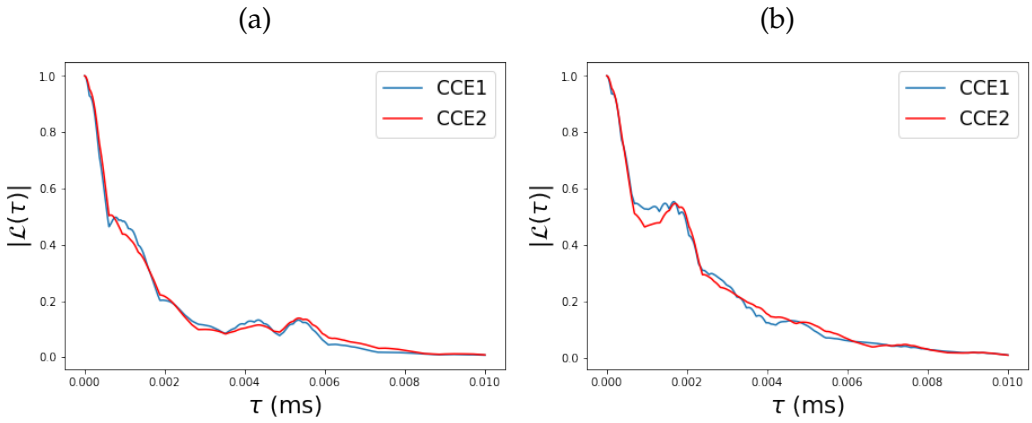

Figure 3.2: Absolute value of the coherence of a neutral V_{Si} in 3C-SiC as a function of free evolution time, both at the CCE1 and CCE2 levels, for an external magnetic field of 200 G (a) and 500 G (b). The dynamics implemented is a free evolution, or FID process, and the curves are averaged over 50 different baths.

CCE1).

In order to better understand our FID results and directly correlate differences in the position of the nuclear spins to the modification of the coherence modulation frequencies, we propose a manipulation of Eqs. 3.2.9 and 3.2.10. In particular, by opportunely rewriting those equations we are able to explicitly obtain the coherence modulation frequencies. To do that we have to express the product of N terms in Eq. 3.2.11 as a sum of sinusoidal functions, by repeatedly applying the appropriate trigonometric formulas, so that the modulation frequencies are easily calculated via a Fourier transform. The new expressions can be obtained by exploiting induction considerations (see Appendix B) and the imaginary part of the coherence, e.g., is given by

$$\langle S_y \rangle = \cos(\omega_1 \tau) \Sigma_N(\tau), \tag{3.2.14}$$

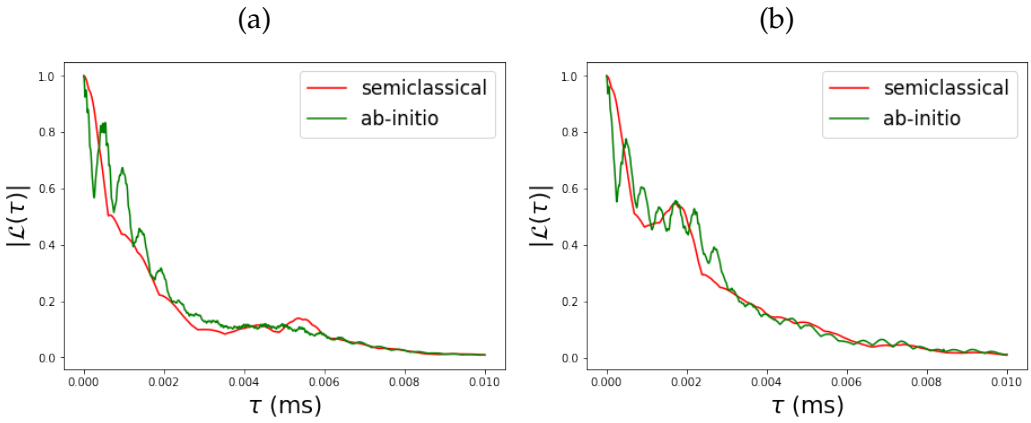

Figure 3.3: Absolute value of the coherence of a neutral V_{Si} in 3C-SiC as a function of free evolution time at the CCE2 level, both with semiclassical and *ab initio* hyperfine tensor components, for an external magnetic field of 200 G (a) and 500 G (b). The dynamics implemented is a free evolution, or FID process, and the curves are averaged over 50 different baths.

where

$$\begin{aligned}\Sigma_N(\tau) = \frac{1}{2^{2N-1}}\Big\{ & S_{I_1}\cdots S_{I_N}\Big[(+-+-\ldots+-)+\ldots+(+--+\ldots-+)\Big] \\ & + S_{I_1}\cdots D_{I_N}\Big[(+-+-\ldots++)+\ldots+(+--+\ldots--)\Big]+\ldots \\ & + S_{I_1}\cdots D_{I_i}\cdots D_{I_N}\Big[(+-\ldots++\ldots++)+\ldots+(+-\ldots--\ldots--)\Big] \\ & +\ldots+D_{I_1}\cdots D_{I_N}\Big[(++++\ldots++)+\ldots+(++--\ldots--)\Big]\Big\}.\end{aligned} \tag{3.2.15}$$

In Eq. 3.2.15 we have used the shorthand notation

$$(+-\ldots+-) \equiv \cos\left[(\omega_{I_1}/2-\Omega_{I_1}/2+\ldots+\omega_{I_N}/2-\Omega_{I_N}/2)\,\tau\right], \tag{3.2.16}$$

whereas

$$S_{I_i} \equiv 1 + \frac{\omega_{I_i} + A_i}{\Omega_{I_i}}, \tag{3.2.17}$$

$$D_{I_i} \equiv 1 - \frac{\omega_{I_i} + A_i}{\Omega_{I_i}}. \tag{3.2.18}$$

Inside the curly brackets there are 2^N terms, each of which is multiplied by a sum of 2^{N-1} cosines inside the square brackets. Therefore, without counting the qubit through its level splitting ω_1 (in which case the modulation frequencies would be doubled, see Appendix B), the modulation frequencies are $2^N \times 2^{N-1} = 2^{2N-1}$. Two immediate tests to demonstrate the correctness of Eq. 3.2.15 are its evaluation in trivial conditions for which we expect a specific behavior, i.e.

$$\Sigma_N \left(A = 0, B = 0\right) = 1, \tag{3.2.19}$$

$$\Sigma_N \left(\tau = 0\right) = 1. \tag{3.2.20}$$

Eqs. 3.2.19 and 3.2.20, coupled with Eq. 3.2.14, give us the expected behavior of the coherence imaginary part when the qubit is isolated from the environment and at the beginning of the dynamics, respectively. Additional considerations regarding Eq. 3.2.15 are reported in Appendix B.

The Fourier transform of the signal in time, given in Eq. 3.2.15, is

easily obtained and can be written as

$$\begin{aligned}\tilde{\Sigma}_N(\omega) = \frac{\pi}{2^{2N-1}}\Big\{ & S_{I_1}\cdots S_{I_N}\Big[[+-+-\ldots+-]+[-+-+\ldots-+]+\ldots \\ & +[+--+\ldots-+]+[-++-\ldots+-]\Big] \\ & +S_{I_1}\cdots D_{I_N}\Big[[+-+-\ldots++]+[-+-+\ldots--]+\ldots \\ & +[+--+\ldots--]+[-++-\ldots++]\Big]+\ldots \\ & +S_{I_1}\cdots D_{I_i}\cdots D_{I_N}\Big[[+-\ldots++\ldots++]+[-+\ldots--\ldots--]+\ldots \\ & +[+-\ldots--\ldots--]+[-+\ldots++\ldots++]\Big] \\ & +\ldots+D_{I_1}\cdots D_{I_N}\Big[[++++\ldots++]+[----\ldots--]+\ldots \\ & +[++--\ldots--]+[--++\ldots++]\Big]\Big\},\end{aligned} \tag{3.2.21}$$

where now each term inside the curly brackets is multiplied by a sum of Dirac delta functions, and we have introduced the notation

$$[+-\ldots+-] \equiv \delta\left[\omega+\omega_{I_1}/2-\Omega_{I_1}/2+\ldots+\omega_{I_N}/2-\Omega_{I_N}/2\right]. \tag{3.2.22}$$

In passing from Eq. 3.2.15 to Eq. 3.2.21, we have used the known result

$$\mathcal{F}\left[\cos(\omega_0 t)\right] = \pi(\delta[\omega+\omega_0]+\delta[\omega-\omega_0]). \tag{3.2.23}$$

By examining the signal in frequency, given in Eq. 3.2.21, we see that the Fourier transform will display delta-like peaks in correspondence to each modulation frequency inside the arguments of the delta functions. To exemplify this by means of an example, we report in Fig. 3.4 the imaginary part of the FID time signal of a V_{Si}^0 interacting with a single ^{29}Si nucleus in the second-neighbor shell, for simplicity, and its normalized Fourier transform obtained via a numerical Fast Fourier Transform (FFT) algorithm. Since in this case $N = 1$, the modulation frequencies are 4

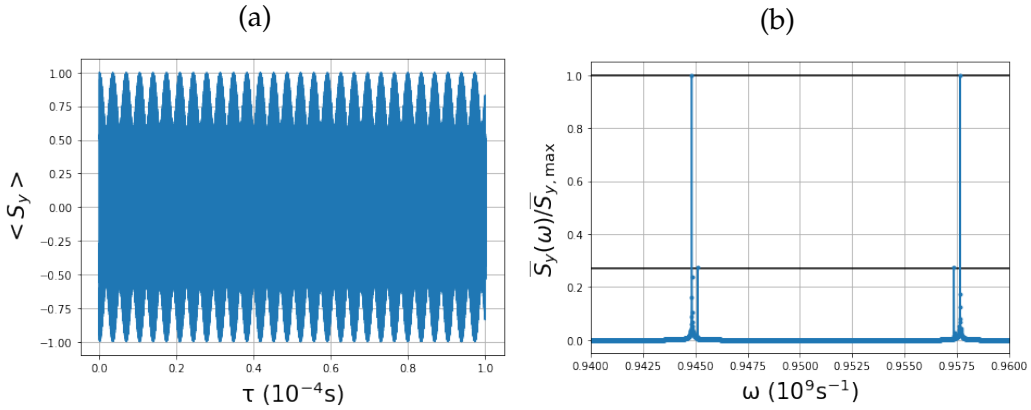

Figure 3.4: (a) Imaginary part of the coherence of a neutral V_{Si} in 3C-SiC as a function of free evolution time at the CCE1 level with *ab initio* hyperfine tensor components, for an external magnetic field of 340 G. The bath contains a single ^{29}Si nucleus in the second-neighbor shell. (b) Normalized Fourier transform of the signal in the time domain obtained via a numerical FFT algorithm.

(see Appendix B) and are quantitatively predicted by Eq. B.0.3 to be 0.9448 GHz, 0.9576 GHz, 0.9574 GHz and 0.9451 GHz, respectively, at the relative amplitude of $(1-\frac{\omega_I+A}{\Omega_I})/(1+\frac{\omega_I+A}{\Omega_I}) = 0.27$ for the central ones (see Fig. 3.4b). The modulation frequencies, containing information on how each nuclear spin in the bath affects the qubit during the dynamics, can be derived directly from the pure-dephasing Hamiltonian 1.3.3, in the CCE1 case or whenever $\mathcal{H}_{n-n} = 0$. In particular, they are obtained as linear combinations of our system's eigenenergies, as we demonstrate in Appendix C.

At this point, the difference in the modulation frequencies in going from the semiclassical to the *ab initio* curve in Fig. 3.3 is explained by considering the dependency of those frequencies, given in Eq. 3.2.15, on the hyperfine tensor components through Ω_{I_i}. In particular, in the case where the bath is composed by a single ^{13}C nucleus in the first neighbor shell, there are only two frequencies in the terms $(+-)$ and $(++)$. The first frequency doubles its value, from 13.1 MHz to 29.4 MHz, by using

the *ab initio* calibration.

3.2.2 Hahn-Echo

In NMR/EPR systems environmental noise takes the form of magnetic field noise that results from the effect of accumulating disturbances from each nuclear spin-generated magnetic field (such static magnetic field inhomogeneity causes inhomogeneous broadening of the spectral lines [28]). To limit inhomogeneous broadening, we have applied the Hahn-echo sequence [127], an established control technique [128, 20] allowing to refocus the spin coherence and thus enlarge its decoherence time [163, 20], which is the main goal of this subsection.

In this regard, the most important part of the spin-echo sequence is an intermediate π pulse applied to the qubit which allows to refocus the spin coherence resulting from the effect of static magnetic field inhomogeneities [27]. Consequently, the dynamics can be described in the following way:

$$\rho_{\mathrm{HE}}(\tau) = U_{\mathrm{HE}}(\tau)\rho_{\mathrm{S}}(0)U_{\mathrm{HE}}^{\dagger}(\tau), \tag{3.2.24}$$

where $U_{\mathrm{HE}}(\tau) = e^{-i\mathcal{H}\tau/2}e^{-i\pi S_x}e^{-i\mathcal{H}\tau/2}e^{-i\pi/2S_x}$ is the Hahn-echo propagator and $\rho_{\mathrm{S}}(0)$ is the same as for the FID case. Now, as a first order approximation, at the CCE1 level we can obtain analytical expressions for the coherence real and imaginary parts in the pure-dephasing approximation [20], as in the FID case. Therefore, the qubit coherence components in 3.2.1, after the Hahn-echo sequence, can be written as [128]

$$\langle S_x\rangle_{\mathrm{HE}}(\tau) = 0, \tag{3.2.25}$$

$$\langle S_y\rangle_{\mathrm{HE}}(\tau) = \prod_{i=1}^{N}\left[1 - 2k_{+1,0}^{i}\sin^2\left(\Omega_{I_i}\frac{\tau}{4}\right)\sin^2\left(\omega_{I_i}\frac{\tau}{4}\right)\right], \tag{3.2.26}$$

where

$$k_{+1,0}^{i} = \frac{B_i^2}{\Omega_{I_i}^2} \tag{3.2.27}$$

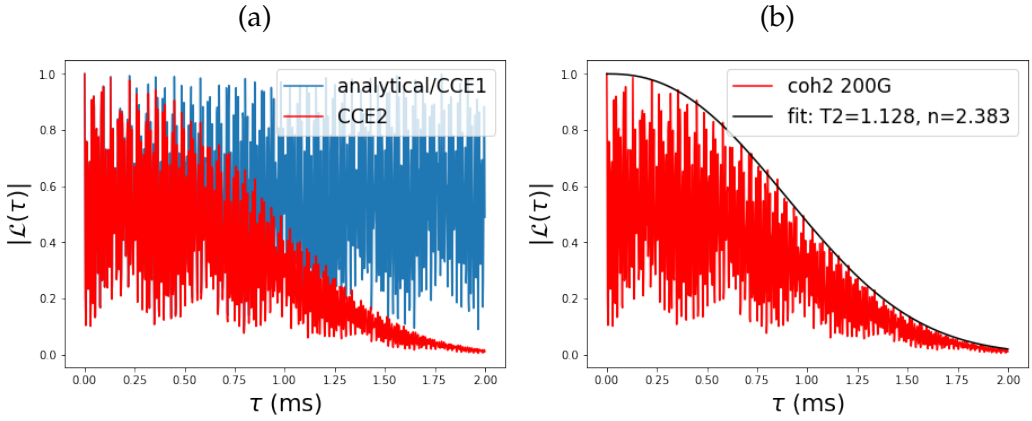

Figure 3.5: Hahn-echo evaluated with CCE1 and CCE2 with semiclassical hyperfine tensor components: absolute value of the coherence of a V_{Si}^0 in 3C-SiC as a function of time, for an external magnetic field of 200 G. The result is averaged over 50 different baths. (a): the blue curve is calculated analytically (Eq. 3.2.26) or at the CCE1 level and the red one is calculated at the CCE2 level. The decoherence time is in the ms range. (b): fitting of the red curve of Fig. 3.5a with an exponential function $e^{-(t/T_2)^n}$. Inset: the optimal values for the fitting parameters T_2, in ms, and n.

is the modulation depth parameter of the i-th nuclear spin between the $|0\rangle$ and $|+1\rangle$ qubit states. Eq. 3.2.26 describes fast oscillations of the qubit coherence, or modulations (see Fig. 3.5), known in the literature as Electron Spin Echo Envelope Modulation (ESEEM), which are due to single nuclear spin transitions [128]. The real part of the coherence is zero also at $t = \tau$ because of the refocusing action of the central π pulse.

Our results on the Hahn-echo extend the findings in Seo et al. [20] to a neutral V_{Si} in 3C-SiC. Indeed the coherence decay is already obtained at the CCE2 level, as shown in Fig. 3.5a (this does not preclude the possibility of having further effects beyond CCE2). The figure shows the qubit coherence as a function of free evolution time, for an external magnetic field of 200 G. The blue curve is calculated at the CCE1 level, and exactly coincides with the analytical curve obtained as a graph of Eq. 3.2.26, as in the FID case. This should be the case since Eq. 3.2.26 is obtained

precisely by following the analytical counterpart of the numerical procedure behind the CCE1 approach, i.e. by neglecting $\mathcal{H}_{n-n}$ in 1.3.5 and thereby considering the coherence as a product of independent contributions coming from each nuclear spin. On the other hand, the red curve in Fig. 3.5 is calculated at the CCE2 level and presents the decay (note the difference with FID, for which CCE1 and CCE2 give similar results). Thus, interactions of the qubit with pairs of coupled nuclear spins within the bath cause a coherence decay that survives to the spin-echo protocol [20]. Furthermore, we demonstrate that the coherence decay of a V_{Si}^{0} is in the ms range (see Fig. 3.5b), whereas for FID it is in the 0.01 ms range (this difference is crucial in QT applications). The figure shows a fitting of the red curve of Fig. 3.5a with a stretched exponential function. The fitting curve's parameters are the Hahn-echo decoherence time and the stretching factor, whose optimal values are $T_2 = 1.13$ ms and $n = 2.38$, respectively. Due to the presence of a stretching factor, we demonstrate that also for a V_{Si} in 3C-SiC the decay of the coherence envelope is not exponential, which is a typical behavior for qubits in NMR/EPR and in general in the solid state. As a matter of fact, this also happens for superconducting qubits, which are usually subjected to $1/f$-type noise from the environment [28].

Then, we have used the *ab initio* calculated values of the hyperfine tensor components listed in Table 1.2 in our CCE code. The comparison of the resulting coherence curve with the semiclassical one, for an external applied magnetic field of 200 G, is shown in Fig. 3.6. The main difference is in the modulation effect, whereas the decay, and hence the decoherence time, is almost unchanged. Again, doing the comparison with FID we see that spin-echo protocols are more robust against the hyperfine tensor components change due to the *ab initio* calibration. This is due to the refocusing π pulse that lifts the dependence on one-body interactions, which are more affected by the *ab initio* calibration. This is in turn due to there being way more one-body interactions where the electron-

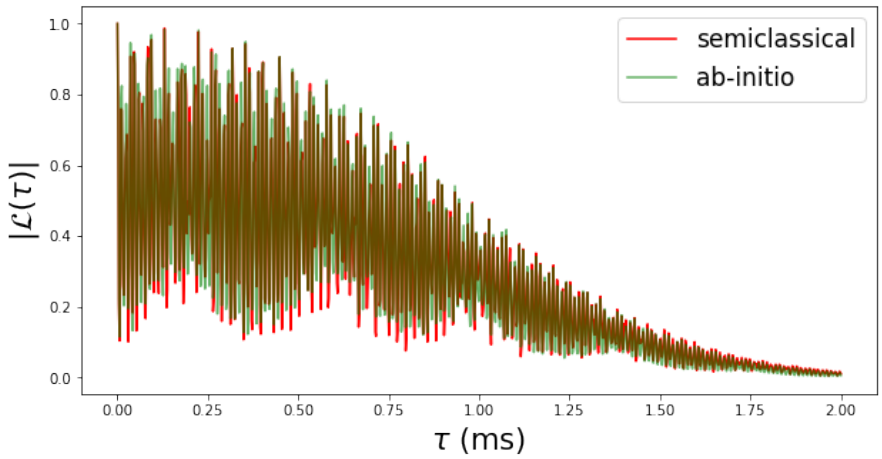

Figure 3.6: Hahn-echo evaluated with CCE2 with semiclassical (Eq. 1.3.9) and *ab initio* (Table 1.2) hyperfine tensor components: absolute value of the coherence of a neutral V_{Si} in 3C-SiC as a function of free evolution time, for an external magnetic field of 200 G. The result is averaged over 50 different baths.

nuclear spin distance is such that the *ab initio* value is used as opposed to two-body interactions where *both* nuclear spins are close enough to require the *ab initio* calibration. This behavior is understood by looking at Eq. 3.2.26, for which a similar reasoning used in the passage from Eq. 3.2.10 to Eq. 3.2.14 can be applied to analytically calculate the modulation frequencies. Those frequencies depend both on the single nuclear spin Larmor frequencies and the hyperfine tensor components through Ω_{I_i}. Therefore, if any of the 50 random baths in a given simulation happens to have a nuclear spin in the first or second neighbor shell, the hyperfine tensor components entering Eq. 3.2.26, and thereby the modulations of the coherence, will be modified. We find the change of the modulation frequencies by using the *ab initio* calibration to be of the same order of magnitude as in the FID case (see the last paragraph of subsection 5.1). As for the decoherence effect, which is at least caused by two-body interactions between nuclear spins (it appears at least at the CCE2 level),

the probability of having two nuclear spins in the first and second neighbor shell is less than the probability of having just one, thus conditioning less the coherence decay. This is a consequence of the chosen numerical random bath-generating procedure.

Chapter 4

Sensing via a Defected 3C-SiC Nanoparticle

4.1 Introduction

Up to now we have focused our work on various kinds of defects in the bulk of WBG semiconductors for applications in nanoelectronics (where they are an issue, Chapter 2) or quantum technologies (where they are a resource, Chapter 3). However, at this point it is quite useful to extend the kind of analysis we carried out in Chapter 3 to the study of our proposed defect (V_{Si}^0) in 3C-SiC *nanoparticles* (with volumes $\sim 300\,\mathrm{nm}^3$). The interest resides in the fact that defected nanostructures can amplify the fields used as external drivers and manifest plasmon or plasma-polariton effects that are interesting for the coupling of those external fields to the defect's evolving states [164, 165]. This has also important biomedical application involving sensing [166, 167]. Furthermore, localized defects in nanoparticle tips are utilized as quantum sensors for thermometry and magnetometry at the nanoscale [168, 169, 170] (mostly employing Nitrogen-Vacancy centers in diamond).

Nanoparticles have different shapes depending on whether the sam-

ple is in a thermodynamic equilibrium state or not [171]. The Equilibrium Crystal Shape (ECS) is *not* reachable during growth and can be obtained by putting the sample in contact with a reservoir of silicon and carbon atoms in thermodynamic equilibrium with it. The ECS can be theoretically predicted by applying the thermodynamic Wulff construction [172, 173]. Kinetic effects stemming from the growth process are due to the intrinsically nonequilibrium nature of the growth itself. These effects change the nanoparticles' shape into what is known in the literature as Kinetic Crystal Shape (KCS). Due to the many different methods that have been developed to carry out a growth process, of which underpotential deposition is just one [174], various theoretical approaches have been devised to tackle the problem and predict the KCS, which is therefore process-dependent. The phase-field approach has been introduced to model the geometric evolution of thin crystalline films [175] and has been successfully applied for the determination of realistic KCS of generic nanoparticles [176], homoepitaxial GaAs fins [177] and faceted crystals [178]. The phase-field approach allows for the evaluation of the growth velocity of each facet involved in the growth process, which as we will see constitutes the main parameter entering the modified thermodynamic Wulff construction [179, 173]. The fundamental parameters that are necessary to determine the ECS and KCS (in a given experimental setting) for 3C-SiC nanoparticles have been evaluated in refs. [180] and [39], respectively. Furthermore, in ref. [181] molecular dynamics simulations predicting the KCS of different initial structures of 3C-SiC nanoparticles are presented. Our goal is then to determine the ECS and KCS (in the experimental setting of Masullo et al. [39]) of a 3C-SiC nanoparticle with a V_{Si}^{0} within it and calculate the defect's (loss of) coherence as a function of free evolution time, for different nanoparticle (and hence bath) shapes and by varying the defect's position inside the nanoparticle. The control technique applied to the defect is the Hahn-echo sequence. On the other hand, FID processes are not applied due to the system's sen-

sitivity to magnetic noise being detrimental in quantum sensing applications [182, 183]. On the flip side, when dealing with quantum sensing applications it is useful to extract from the dynamics, or from its Fourier transform, properties pertaining to the system we are interested in (the bath), so that a strong decoherence could be exploited. That is why this chapter is the most speculative in all the thesis and presents preliminary results.

The rest of the chapter is organized as follows: in Section 4.2 we utilize the Wulff construction to find the 3C-SiC nanoparticle shapes in thermodynamic equilibrium (Subsection 4.2.1) and after a kinetic growth process has been applied (Subsection 4.2.2), both in the Masullo et al. experimental setting and others of our choice. Then, in Section 4.3 we apply the same analysis to a pyramidal nanoparticle. We evaluate the decoherence effect of the qubit in each nanoparticle structure and find the one giving rise to the slowest coherence decay. Finally, in Section 4.4 our conclusions are drawn.

4.2 Wulff Construction for a 3C-SiC Nanoparticle

In order to assess the nanoparticle shape of a given material two methods are most used in the literature, *ab initio* methods and the Wulff construction [184]. The latter is a procedure allowing to construct the shape of a nanoparticle from the knowledge of parameters that can be calculated by using the former method [172].

Inside the nanoparticle, the way in which we model the defect, or electron spin, and describe its interaction with the nuclear spin bath is already reported in Chapter 1 (even though the extension of the bulk analysis to defects in nanoparticles is an assumption at this point). As a summary and to provide additional information, both the electron-nuclear spin and

the nuclear-nuclear spin interaction strengths die off as r^{-3}, where r is the distance between the two objects (see Eq. 1.3.9). Hamiltonian 1.3.3 is already expressed in the pure-dephasing approximation (S_z is the only qubit operator present), in which no qubit transition caused by the interaction with the bath is allowed, and that is justified by the substantial mismatch between the qubit Zeeman term (entering its eigenfrequencies) and the ones of the nuclear spins ($|\gamma_e| \gg |\gamma_i|$ for all i) [32]. The electron spin eigenbasis is $\{|1\rangle, |0\rangle, |-1\rangle\}$, but as a direct consequence of the form of Hamiltonian 1.3.3, by appropriately initializing the electron spin in the $|0\rangle$ state and choosing the control pulses as having precisely the right frequency $\omega_1 = D + \gamma_e B_z$, the $|-1\rangle$ state can be taken out of the dynamics since no transitions are allowed towards it (thus the electron spin behaves as a qubit).

4.2.1 Equilibrium Crystal Shape

The first classical version of Wulff construction that has been introduced in the literature is the *thermodynamic* Wulff construction [173], which is a recipe for constructing the shape of a nanoparticle put in thermodynamic equilibrium contact with a reservoir of its constituent atoms. From the experimental point of view such shape cannot be obtained during the growth process, which is not an equilibrium process and introduces kinetic effects altering the shape. Therefore, after a nanoparticle has been grown, a contact with a silicon and carbon atom reservoir at the same temperature but different chemical potential is necessary to ensure the emergence of those facets with the *lowest* surface energy density. This is precisely an energy *minimization* process. It is thereby not surprising that the parameters needed for the determination of the ECS are the surface energy density $\gamma_{(lmn)}$ of each facet involved. In its original formulation, the thermodynamic Wulff construction states that the normal vector length $h_{(lmn)}$ to the generic (lmn) facet manifesting itself in the equilib-

rium shape is proportional to the facet's surface energy density [173],

$$\gamma_{(lmn)} = \frac{h_{(lmn)}}{\lambda}, \tag{4.2.1}$$

where $h_{(lmn)}$ is the normal distance from the center of the nanoparticle (Wulff point) to the (lmn) facet and λ is a constant accounting for volume. Consequently, the ECS is obtained as the inner envelope of those planes defined through their normal vectors $\vec{h}_{(lmn)}$ [172],

$$S_w = \left\{ \vec{r} : \vec{r} \cdot \hat{n} = \lambda \gamma_{\hat{n}} \text{ for all unit vectors } \hat{n} \right\}, \tag{4.2.2}$$

where $\hat{n} = (l, m, n)/\sqrt{l^2 + m^2 + n^2}$. Thus, we have generated the nuclear spins within a 3C-SiC nanoparticle in the equilibrium shape via the same procedure as for the pyramidal one (Section 4.3). What remains to do is to calculate the surface energy density of the most important low-index facets. Precisely this has been done in ref. [180], where the surface energy densities are calculated via *ab initio* methods to be $\gamma_{(111)} = 19\,\mathrm{eV/nm^2}$ (Si-terminated), $\gamma_{(\bar{1}\bar{1}\bar{1})} = 21\,\mathrm{eV/nm^2}$ (C-terminated), $\gamma_{(001)} = 15\,\mathrm{eV/nm^2}$ and $\gamma_{(110)} = 21\,\mathrm{eV/nm^2}$.

The equilibrium nanoparticle shape obtained by using these *ab initio* data for the surface energy density is shown in Fig. 4.1. The volume constant appearing in Eq. 4.2.2 and describing, along with the surface energy densities, the volume of the nanoparticle is chosen to be $\lambda = 0.25\,\mathrm{nm}^3$. The final volume itself, depending also on the $\gamma_{(lmn)}$ parameters, is approximately equal to $290\,\mathrm{nm}^3$ for a nanoparticle containing ~ 20000 atoms. In Fig. 4.2 we show our results on the absolute value of the qubit coherence as a function of free evolution time. The application of CCE theory for defects in nanostructures is debatable at this point and we would have liked to justify it by means of a realistic model. However, a tentative initial support for our assumption, to be confirmed by theoretically/computationally experimenting with it, comes from the theory's high convergence property with respect to small baths [32] (which proves

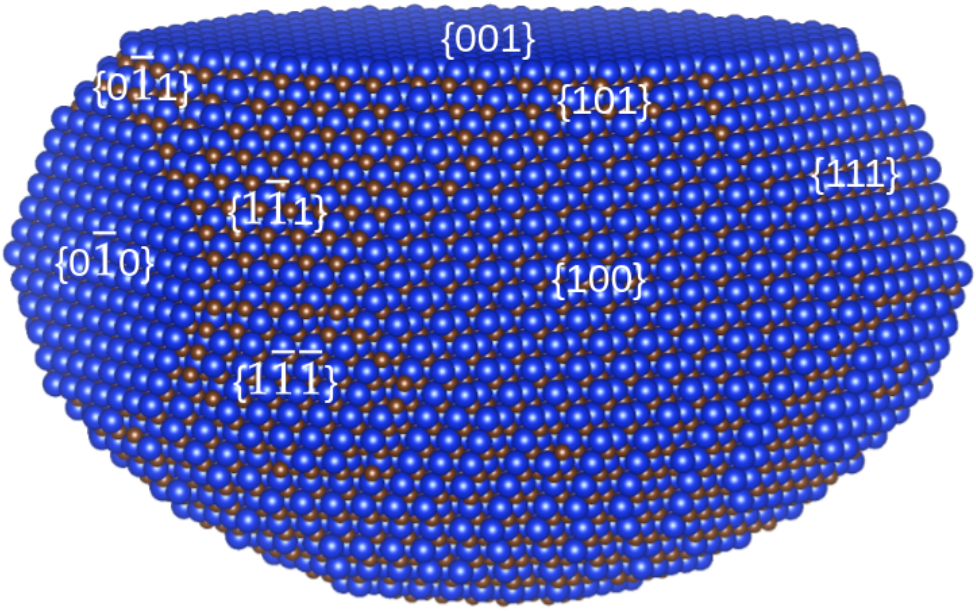

Figure 4.1: Atomic structure of the equilibrium crystal shape of a 3C-SiC nanoparticle attached to the bulk of the material. The cutting planes are obtained via Eq. 4.2.2 with the surface energy density *ab initio* data taken from Filimonov et al. [180], and are the {111}, {001} and {110} facets.

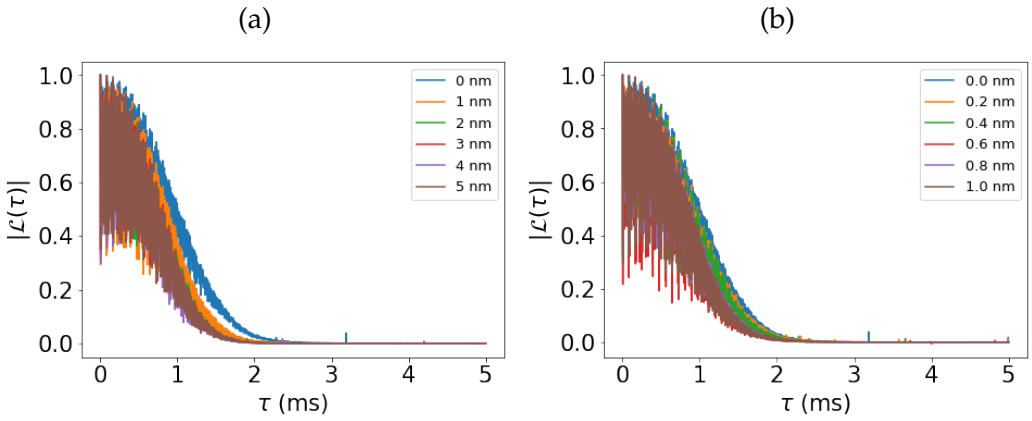

Figure 4.2: Hahn-echo evaluated with CCE2: absolute value of the coherence of a neutral V_{Si} in the equilibrium crystal shape of a 3C-SiC nanoparticle as a function of free evolution time. The external magnetic field is 430 G. The curves are averaged over 50 different baths. (a) The qubit-edge distance is varied from 0 to 5 nm with a 1 nm increment. (b) Zoom in the region near the edge with a 0.2 nm increment.

its applicability in these cases). Another assumption we make regards the usefulness of Hahn-echo techniques for sensing, which is certainly a source of further work, combined with a rigorous quantitative analysis of the time scales entering the decay and how it is different from the FID case (as we did in Chapter 3). For simplicity of implementation, this time the *qubit-edge* distance is what differentiates one curve from the other in Fig. 4.2. This is the reason why the blue curve shows the slowest decay, being the one in which the qubit is surrounded by the less numerous nuclear spin bath. Note also that the jump in the coherence function, which for the pyramidal nanoparticle occurs between the 0.6 and the 0.4 nm curve, for the equilibrium shape occurs between the 1.0 and the 0.0 nm curve. This is due to the ECS having way less sharp edges with respect to the pyramidal nanoparticle (see below), and thereby having way more room for nuclear spins in the bath (cfr. Figs. 4.7b and 4.1).

4.2.2 Kinetic Crystal Shape

Before being able to reach the equilibrium shape of a nanoparticle of a given material in the laboratory, one has to grow that nanoparticle by exploiting a specific protocol whose end result differs from the ECS due to kinetic effects being accumulated in the process [177, 178]. In order to theoretically predict the KCS, a modified version of the Wulff construction has been introduced, which is known in the literature as *modified* thermodynamic Wulff construction [172, 173]. The idea behind it is similar to that of the original thermodynamic Wulff construction, the only differences being the substitution of the surface energy densities with the growth velocities of each facet involved and the introduction of the time parameter. The edge facets corresponding to the kinetic shape can be obtained via [173]

$$S_K = \{\vec{r} : \vec{r} \cdot \hat{n} = \lambda(t) v_{\hat{n}} \text{ for all unit vectors } \hat{n}\}\,, \tag{4.2.3}$$

where $v_{\hat{n}}$ is the orientation-dependent growth velocity and the nanoparticle volume constant depends on time, as it should be for a growth process. Despite the growth process being a time-dependent phenomenon, in specific experimental situations, in which the growth time frame is way longer than the kinetic effects time frame, it can be regarded as stationary. In particular, that is the case in ref. [39], whose growth velocities relative to that of the (111) facet (chosen as unitary), $v_{(\bar{1}\bar{1}\bar{1})} = 3.12$, $v_{(001)} = 1.82$ and $v_{(110)} = 5.55$, are used in this chapter to determine the KCS.

The result for the kinetic nanoparticle shape is shown in Fig. 4.3. The nanoparticle volume constant has been chosen to be $\lambda = 0.035\,\mathrm{nm}^3$ in order to obtain a similar final volume to that of the nanoparticle in thermodynamic equilibrium. In Fig. 4.4 we show our results on the absolute value of the qubit coherence for the kinetic shape of the nanoparticle. An important thing to note is the fact that Fig. 4.4a shows a slower decay for the blue curve with respect to the equivalent one in the ECS case.

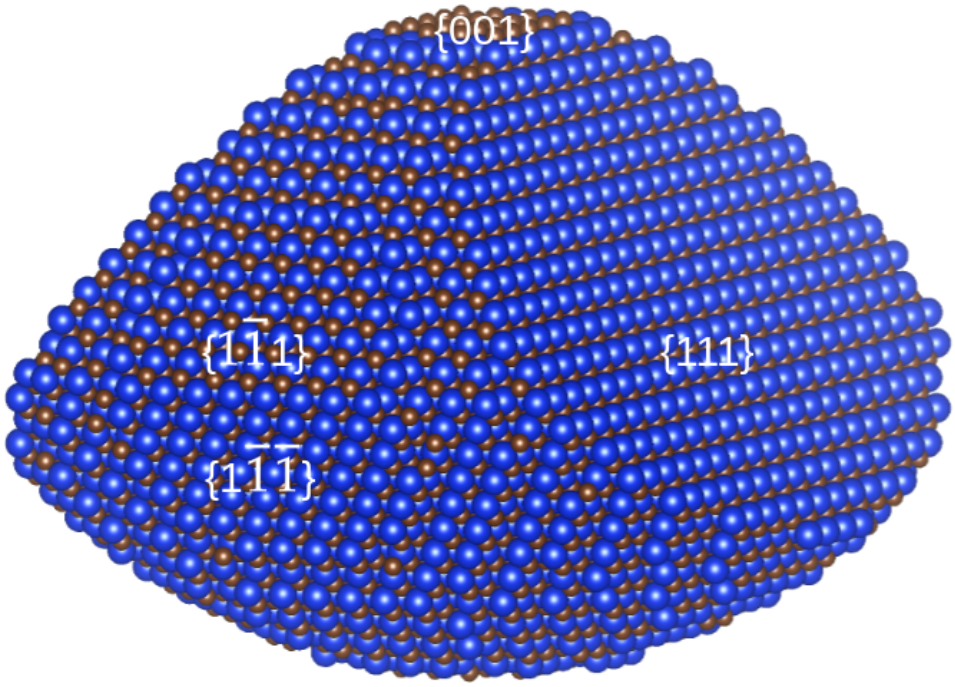

Figure 4.3: Atomic structure of the kinetic crystal shape of a 3C-SiC nanoparticle attached to the bulk of the material. The cutting planes are obtained via Eq. 4.2.3 with the growth velocity data taken from Masullo et al. [39], and are the $\{111\}$ and $\{001\}$ facets.

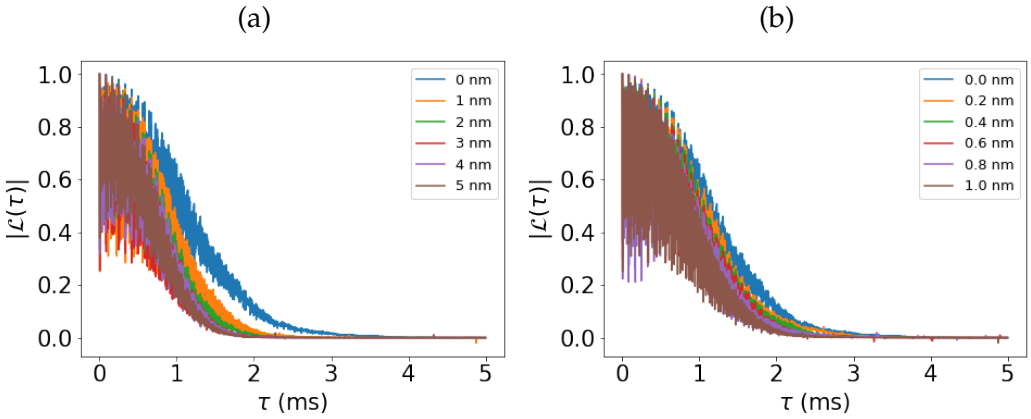

Figure 4.4: Hahn-echo evaluated with CCE2: absolute value of the coherence of a neutral V_{Si} in the kinetic crystal shape (in the experimental conditions of Masullo et al. [39]) of a 3C-SiC nanoparticle as a function of free evolution time. The external magnetic field is 430 G. The curves are averaged over 50 different baths. (a) The qubit-edge distance is varied from 0 to 5 nm with a 1 nm increment. (b) Zoom in the region near the edge with a 0.2 nm increment.

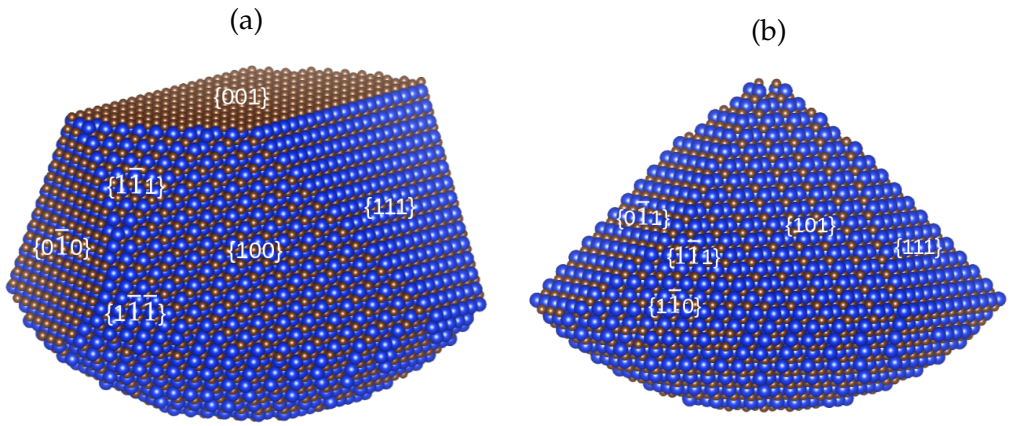

Figure 4.5: Atomic structures of 3C-SiC nanoparticles attached to the bulk of the material. The cutting planes are obtained via Eq. 4.2.3. (a) The relative growth velocities are $v_{(\bar{1}\bar{1}\bar{1})} = 3.12$, $v_{(001)} = v_{(111)} = 1$ and $v_{(110)} = 5.55$, a modified version of the ones from Masullo et al. [39]. (b) The relative growth velocities are $v_{(\bar{1}\bar{1}\bar{1})} = 3.12$, $v_{(001)} = 1.82$ and $v_{(110)} = v_{(111)} = 1$.

That is the result of the kinetic nanoparticle being more peaked than the equilibrium one in the negative direction of the z axis (cfr. Figs. 4.2a and 4.4a). Therefore, the results suggest that the kinetic shape is structurally halfway between the equilibrium shape and the pyramidal one, analyzed in the next section.

The next question we posed ourselves involved how we can depart from the experimental conditions in Masullo et al. [39] to be able to investigate other interesting kinetic shapes with our theoretical analysis. In order to do that we have tweaked the growth velocity parameters in our simulations until we obtained two visibly different structures with respect to the KCS. First we have lowered the growth velocity corresponding to the (001) facet so that $v_{(001)} = v_{(111)}$ and left the other ones unchanged. Then we proceeded by doing the same thing for the growth velocity associated to facet (110). The atomic structures we have thus obtained are shown in Figs. 4.5a and 4.5b, respectively. Our results on the absolute value of the qubit coherence are instead shown in Fig. 4.6. In the first row we present the results for the first modified kinetic shape, for which the similarity with the ECS results of Fig. 4.2 is immediately clear. This is due to the two structures being fairly similar, with the kinetic one differing only in the slightly sharper (001) facet (cfr. Figs. 4.5a and 4.1). The results for the second modified kinetic shape are instead shown in the second row of Fig. 4.6, and are way more similar to that of the initial kinetic shape of Fig. 4.4 and to that of the pyramidal nanoparticle (Fig. 4.8). This is due to this structure being way sharper than the one depicted in Fig. 4.5a. Therefore, this study suggests the use of nanoparticles with sharp tips in sensing experiments, the sharpest being the pyramidal one. This is due to the fact that a qubit within them has an increased comparative response to the number of nuclear spins surrounding it with respect to the same qubit in other types of structures. Out of the kinetic shapes we have taken into account the one whose relative growth velocities are $v_{(\bar{1}\bar{1}\bar{1})} = 3.12$, $v_{(001)} = 1.82$ and $v_{(110)} = v_{(111)} = 1$ is the closest one to

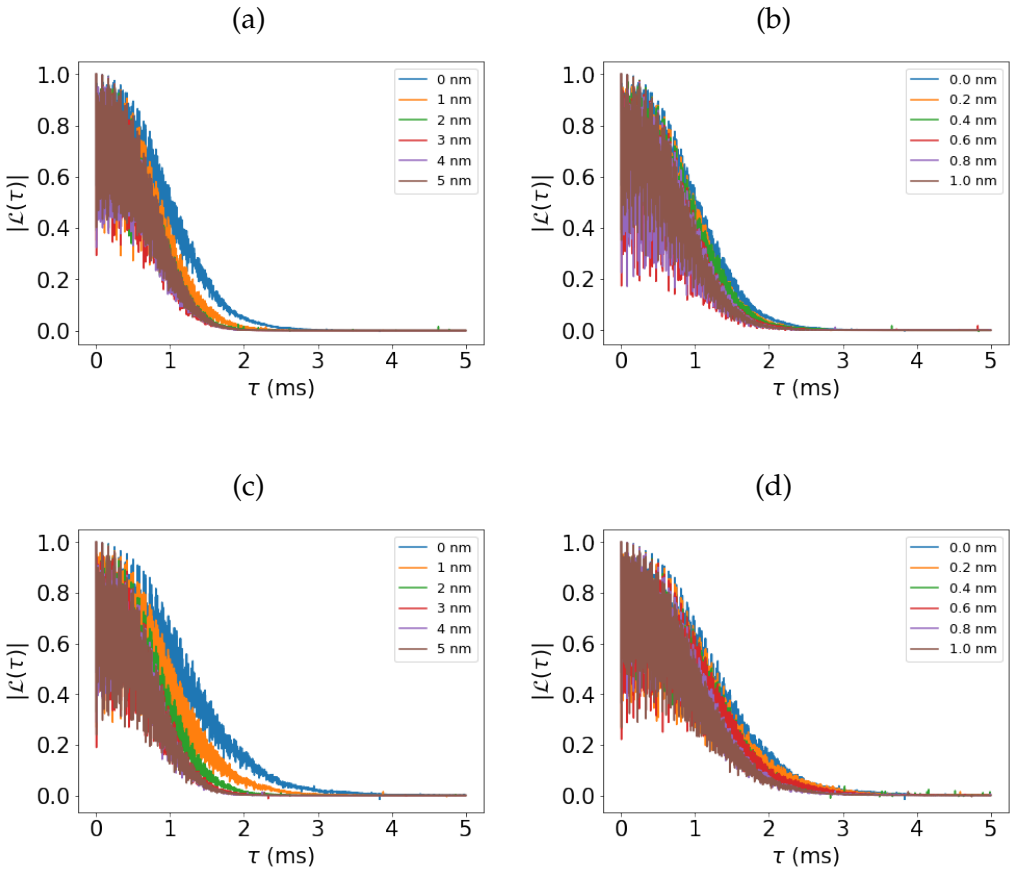

Figure 4.6: Hahn-echo evaluated with CCE2: absolute value of the coherence of a neutral V_{Si} in two modified versions of the KCS (in the experimental conditions of Masullo et al. [39]) of a 3C-SiC nanoparticle as a function of free evolution time. The external magnetic field is 430 G. The curves are averaged over 50 different baths. (a-b) The relative growth velocities are $v_{(\bar{1}\bar{1}\bar{1})} = 3.12$, $v_{(001)} = v_{(111)} = 1$ and $v_{(110)} = 5.55$. (c-d) The relative growth velocities are $v_{(\bar{1}\bar{1}\bar{1})} = 3.12$, $v_{(001)} = 1.82$ and $v_{(110)} = v_{(111)} = 1$.

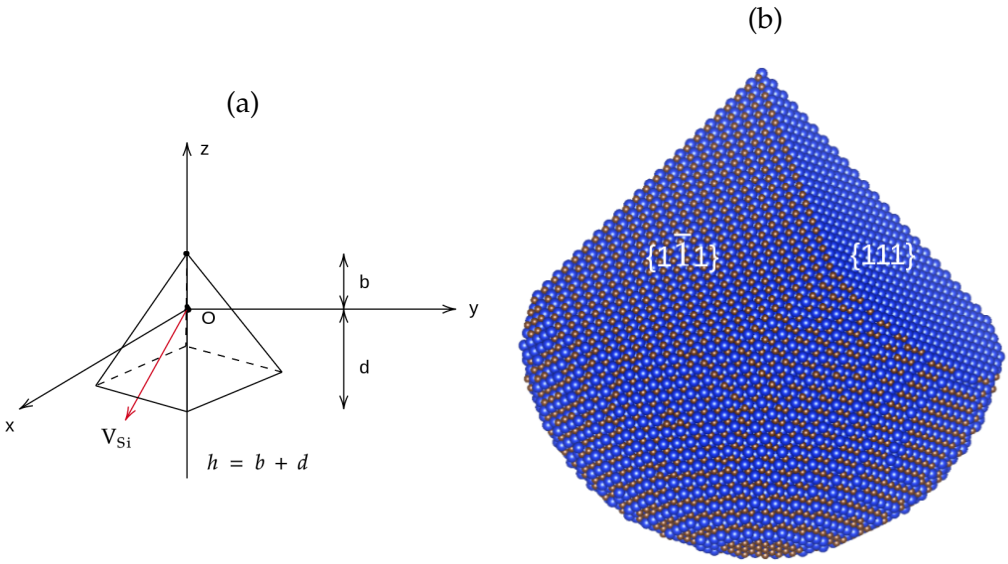

Figure 4.7: (a) Schematic drawing of the pyramidal 3C-SiC nanoparticle without the bulk part. The height of the nanoparticle is divided up into the base-qubit distance b and the qubit-top distance d, with the qubit located at the origin of the coordinate system. The visible triangular facets are $\{111\}$ and $\{1\bar{1}1\}$. (b) Atomic structure of the pyramidal 3C-SiC nanoparticle attached to the bulk of the material.

the behavior of the pyramidal nanoparticle. As a consequence of our results, we propose an experiment in which the nanoparticle in Fig. 4.5b is constructed and then utilized to sense the presence of nearby nuclear spins and thereby assess their concentration in unknown materials under study. One possible strategy to perform measurements of a qubit coherence has been adopted in ref. [20], which has been our main inspiration for the application of CCE theory to deal with our system's dynamics. Our proposal is to generalize Seo's coherence measurements to a qubit in the tip of our nanoparticle in Fig. 4.5b for nuclear spin bath sensing applications.

4.3 Pyramidal Nanoparticle

Another important nanoparticle shape we analyze is the pyramidal one, and in this choice we are inspired by the typical form of the tip of the instruments in Atomic Force Microscopy (AFM) experiments [185, 186, 187]. A schematic view of the pyramidal nanoparticle can be found in Fig. 4.7a. Here the four triangular facets are directed towards the $[111]$, $[1\bar{1}1]$, $[\bar{1}\bar{1}1]$ and $[\bar{1}11]$ directions, respectively, and for simplicity the bulk of the material in the $[00\bar{1}]$ direction is not shown. Moreover, the height of the nanoparticle is $h = b + d$, where b is the bulk-qubit distance, d is the qubit-tip distance and the qubit is located at the origin of the coordinate system. In Fig. 4.7b we show the atomic structure of the nanoparticle attached to the bulk of the material. Then, the question is how the variation of the coherence function in time will change as a result of the different nanoparticle shapes we will consider, and hence of the different nuclear spin bath configuration, and as a result of the different location of the qubit within the nanoparticle.

Finally, our results on the decoherence of a neutral V_{Si} in a pyramidal 3C-SiC nanoparticle are shown in Fig. 4.8. In Fig. 4.8a we show the absolute value of the qubit coherence as a function of free evolution time (introduced in Eq. 3.2.24), for an external magnetic field of 430 G. Six different curves are shown in which the qubit is ever closer to the tip of the pyramidal nanoparticle. Fig. 4.8b shows instead how the decoherence effect is affected by the proximity of the qubit to the tip of the nanoparticle. As can be clearly seen, the farther the qubit is from the bulk the fewer are the nuclear spins surrounding it, and that is reflected by the loss of coherence being more pronounced for the blue curve with respect to the maroon one. Note also that decoherence is not completely finished after 5 ms for the 5 nm curve. Furthermore, there is a visible jump between the green and the red curve in Fig. 4.8b, which indicates that the nuclear spins interacting more strongly with the qubit (the closest ones [16]) are no longer present. Therefore, in this study we propose to exploit defects

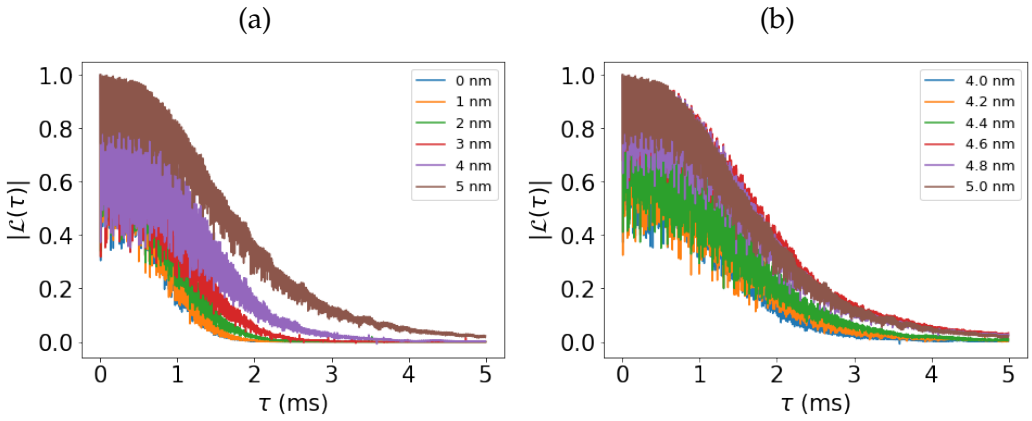

Figure 4.8: Hahn-echo evaluated with CCE2: absolute value of the coherence of a neutral V_{Si} in a pyramidal 3C-SiC nanoparticle as a function of free evolution time. The external magnetic field is 430 G. The curves are averaged over 50 different baths. (a) The bulk-qubit distance is varied from 0 to 5 nm with a 1 nm increment. (b) Zoom in the region near the tip with a 0.2 nm increment.

in 3C-SiC nanoparticles for sensing applications in AFM experiments. In particular, by performing coherence measurements of a defect in the tip of the instrument, alone and in contact with a material whose paramagnetic nuclei's concentration is unknown, one could have a sense of the number of naturally occurring isotopes by measuring a drop in the decoherence time.

4.4 Discussion

In conclusion, in this chapter we have generalized the approach we have followed in other studies [15, 16] to defected 3C-SiC nanoparticles, on the basis of an educated guess. The approach consists in applying the Hahn-echo sequence on a qubit (or defect) within the nanoparticle and using CCE theory to model the dynamics of the qubit interacting with the nuclear spin bath, resting on the assumption that it works well for small

baths (as we see in ref. [32]). First we applied the thermodynamic and modified thermodynamic Wulff construction to obtain the proper 3C-SiC nanoparticle shape in thermodynamic equilibrium and after a particular growth process (here we choose the one from ref. [39]), respectively. For what concerns the ECS, we noticed that the jump in the coherence function occurs farther from the edge with respect to the pyramidal nanoparticle. This is due to the ECS having way less sharp edges with respect to the pyramidal nanoparticle, and thereby having way more room for nuclear spins in the bath. Therefore, we found that the nuclear spin bath reduction that takes place in 0.2 nm in the pyramidal nanoparticle, in the equilibrium one occurs in 1.0 nm. Moving on to the KCS, we found that the corresponding coherence curves show a slower decay with respect to the equivalent ones in the ECS case. That is the result of the kinetic nanoparticle being more peaked than the equilibrium one in the negative direction of the z axis, suggesting that the kinetic shape is structurally halfway between the equilibrium shape and the pyramidal one. Then we modified Masullo's KCS by varying the relative growth velocity of each facet, until we obtained two visibly different atomic structures (Fig. 4.5). For the first modified kinetic shape the relative growth velocities are $v_{(\bar{1}\bar{1}\bar{1})} = 3.12$, $v_{(001)} = v_{(111)} = 1$ and $v_{(110)} = 5.55$. For this shape the coherence results show a strong similarity with that of the ECS, due to their similar atomic structures. On the other hand, for the second modified kinetic shape the relative growth velocities are $v_{(\bar{1}\bar{1}\bar{1})} = 3.12$, $v_{(001)} = 1.82$ and $v_{(110)} = v_{(111)} = 1$. The associated coherence results are way more similar to that of Masullo's KCS and to that of the pyramidal nanoparticle, due to the similar structures with sharper edges. Then we showed our results on the pyramidal nanoparticle itself, taking inspiration by the tip of the instrument in AFM experiments. We have found that there is a visible jump between the green and the red curve in Fig. 4.8b, which indicates that the nuclear spins interacting more strongly with the qubit are not present due to the sharpness of the nanoparticle's (001) facet.

Ours are only preliminary results that (if confirmed) suggest the use of nanoparticles with sharp tips in sensing experiments, the sharpest being the pyramidal one. That is because a qubit within them has less neighboring nuclear spins of the nanoparticle with respect to the same qubit in other types of structures (and equivalently the closest nuclear spins will be the ones from the material under study in a sensing experiment).

Conclusions

In conclusion, we have studied point-defects in wide band gap semiconductors from two different points of view, in the nanoelectronics realm (where they cause issues) and in the quantum technology one (where they are a resource).

In nanoelectronics, the Car-Parrinello molecular dynamics and the nudged elastic band method have been used to show that Aluminum Frenkel defects may form bistable centers that can act as traps of electrical charges in disordered and stoichiometric α-Al_2O_3. Furthermore, the application of a polaronic model representing a distribution of individually interacting energy levels with an internal reconfiguration mode and coupled to continuous bands of carriers has shown that such trap states can explain the hysteresis mechanism in the C-V measurements of Al_2O_3/AlGaN capacitors. We acknowledge that this bistable hysteretic behavior can emerge from different types of oxide defects, whose experimental and theoretical investigation could enhance the understanding of MOS devices based on the Al_2O_3 gate dielectric.

In quantum technology, we have used DFT through the quantum espresso code to study the formation energy of the silicon vacancy in 3C-SiC, analyzing its charge states and finding their range of stability as a function of the Fermi level. Thus, we have demonstrated that the less studied neutral charge state of the V_{Si} is the most stable for *p*-doped

3C-SiC samples. Moreover, our results on the hyperfine tensor show important deviation with respect to the semiclassical estimates of the model parameters obtained with Eq. 1.3.9. We have studied both Hahn spin-echo and FID as protocols applied to our qubit, finding the equations (Eqs. 3.2.9 and 3.2.10) that describe FID when the nuclear spins are non-interacting with each other. By appropriately rewriting those equations we have been able to analytically calculate the FID modulation frequencies and associate them to the system's eigenenergies, and thus to its magnetic parameters. Furthermore, by applying the CCE theory by means of our code we have shed light within reliable approximations on the ESEEM phenomenon and the decoherence of the spin associated to the defect when Hahn spin-echo protocols are applied to the system, or after free evolution. The estimated V_{Si} decoherence time in 3C-SiC after Hahn-echo is in the milliseconds range, thus gaining at least two orders of magnitude with respect to FID. We have also evaluated the non-exponential character of the coherence decay, which is typical for qubits in solid-state devices. Finally, for the Hahn-echo we have demonstrated that modeling the 3D distribution of the spin density in the vicinity of the qubit in our CCE simulations, by using *ab initio* methods, has an effect on the coherence modulations known as the ESEEM phenomenon, but not as much on the decoherence effect. For the FID process the effect is instead more pronounced.

For what concerns the defected 3C-SiC nanoparticles, our preliminary results suggest the use of nanoparticles with sharp tips in sensing experiments, the sharpest being the pyramidal one. That is because a qubit within them has less neighboring nuclear spins of the nanoparticle with respect to the same qubit in other types of structures (and equivalently the closest nuclear spins will be the ones from the material under study in a sensing experiment).

Appendix A

Supplemental material on the simulations

In this Appendix we are going to present all the results on the convergence of the parameters entering our simulations.

First of all, in Fig. A.0.1 we show the dependence of the coherence on the axial component D in a FID process. Since in our CCE code the Hamiltonian is written in the pure-dephasing approximation from the start, these results are obtained by using the PyCCE code from the Galli group [188]. As can be seen from the figure, by adding $E = -0.41\,\mathrm{MHz}$ (right panel) the result does not change appreciably, so that our choice of neglecting E is justified. Then, in Fig. A.0.2 we have studied the dependence of the coherence on the radius of the spherical bath R_{bath} at the CCE1 level, which is sufficient for analyzing FID.

From the figure we see that already for a bath with a radius of dimension $R_{\mathrm{bath}} = 2.5\,\mathrm{nm}$ the result is almost completely converged, justifying our choice of $R_{\mathrm{bath}} = 5\,\mathrm{nm}$. It is important to stress here that in the context of CCE simulations convergence has been established qualitatively by identifying the coherence curve which does not appreciably deviate from the ones at lower and higher value associated to the parameter to be converged, as in ref. [20].

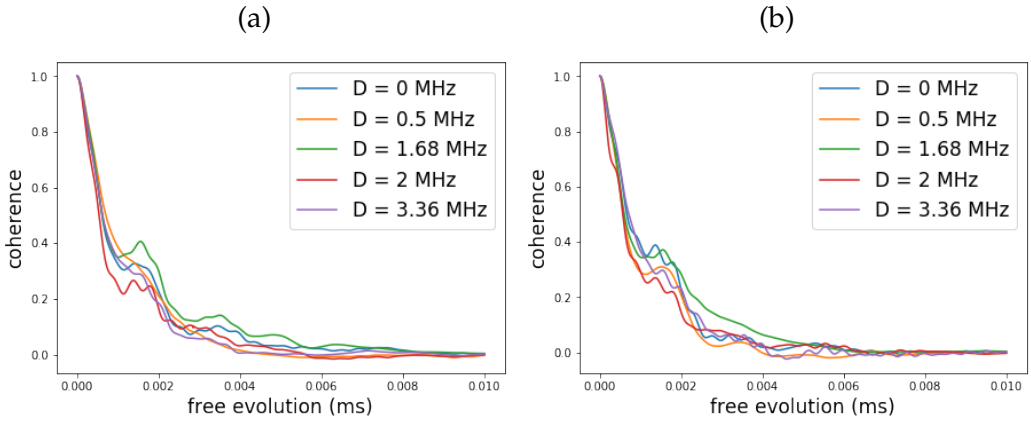

Figure A.0.1: CCE2 absolute value of the coherence of a neutral V_{Si} in 3C-SiC as a function of free evolution time, with different values for the axial component D of the ZFS tensor, for an external magnetic field of 500 G. The dynamics implemented is a free evolution, or FID process, and the results are averaged over 50 different baths. (a): the transversal component E of the ZFS tensor is absent. (b): the transversal component E of the ZFS tensor is present ($E = -0.41$ MHz). The curves are obtained with the PyCCE code from the Galli group [188].

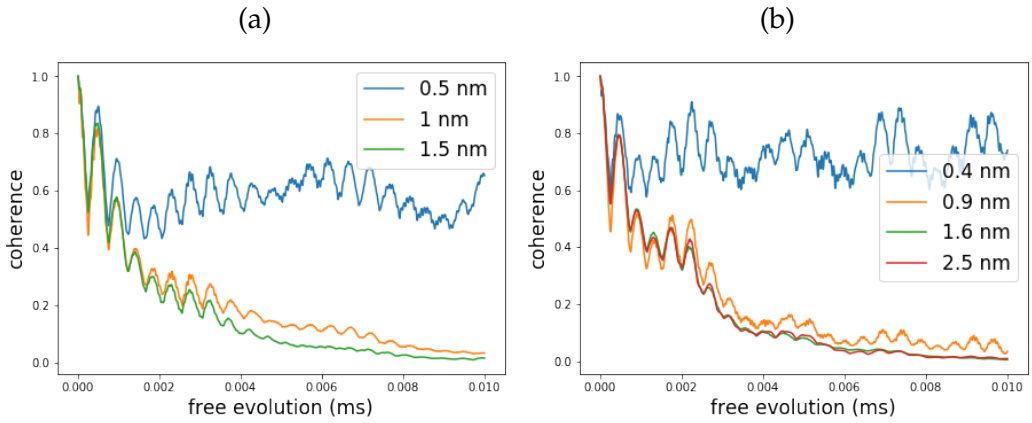

Figure A.0.2: CCE1 absolute value of the coherence of a neutral V_{Si} in 3C-SiC as a function of free evolution time, with different values for the radius of the spherical bath R_{bath}, for an external magnetic field of 340 G (a) and 500 G (b). The dynamics implemented is a free evolution, or FID process, and the results are averaged over 50 different baths.

Finally, in Fig. A.0.3 we show the dependence of the coherence on the number of realizations of the bath $\mathcal{N}$, again at the CCE1 level and for a reduced bath of $R_{\text{bath}} = 4$ nm. Note that already a mean over 50 different baths is sufficient to obtain a reasonably well-converged coherence curve, which is why we choose $\mathcal{N} = 50$ in the main body of the thesis.

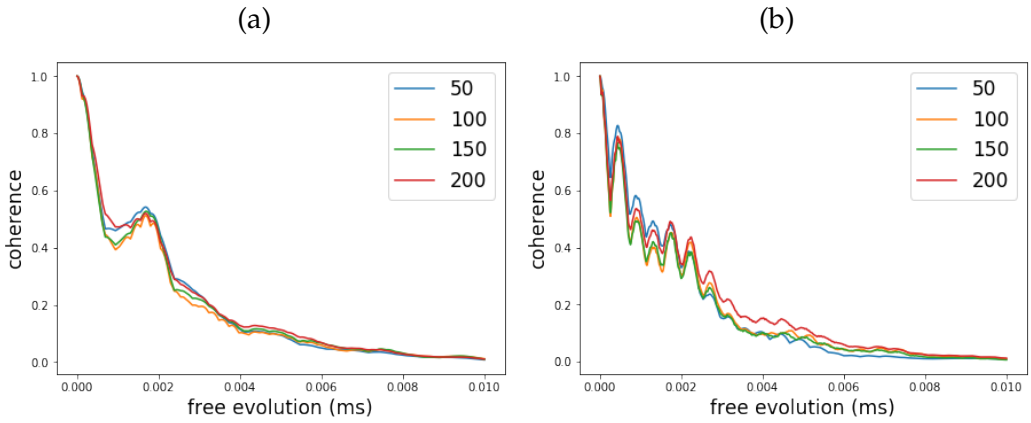

Figure A.0.3: CCE1 absolute value of the coherence of a neutral V_{Si} in 3C-SiC as a function of free evolution time, with different values for the number of bath realizations $\mathcal{N}$, for an external magnetic field of 500 G. The dynamics implemented is a free evolution, or FID process, and the radius of the spherical bath is $R_{\text{bath}} = 4\,\text{nm}$. (a): the hyperfine tensor components are calculated via Eq. 1.3.9. (b): the hyperfine tensor components are calculated via *ab initio* methods based on DFT (Table 1.2).

Appendix B

Induction considerations

In this appendix we give a non-rigorous derivation of Eq. 3.2.15 of the main text, starting from Eq. 3.2.11, by exploiting induction considerations.

Let's start by considering the case where there is a single nuclear spin in our bath, i.e. $n = 1$. In this case, by using trigonometric formulas, Eq. 3.2.11 can be written as

$$\Sigma_1(\tau) = \frac{1}{2}\left(S_{I_1}\cos\left[\left(\frac{\omega_{I_1}}{2} - \frac{\Omega_{I_1}}{2}\right)\tau\right] + D_{I_1}\cos\left[\left(\frac{\omega_{I_1}}{2} + \frac{\Omega_{I_1}}{2}\right)\tau\right]\right), \tag{B.0.1}$$

and thus we have two terms and two modulation frequencies, one for each term. In the case $n = 2$ we have instead four terms and eight modulation frequencies, two for each term, as can be seen by the following

formula:

$$\Sigma_2 = \frac{1}{8}\Bigg\{ S_{I_1} S_{I_2}\Bigg[\cos\Big[\Big(\frac{\omega_{I_1}}{2} - \frac{\Omega_{I_1}}{2} + \frac{\omega_{I_2}}{2} - \frac{\Omega_{I_2}}{2}\Big)\tau\Big] + \cos\Big[\Big(\frac{\omega_{I_1}}{2} - \frac{\Omega_{I_1}}{2} - \frac{\omega_{I_2}}{2} + \frac{\Omega_{I_2}}{2}\Big)\tau\Big]\Bigg]$$
$$+ S_{I_1} D_{I_2}\Bigg[\cos\Big[\Big(\frac{\omega_{I_1}}{2} - \frac{\Omega_{I_1}}{2} + \frac{\omega_{I_2}}{2} + \frac{\Omega_{I_2}}{2}\Big)\tau\Big] + \cos\Big[\Big(\frac{\omega_{I_1}}{2} - \frac{\Omega_{I_1}}{2} - \frac{\omega_{I_2}}{2} - \frac{\Omega_{I_2}}{2}\Big)\tau\Big]\Bigg]$$
$$+ D_{I_1} S_{I_2}\Bigg[\cos\Big[\Big(\frac{\omega_{I_1}}{2} + \frac{\Omega_{I_1}}{2} + \frac{\omega_{I_2}}{2} - \frac{\Omega_{I_2}}{2}\Big)\tau\Big] + \cos\Big[\Big(\frac{\omega_{I_1}}{2} + \frac{\Omega_{I_1}}{2} - \frac{\omega_{I_2}}{2} + \frac{\Omega_{I_2}}{2}\Big)\tau\Big]\Bigg]$$
$$+ D_{I_1} D_{I_2}\Bigg[\cos\Big[\Big(\frac{\omega_{I_1}}{2} + \frac{\Omega_{I_1}}{2} + \frac{\omega_{I_2}}{2} + \frac{\Omega_{I_2}}{2}\Big)\tau\Big] + \cos\Big[\Big(\frac{\omega_{I_1}}{2} + \frac{\Omega_{I_1}}{2} - \frac{\omega_{I_2}}{2} - \frac{\Omega_{I_2}}{2}\Big)\tau\Big]\Bigg]\Bigg\}. \tag{B.0.2}$$

By analyzing Eqs. B.0.1 and B.0.2 we find some common behaviors that allow us to infer the form of the equation valid in the general $n = N$ case to be exactly Eq. 3.2.15. Furthermore, in the general case we have 2^N terms and 2^{2N-1} modulation frequencies, 2^{N-1} for each term. The number of terms and the number of frequencies per term are not random, and can be understood, or counted, as the number of ways in which we can dispose N elements from a set of 2 elements, where the same element can be repeated at most N times (they are thus called dispositions with repetitions). For what concerns the number of terms we have to dispose N elements from the set of values $\{S_{I_i}, D_{I_i}\}$ they can take, with a maximum of N possible repetitions. The number of these dispositions is precisely 2^N. Instead, for the number of frequencies per term we have to dispose $N-1$ *pairs* of elements (pairs of signs), all but the first one, from the set of values $\{+,-\}$ they can take, with a maximum of $N-1$ possible repetitions, *fixing* at the same time the first pair to a $(+-)$ if the term they are multiplied by starts with an S or to a $(++)$ if the term they are multiplied by starts with a D. Since the cosine is an even function, we can make the opposite choice, $S \longrightarrow (-+)$ and $D \longrightarrow (--)$, but also in this case the rules remain the same and nothing changes, so that it is a matter of taste.

Finally, we give the version of Eq. 3.2.14 in which also the $\cos(\omega_1\tau)$

term is put inside of Σ_N, i.e.

$$\begin{aligned}
\langle S_y \rangle = \frac{1}{2^{2N}} \Big\{ & S_{I_1} \cdots S_{I_N} \Big[(-+-+\ldots-+) + \ldots + (-++-\ldots+-) \\
& + (+--+\ldots-+) + \ldots + (+-+-\ldots+-) \Big] \\
& + S_{I_1} \cdots D_{I_N} \Big[(-+\ldots-+--) + \ldots + (+-\ldots+---) \\
& + (-+\ldots-+++) + \ldots + (+-\ldots+-++) \Big] + \ldots \\
& + S_{I_1} \cdots D_{I_i} \cdots D_{I_N} \Big[(-+\ldots--\ldots--) + \ldots + (+-\ldots--\ldots++) \\
& + (-+\ldots++\ldots--) + \ldots + (+-\ldots++\ldots++) \Big] + \ldots \\
& + D_{I_1} \cdots D_{I_N} \Big[(----\ldots--) + \ldots + (--++\ldots++) \\
& + (++--\ldots--) + \ldots + (++++\ldots++) \Big] \Big\},
\end{aligned} \tag{B.0.3}$$

where now a new notation is used,

$$(+-\ldots+-) \equiv \cos\left[\left(\omega_1 + \omega_{I_1}/2 - \Omega_{I_1}/2 + \ldots + \omega_{I_N}/2 - \Omega_{I_N}/2\right) \tau \right]. \tag{B.0.4}$$

In this case there are 2^{2N} modulation frequencies, thus their number being doubled in size, as noticed in the main text. Furthermore, each of the final modulation frequencies appearing in Eq. B.0.3 can be written as a linear combination of the eigenvalues of the pure-dephasing Hamiltonian, given in Eq. 1.3.3, in the CCE1 case (see Appendix C).

Appendix C

Modulation frequencies

In this Appendix we derive the modulation frequencies from Section 3.2.1 by following a different approach. Let's start by specializing ourselves to the case in which there is only one nuclear spin in the bath, i.e. $n = 1$, and let's write the pure-dephasing Hamiltonian 1.3.3 in this case,

$$\mathcal{H} = DS_z^2 + \gamma_e B_z S_z + \gamma_1 B_z S_z + AS_z I_z + BS_z I_x. \tag{C.0.1}$$

The problem's Hilbert space has dimension $\dim(\mathscr{H}) = 3 \times 2 = 6$, so that the matrix representing Hamiltonian C.0.1 is a 6×6 one. We report the matrix in the following:

$$\begin{pmatrix} \omega_1 + \frac{\omega_I}{2} + \frac{A}{2} & B/2 & 0 & 0 & 0 & 0 \\ B/2 & \omega_1 - \frac{\omega_I}{2} - \frac{A}{2} & 0 & 0 & 0 & 0 \\ 0 & 0 & \frac{\omega_I}{2} & 0 & 0 & 0 \\ 0 & 0 & 0 & -\frac{\omega_I}{2} & 0 & 0 \\ 0 & 0 & 0 & 0 & \omega_{-1} + \frac{\omega_I}{2} - \frac{A}{2} & -B/2 \\ 0 & 0 & 0 & 0 & -B/2 & \omega_{-1} - \frac{\omega_I}{2} + \frac{A}{2} \end{pmatrix}. \tag{C.0.2}$$

This is a block-diagonal matrix with three quadrants, one for each of the three electron spin's energy levels. Consequently, the third quadrant is of no interest for us, whereas the second one is already diagonal. It remains

to diagonalize the first quadrant to be able to write down the first four eigenvalues, which are given by

$$\omega_1 + \frac{\Omega_I}{2} = E_1, \tag{C.0.3}$$

$$\omega_1 - \frac{\Omega_I}{2} = E_2, \tag{C.0.4}$$

$$\frac{\omega_I}{2} = E_3, \tag{C.0.5}$$

$$-\frac{\omega_I}{2} = E_4, \tag{C.0.6}$$

where Ω_I is defined in Eq. 3.2.12. Now, from Eq. B.0.3 we have the 2^{2N}, in this case 4, modulation frequencies, which are the following,

$$\omega_1 - \frac{\omega_I}{2} + \frac{\Omega_I}{2} = E_1 + E_4, \tag{C.0.7}$$

$$\omega_1 + \frac{\omega_I}{2} - \frac{\Omega_I}{2} = E_2 + E_3, \tag{C.0.8}$$

$$\omega_1 - \frac{\omega_I}{2} - \frac{\Omega_I}{2} = E_2 + E_4, \tag{C.0.9}$$

$$\omega_1 + \frac{\omega_I}{2} + \frac{\Omega_I}{2} = E_1 + E_3. \tag{C.0.10}$$

Eqs. C.0.7-C.0.10 are the relations we were looking for between the modulation frequencies and our system's eigenenergies. Furthermore, analogous relations valid in the case $n = N$ can be easily obtained by using induction considerations.

Bibliography

[1] Tsunenobu Kimoto and James A Cooper. *Fundamentals of silicon carbide technology: growth, characterization, devices and applications*. John Wiley & Sons, 2014.

[2] Katsuya Okamura and Ken Takayama. High frequency power supply with 3.3 kv sic-mosfets for accelerator application. In *Materials Science Forum*, volume 897, pages 685–688. Trans Tech Publ, 2017.

[3] Luciano FS Alves, Ruan CM Gomes, Pierre Lefranc, Raoni de A Pegado, Pierre-Olivier Jeannin, Benedito A Luciano, and Filipe V Rocha. Sic power devices in power electronics: An overview. In *2017 Brazilian Power Electronics Conference (COBEP)*, pages 1–8. IEEE, 2017.

[4] Stefania Castelletto and Alberto Boretti. Silicon carbide color centers for quantum applications. *Journal of Physics: Photonics*, 2(2):022001, 2020.

[5] Viktor Ivády, Krisztián Szász, Abram L Falk, Paul V Klimov, David J Christle, Erik Janzén, Igor A Abrikosov, David D Awschalom, and Adam Gali. Theoretical model of dynamic spin polarization of nuclei coupled to paramagnetic point defects in diamond and silicon carbide. *Physical Review B*, 92(11):115206, 2015.

[6] Debbie G Senesky, Babak Jamshidi, Kan Bun Cheng, and Albert P Pisano. Harsh environment silicon carbide sensors for health and performance monitoring of aerospace systems: A review. *IEEE Sensors Journal*, 9(11):1472–1478, 2009.

[7] Giuseppe Fisicaro, Corrado Bongiorno, Ioannis Deretzis, Filippo Giannazzo, Francesco La Via, Fabrizio Roccaforte, Marcin Zielinski, Massimo Zimbone, and Antonino La Magna. Genesis and evolution of extended defects: The role of evolving interface instabilities in cubic sic. *Applied Physics Reviews*, 7(2):021402, 2020.

[8] Francesco La Via, Massimo Zimbone, Corrado Bongiorno, Antonino La Magna, Giuseppe Fisicaro, Ioannis Deretzis, Viviana Scuderi, Cristiano Calabretta, Filippo Giannazzo, Marcin Zielinski, et al. New approaches and understandings in the growth of cubic silicon carbide. *Materials*, 14(18):5348, 2021.

[9] QZ Liu and SS Lau. A review of the metal–gan contact technology. *Solid-State Electronics*, 42(5):677–691, 1998.

[10] Ahmad Hassan, Yvon Savaria, and Mohamad Sawan. Gan integration technology, an ideal candidate for high-temperature applications: A review. *IEEE Access*, 6:78790–78802, 2018.

[11] Rongming Chu, Yu Cao, Mary Chen, Ray Li, and Daniel Zehnder. An experimental demonstration of gan cmos technology. *IEEE Electron Device Letters*, 37(3):269–271, 2016.

[12] I Deretzis, P Fiorenza, T Fazio, E Schilirò, R Lo Nigro, G Greco, G Fisicaro, F Roccaforte, and A La Magna. Aluminum frenkel defects cause hysteresis in al2o3/algan capacitors. *Journal of Applied Physics*, 132(16):165105, 2022.

[13] Yury Yu Illarionov, Theresia Knobloch, Markus Jech, Mario Lanza, Deji Akinwande, Mikhail I Vexler, Thomas Mueller, Max C Lemme,

Gianluca Fiori, Frank Schwierz, et al. Insulators for 2d nanoelectronics: the gap to bridge. *Nature communications*, 11(1):1–15, 2020.

[14] Mete Atatüre, Dirk Englund, Nick Vamivakas, Sang-Yun Lee, and Joerg Wrachtrup. Material platforms for spin-based photonic quantum technologies. *Nature Reviews Materials*, 3(5):38–51, 2018.

[15] Tommaso Fazio, Giuseppe Fisicaro, Ioannis Deretzis, Elisabetta Paladino, and Antonino La Magna. Computational study of the silicon vacancy in 3c-sic and perspectives for quantum technologies. In *Materials Science Forum*, volume 1062, pages 309–314. Trans Tech Publ, 2022.

[16] Tommaso Fazio, Giuseppe Fisicaro, Ioannis Deretzis, Elisabetta Paladino, and Antonino La Magna. Decoherence analysis of silicon vacancies in 3c-sic. *Submitted. Preprint at http://arxiv.org/abs/2211.00341*, 2022.

[17] W Schilling. Properties of frenkel defects. *Journal of nuclear materials*, 216:45–48, 1994.

[18] Hideo Hosono, Hiroshi Kawazoe, and Noriaki Matsunami. Experimental evidence for frenkel defect formation in amorphous sio 2 by electronic excitation. *Physical Review Letters*, 80(2):317, 1998.

[19] Joseph J Freedsman, Takashi Egawa, Yuya Yamaoka, Yoshiki Yano, Akinori Ubukata, Toshiya Tabuchi, and Koh Matsumoto. Normally-off al2o3/algan/gan mos-hemt on 8 in. si with low leakage current and high breakdown voltage (825 v). *Applied Physics Express*, 7(4):041003, 2014.

[20] Hosung Seo, Abram L Falk, Paul V Klimov, Kevin C Miao, Giulia Galli, and David D Awschalom. Quantum decoherence dynamics of divacancy spins in silicon carbide. *Nature communications*, 7(1):1–9, 2016.

[21] Abram L Falk, Bob B Buckley, Greg Calusine, William F Koehl, Viatcheslav V Dobrovitski, Alberto Politi, Christian A Zorman, Philip X-L Feng, and David D Awschalom. Polytype control of spin qubits in silicon carbide. *Nature communications*, 4(1):1–7, 2013.

[22] Paolo Giannozzi, Stefano Baroni, Nicola Bonini, Matteo Calandra, Roberto Car, Carlo Cavazzoni, Davide Ceresoli, Guido L Chiarotti, Matteo Cococcioni, Ismaila Dabo, et al. Quantum espresso: a modular and open-source software project for quantum simulations of materials. *Journal of physics: Condensed matter*, 21(39):395502, 2009.

[23] Chris J Pickard and Francesco Mauri. All-electron magnetic response with pseudopotentials: Nmr chemical shifts. *Physical Review B*, 63(24):245101, 2001.

[24] Jérémie Lefèvre, Jean-Marc Costantini, Didier Gourier, Stéphane Esnouf, and Guillaume Petite. Characterization of a silicon-related defect detected by its excited triplet state in electron-irradiated 3c-sic. *Physical Review B*, 83(7):075201, 2011.

[25] Viktor Ivády, Joel Davidsson, Nguyen Tien Son, Takeshi Ohshima, Igor A Abrikosov, and Adam Gali. Identification of si-vacancy related room-temperature qubits in 4 h silicon carbide. *Physical Review B*, 96(16):161114, 2017.

[26] Michel Bockstedte, Matthias Heid, and Oleg Pankratov. Signature of intrinsic defects in sic: Ab initio calculations of hyperfine tensors. *Physical Review B*, 67(19):193102, 2003.

[27] Charles P Slichter. *Principles of magnetic resonance*, volume 1. Springer Science & Business Media, 2013.

[28] E Paladino, YM Galperin, G Falci, and BL Altshuler. 1/f noise: Implications for solid-state quantum information. *Reviews of Modern Physics*, 86(2):361, 2014.

[29] G Falci, A D'arrigo, A Mastellone, and E Paladino. Initial decoherence in solid state qubits. *Physical review letters*, 94(16):167002, 2005.

[30] J Bergli, Yu M Galperin, and BL Altshuler. Decoherence in qubits due to low-frequency noise. *New Journal of Physics*, 11(2):025002, 2009.

[31] Semen Aleksandrovich Al'Tshuler and Boris Mikhaĭlovich Kozyrev. *Electron paramagnetic resonance*. Academic Press, 2013.

[32] Wen Yang and Ren-Bao Liu. Quantum many-body theory of qubit decoherence in a finite-size spin bath. *Physical Review B*, 78(8):085315, 2008.

[33] Jianjun Chen, Judong Zhang, Mingming Wang, and Ye Li. High-temperature hydrogen sensor based on platinum nanoparticle-decorated sic nanowire device. *Sensors and Actuators B: Chemical*, 201:402–406, 2014.

[34] Hind Ahmed, Hayder M Abduljalil, and Ahmed Hashim. Structural, optical and electronic properties of novel (pva–mgo)/sic nanocomposites films for humidity sensors. *Transactions on Electrical and Electronic Materials*, 20(3):218–232, 2019.

[35] Jianjun Su, Biao Gao, Zhendong Chen, Jijiang Fu, Weili An, Xiang Peng, Xuming Zhang, Lei Wang, Kaifu Huo, and Paul K Chu. Large-scale synthesis and mechanism of β-sic nanoparticles from rice husks by low-temperature magnesiothermic reduction. *ACS Sustainable Chemistry & Engineering*, 4(12):6600–6607, 2016.

[36] Yiyuan Wang, Shun Dong, Xiutao Li, Changqing Hong, and Xinghong Zhang. Synthesis, properties, and multifarious applications of sic nanoparticles: a review. *Ceramics International*, 2021.

[37] E Ringe, Richard P Van Duyne, and LD Marks. Wulff construction for alloy nanoparticles. *Nano letters*, 11(8):3399–3403, 2011.

[38] Ki Chul Kim, Bing Dai, J Karl Johnson, and David S Sholl. Assessing nanoparticle size effects on metal hydride thermodynamics using the wulff construction. *Nanotechnology*, 20(20):204001, 2009.

[39] Marco Masullo, Roberto Bergamaschini, Marco Albani, Thomas Kreiliger, Marco Mauceri, Danilo Crippa, Francesco La Via, Francesco Montalenti, Hans von Känel, and Leo Miglio. Growth and coalescence of 3c-sic on si (111) micro-pillars by a phase-field approach. *Materials*, 12(19):3223, 2019.

[40] K Sasaki, E Sakuma, S Misawa, S Yoshida, and S Gonda. High-temperature electrical properties of 3c-sic epitaxial layers grown by chemical vapor deposition. *Applied physics letters*, 45(1):72–73, 1984.

[41] Jian Yi, XiaoDong He, Yue Sun, and Yao Li. Electron beam-physical vapor deposition of sic/sio2 high emissivity thin film. *Applied surface science*, 253(9):4361–4366, 2007.

[42] Noraini Marsi, Burhanuddin Yeop Majlis, Faisal Mohd-Yasin, and Azrul Azlan Hamzah. The fabrication of back etching 3c-sic-on-si diaphragm employing koh+ ipa in mems capacitive pressure sensor. *Microsystem Technologies*, 21(8):1651–1661, 2015.

[43] Nathan Argaman and Guy Makov. Density functional theory: An introduction. *American Journal of Physics*, 68(1):69–79, 2000.

[44] P Hohenberg and WJPR Kohn. Density functional theory (dft). *Phys. Rev*, 136:B864, 1964.

[45] Walter Kohn and Lu Jeu Sham. Self-consistent equations including exchange and correlation effects. *Physical review*, 140(4A):A1133, 1965.

[46] C Stampfl and Ch G Van de Walle. Density-functional calculations for iii-v nitrides using the local-density approximation and the generalized gradient approximation. *Physical Review B*, 59(8):5521, 1999.

[47] John P Perdew, Kieron Burke, and Matthias Ernzerhof. Generalized gradient approximation made simple. *Phys. Rev. Lett.*, 77(18):3865, 1996.

[48] John P Perdew. Density functional theory and the band gap problem. *International Journal of Quantum Chemistry*, 28(S19):497–523, 1985.

[49] Carlo Adamo and Denis Jacquemin. The calculations of excited-state properties with time-dependent density functional theory. *Chemical Society Reviews*, 42(3):845–856, 2013.

[50] Jochen Heyd, Gustavo E Scuseria, and Matthias Ernzerhof. Hybrid functionals based on a screened coulomb potential. *The Journal of chemical physics*, 118(18):8207–8215, 2003.

[51] Douglas Andrade and Guilherme Colherinhas. A6h polypeptide membranes: Molecular dynamics simulation, giao-dft-nmr and td-dft spectroscopy analysis. *Journal of Molecular Liquids*, 316:113850, 2020.

[52] Philip J Hasnip, Keith Refson, Matt IJ Probert, Jonathan R Yates, Stewart J Clark, and Chris J Pickard. Density functional theory in the solid state. *Philosophical Transactions of the Royal Society A: Mathematical, Physical and Engineering Sciences*, 372(2011):20130270, 2014.

[53] Ben Hourahine, Bálint Aradi, Volker Blum, F Bonafé, A Buccheri, Cristopher Camacho, Caterina Cevallos, MY Deshaye, T Dumitrică,

A Dominguez, et al. Dftb+, a software package for efficient approximate density functional theory based atomistic simulations. *The Journal of chemical physics*, 152(12):124101, 2020.

[54] Jürgen Hafner. Ab-initio simulations of materials using vasp: Density-functional theory and beyond. *Journal of computational chemistry*, 29(13):2044–2078, 2008.

[55] Kari Laasonen, Roberto Car, Changyol Lee, and David Vanderbilt. Implementation of ultrasoft pseudopotentials in ab initio molecular dynamics. *Physical Review B*, 43(8):6796, 1991.

[56] G Kresse and J Hafner. Norm-conserving and ultrasoft pseudopotentials for first-row and transition elements. *Journal of Physics: Condensed Matter*, 6(40):8245, 1994.

[57] Georg Kresse and Daniel Joubert. From ultrasoft pseudopotentials to the projector augmented-wave method. *Physical review b*, 59(3):1758, 1999.

[58] Roberto Orlando, Roberto Dovesi, C Roetti, and VR Saunders. Ab initio hartree-fock calculations for periodic compounds: application to semiconductors. *Journal of Physics: Condensed Matter*, 2(38):7769, 1990.

[59] José M Soler, Emilio Artacho, Julian D Gale, Alberto García, Javier Junquera, Pablo Ordejón, and Daniel Sánchez-Portal. The siesta method for ab initio order-n materials simulation. *Journal of Physics: Condensed Matter*, 14(11):2745, 2002.

[60] Linu Malakkal, Barbara Szpunar, Juan Carlos Zuniga, Ravi Kiran Siripurapu, and Jerzy A Szpunar. First principles calculation of thermo-mechanical properties of thoria using quantum espresso. *International Journal of Computational Materials Science and Engineering*, 5(02):1650008, 2016.

[61] Paolo Giannozzi, Oliviero Andreussi, Thomas Brumme, Oana Bunau, M Buongiorno Nardelli, Matteo Calandra, Roberto Car, Carlo Cavazzoni, Davide Ceresoli, Matteo Cococcioni, et al. Advanced capabilities for materials modelling with quantum espresso. *Journal of physics: Condensed matter*, 29(46):465901, 2017.

[62] Taylor A Barnes, Thorsten Kurth, Pierre Carrier, Nathan Wichmann, David Prendergast, Paul RC Kent, and Jack Deslippe. Improved treatment of exact exchange in quantum espresso. *Computer Physics Communications*, 214:52–58, 2017.

[63] F Roccaforte, P Fiorenza, G Greco, M Vivona, R Lo Nigro, F Giannazzo, A Patti, and M Saggio. Recent advances on dielectrics technology for sic and gan power devices. *Appl. Surf. Sci.*, 301:9–18, 2014.

[64] Emanuela Schilirò, Patrick Fiorenza, Corrado Bongiorno, Corrado Spinella, Salvatore Di Franco, Giuseppe Greco, Raffaella Lo Nigro, and Fabrizio Roccaforte. Correlating electron trapping and structural defects in al2o3 thin films deposited by plasma enhanced atomic layer deposition. *AIP Adv.*, 10(12):125017, 2020.

[65] D Bisi, SH Chan, X Liu, R Yeluri, S Keller, M Meneghini, G Meneghesso, E Zanoni, and UK Mishra. On trapping mechanisms at oxide-traps in al2o3/gan metal-oxide-semiconductor capacitors. *Appl. Phys. Lett.*, 108(11):112104, 2016.

[66] AY Polyakov, NB Smirnov, AV Govorkov, AV Markov, AM Dabiran, AM Wowchak, AV Osinsky, B Cui, PP Chow, and SJ Pearton. Deep traps responsible for hysteresis in capacitance-voltage characteristics of algan/ gan heterostructure transistors. *Appl. Phys. Lett.*, 91(23):232116, 2007.

[67] LE Byrum, G Ariyawansa, RC Jayasinghe, N Dietz, AGU Perera, SG Matsik, IT Ferguson, A Bezinger, and HC Liu. Capacitance hys-

teresis in gan/algan heterostructures. *J. Appl. Phys.*, 105(2):023709, 2009.

[68] Chihoko Mizue, Yujin Hori, Marcin Miczek, and Tamotsu Hashizume. Capacitance–voltage characteristics of al2o3/algan/gan structures and state density distribution at al2o3/algan interface. *Jpn. J. Appl. Phys.*, 50(2R):021001, 2011.

[69] Richard Car and Mark Parrinello. Unified approach for molecular dynamics and density-functional theory. *Phys. Rev. Lett.*, 55(22):2471, 1985.

[70] Jon M Andersson, Zs Czigány, P Jin, and Ulf Helmersson. Microstructure of α-alumina thin films deposited at low temperatures on chromia template layers. *J. Vac. Sci. Technol. A*, 22(1):117–121, 2004.

[71] Roel Prins. On the structure of γ-al2o3. *J. Catal.*, 392:336–346, 2020.

[72] Jürg Hutter. Car–parrinello molecular dynamics. *Wiley Interdisciplinary Reviews: Computational Molecular Science*, 2(4):604–612, 2012.

[73] Mark E Tuckerman, Dominik Marx, Michael L Klein, and Michele Parrinello. Efficient and general algorithms for path integral car–parrinello molecular dynamics. *The Journal of chemical physics*, 104(14):5579–5588, 1996.

[74] Nikos L Doltsinis and Dominik Marx. Nonadiabatic car-parrinello molecular dynamics. *Physical review letters*, 88(16):166402, 2002.

[75] Kari Laasonen, Alfredo Pasquarello, Roberto Car, Changyol Lee, and David Vanderbilt. Car-parrinello molecular dynamics with vanderbilt ultrasoft pseudopotentials. *Physical Review B*, 47(16):10142, 1993.

[76] David Vanderbilt. Soft self-consistent pseudopotentials in a generalized eigenvalue formalism. *Phys. Rev. B*, 41(11):7892, 1990.

[77] Shuichi Nosé. A unified formulation of the constant temperature molecular dynamics methods. *J. Chem. Phys.*, 81(1):511–519, 1984.

[78] Loup Verlet. Computer "experiments" on classical fluids. i. thermodynamical properties of lennard-jones molecules. *Phys. Rev.*, 159(1):98, 1967.

[79] Hendrik J Monkhorst and James D Pack. Special points for brillouin-zone integrations. *Phys. Rev. B*, 13(12):5188, 1976.

[80] Carlo Adamo and Vincenzo Barone. Toward reliable density functional methods without adjustable parameters: The pbe0 model. *J. Chem. Phys.*, 110(13):6158–6170, 1999.

[81] Matthias Ernzerhof and Gustavo E Scuseria. Assessment of the perdew–burke–ernzerhof exchange-correlation functional. *J. Chem. Phys.*, 110(11):5029–5036, 1999.

[82] Hannes Jónsson, Greg Mills, and Karsten W Jacobsen. Nudged elastic band method for finding minimum energy paths of transitions. In *Classical and quantum dynamics in condensed phase simulations*, pages 385–404. World Scientific, 1998.

[83] Daniel Sheppard, Penghao Xiao, William Chemelewski, Duane D Johnson, and Graeme Henkelman. A generalized solid-state nudged elastic band method. *The Journal of chemical physics*, 136(7):074103, 2012.

[84] Graeme Henkelman, Blas P Uberuaga, and Hannes Jónsson. A climbing image nudged elastic band method for finding saddle points and minimum energy paths. *J. Chem. Phys.*, 113(22):9901–9904, 2000.

[85] Patrick Fiorenza, Emanuela Schilirò, Giuseppe Greco, Marilena Vivona, Marco Cannas, Filippo Giannazzo, Raffaella Lo Nigro, and Fabrizio Roccaforte. Temperature and time dependent electron trapping in al2o3 thin films onto algan/gan heterostructures. *Appl. Surf. Sci.*, 579:152136, 2022.

[86] Leonid Bloch, Yaron Kauffmann, and Boaz Pokroy. Size effect on the short range order and the crystallization of nanosized amorphous alumina. *Cryst. Growth Des.*, 14(8):3983–3989, 2014.

[87] JR Weber, Anderson Janotti, and CG Van de Walle. Native defects in al 2 o 3 and their impact on iii-v/al 2 o 3 metal-oxide-semiconductor-based devices. *J. Appl. Phys.*, 109(3):033715, 2011.

[88] Minseok Choi, Anderson Janotti, and Chris G Van de Walle. Native point defects and dangling bonds in α-al2o3. *J. Appl. Phys.*, 113(4):044501, 2013.

[89] Sung Keun Lee, Sung Bo Lee, Sun Young Park, Yoo Soo Yi, and Chi Won Ahn. Structure of amorphous aluminum oxide. *Phys. Rev. Lett.*, 103(9):095501, 2009.

[90] Sung Keun Lee and Saebom Ryu. Probing of triply coordinated oxygen in amorphous al2o3. *J. Phys. Chem. Lett.*, 9(1):150–156, 2018.

[91] Hiroyoshi Momida and Takahisa Ohno. Bistability and metastability of oxygen vacancies in amorphous al2o3: A possible origin of resistance switching mechanism. *Appl. Phys. Lett.*, 117(10):103504, 2020.

[92] Grzegorz Chalasinski and Malgorzata M Szczesniak. Origins of structure and energetics of van der waals clusters from ab initio calculations. *Chemical Reviews*, 94(7):1723–1765, 1994.

[93] Krisztián Szász, Tamás Hornos, Martijn Marsman, and Adam Gali. Hyperfine coupling of point defects in semiconductors by hybrid density functional calculations: The role of core spin polarization. *Physical Review B*, 88(7):075202, 2013.

[94] Viktor Ivády, Tamás Simon, Jeronimo R Maze, IA Abrikosov, and Adam Gali. Pressure and temperature dependence of the zero-field splitting in the ground state of nv centers in diamond: A first-principles study. *Physical Review B*, 90(23):235205, 2014.

[95] Fattah Sakuldee and Łukasz Cywiński. Characterization of a quasistatic environment with a qubit. *Physical Review A*, 99(6):062113, 2019.

[96] Brian Harold Bransden and Charles Jean Joachain. *Physics of atoms and molecules*. Pearson Education India, 2003.

[97] Thibault Charpentier. The paw/gipaw approach for computing nmr parameters: A new dimension added to nmr study of solids. *Solid state nuclear magnetic resonance*, 40(1):1–20, 2011.

[98] Ivan Girotto, Nicola Varini, Filippo Spiga, Carlo Cavazzoni, Davide Ceresoli, Layla Martin-Samos, and Tommaso Gorni. *Enabling of quantum espresso to petascale scientific challenges*. PRACE, 2012.

[99] Nicola Varini, Davide Ceresoli, Layla Martin-Samos, Ivan Girotto, and Carlo Cavazzoni. Enhancement of dft-calculations at petascale: nuclear magnetic resonance, hybrid density functional theory and car–parrinello calculations. *Computer Physics Communications*, 184(8):1827–1833, 2013.

[100] He Ma, Marco Govoni, and Giulia Galli. Pyzfs: A python package for first-principles calculations of zero-field splitting tensors. *Journal of Open Source Software*, 5(47):2160, 2020.

[101] Alexei V Arbuznikov, Juha Vaara, and Martin Kaupp. Relativistic spin-orbit effects on hyperfine coupling tensors by density-functional theory. *The Journal of chemical physics*, 120(5):2127–2139, 2004.

[102] Walter Kohn, Axel D Becke, and Robert G Parr. Density functional theory of electronic structure. *The Journal of Physical Chemistry*, 100(31):12974–12980, 1996.

[103] Jianqi Xi, Bin Liu, Yanwen Zhang, and William J Weber. Ab initio study of point defects near stacking faults in 3c-sic. *Computational Materials Science*, 123:131–138, 2016.

[104] DR Hamann, M Schlüter, and C Chiang. Norm-conserving pseudopotentials. *Physical Review Letters*, 43(20):1494, 1979.

[105] Christoph Freysoldt, Blazej Grabowski, Tilmann Hickel, Jörg Neugebauer, Georg Kresse, Anderson Janotti, and Chris G Van de Walle. First-principles calculations for point defects in solids. *Reviews of modern physics*, 86(1):253, 2014.

[106] Michel Bockstedte, Alexander Mattausch, and Oleg Pankratov. Ab initio study of the migration of intrinsic defects in 3 c- sic. *Physical Review B*, 68(20):205201, 2003.

[107] Takuji Oda, Yanwen Zhang, and William J Weber. Study of intrinsic defects in 3c-sic using first-principles calculation with a hybrid functional. *The Journal of chemical physics*, 139(12):124707, 2013.

[108] L Torpo, Risto M Nieminen, KE Laasonen, and S Pöykkö. Silicon vacancy in sic: a high-spin state defect. *Applied physics letters*, 74(2):221–223, 1999.

[109] Adolf Schöner, Michael Krieger, Gerhard Pensl, Masayuki Abe, and Hiroyuki Nagasawa. Fabrication and characterization of 3c-sic-based mosfets. *Chemical Vapor Deposition*, 12(8-9):523–530, 2006.

[110] J Isoya, T Umeda, N Mizuochi, NT Son, Erik Janzén, and T Ohshima. Epr identification of intrinsic defects in sic. *physica status solidi (b)*, 245(7):1298–1314, 2008.

[111] Mt Wagner, NQ Thinh, NT Son, WM Chen, Erik Janzén, PG Baranov, EN Mokhov, Christer Hallin, and JL Lindström. Ligand hyperfine interaction at the neutral silicon vacancy in 4h-and 6 h- sic. *Physical Review B*, 66(15):155214, 2002.

[112] S Filipp, AF Van Loo, M Baur, L Steffen, and A Wallraff. Preparation of subradiant states using local qubit control in circuit qed. *Physical Review A*, 84(6):061805, 2011.

[113] Chandrasekhar Ramanathan, Nicolas Boulant, Zhiying Chen, David G Cory, Isaac Chuang, and Matthias Steffen. Nmr quantum information processing. *Quantum Information Processing*, 3(1):15–44, 2004.

[114] Lieven MK Vandersypen and Isaac L Chuang. Nmr techniques for quantum control and computation. *Reviews of modern physics*, 76(4):1037, 2005.

[115] Juan José García-Ripoll, Peter Zoller, and J Ignacio Cirac. Speed optimized two-qubit gates with laser coherent control techniques for ion trap quantum computing. *Physical Review Letters*, 91(15):157901, 2003.

[116] You-Ji Fan, Zhen-Fei Zheng, Yu Zhang, Dao-Ming Lu, and Chui-Ping Yang. One-step implementation of a multi-target-qubit controlled phase gate with cat-state qubits in circuit qed. *Frontiers of Physics*, 14(2):1–9, 2019.

[117] Vanita Srinivasa, Jacob M Taylor, and Charles Tahan. Entangling distant resonant exchange qubits via circuit quantum electrodynamics. *Physical Review B*, 94(20):205421, 2016.

[118] Jean Baum, Michael Munowitz, Allen N Garroway, and Alex Pines. Multiple-quantum dynamics in solid state nmr. *The Journal of chemical physics*, 83(5):2015–2025, 1985.

[119] Jens Koch, M Yu Terri, Jay Gambetta, Andrew A Houck, David I Schuster, Johannes Majer, Alexandre Blais, Michel H Devoret, Steven M Girvin, and Robert J Schoelkopf. Charge-insensitive qubit design derived from the cooper pair box. *Physical Review A*, 76(4):042319, 2007.

[120] A Soare, H Ball, D Hayes, J Sastrawan, MC Jarratt, JJ McLoughlin, X Zhen, TJ Green, and MJ Biercuk. Experimental noise filtering by quantum control. *Nature Physics*, 10(11):825–829, 2014.

[121] Todd J Green, Jarrah Sastrawan, Hermann Uys, and Michael J Biercuk. Arbitrary quantum control of qubits in the presence of universal noise. *New Journal of Physics*, 15(9):095004, 2013.

[122] Santiago Hernández-Gómez and Nicole Fabbri. Quantum control for nanoscale spectroscopy with diamond nitrogen-vacancy centers: a short review. *Frontiers in Physics*, 8:610868, 2021.

[123] M Hatano and T Iwasaki. Device engineering for diamond quantum sensors. In *2019 IEEE International Electron Devices Meeting (IEDM)*, pages 26–3. IEEE, 2019.

[124] Debraj Modak, Abhijit Kundu, and Moumita Mukherjee. Multiple-graphene layer based p++–n–n—n++ device on si/3c-sic (100) substrate: a highly sensitive visible photo-sensor. *Semiconductor Science and Technology*, 35(9):095025, 2020.

[125] Hoang-Phuong Phan, Karen M Dowling, Tuan Khoa Nguyen, Toan Dinh, Debbie G Senesky, Takahiro Namazu, Dzung Viet Dao, and Nam-Trung Nguyen. Highly sensitive pressure sensors employing

3c-sic nanowires fabricated on a free standing structure. *Materials & Design*, 156:16–21, 2018.

[126] Stefania Castelletto, Brett C Johnson, and Alberto Boretti. Quantum effects in silicon carbide hold promise for novel integrated devices and sensors. *Advanced Optical Materials*, 1(9):609–625, 2013.

[127] H Okumura, H Itoh, I Nashiyama, S Yamasaki, S Misawa, and S Yoshida. Characterization of 3c-sic epilayers by pulsed electron spin resonance. *Materials Science and Engineering: B*, 11(1-4):31–34, 1992.

[128] Arthur Schweiger and Gunnar Jeschke. *Principles of pulse electron paramagnetic resonance*. Oxford University Press on Demand, 2001.

[129] Ian Coddington, William C Swann, and Nathan R Newbury. Time-domain spectroscopy of molecular free-induction decay in the infrared. *Optics letters*, 35(9):1395–1397, 2010.

[130] DI Hoult and NS Ginsberg. The quantum origins of the free induction decay signal and spin noise. *Journal of Magnetic Resonance*, 148(1):182–199, 2001.

[131] S Bengtsson, Esben Witting Larsen, D Kroon, S Camp, M Miranda, CL Arnold, A L'Huillier, KJ Schafer, MB Gaarde, L Rippe, et al. Space–time control of free induction decay in the extreme ultraviolet. *Nature Photonics*, 11(4):252–258, 2017.

[132] Axel Schenzle, NC Wong, and Richard G Brewer. Oscillatory free-induction decay. *Physical Review A*, 21(3):887, 1980.

[133] L_G Rowan, EL Hahn, and WB Mims. Electron-spin-echo envelope modulation. *Physical Review*, 137(1A):A61, 1965.

[134] Jiapei Shu, Gongtao Wu, Yao Guo, Bo Liu, Xianlong Wei, and Qing Chen. The intrinsic origin of hysteresis in mos 2 field effect transistors. *Nanoscale*, 8(5):3049–3056, 2016.

[135] Xianglong Yuan and Linn W Hobbs. Modeling chemical and topological disorder in irradiation-amorphized silicon carbide. *Nuclear Instruments and Methods in Physics Research Section B: Beam Interactions with Materials and Atoms*, 191(1-4):74–82, 2002.

[136] Yanwen Zhang, Ritesh Sachan, Olli H Pakarinen, Matthew F Chisholm, Peng Liu, Haizhou Xue, and William J Weber. Ionization-induced annealing of pre-existing defects in silicon carbide. *Nature communications*, 6(1):1–7, 2015.

[137] H Kraus, VA Soltamov, F Fuchs, D Simin, A Sperlich, PG Baranov, GV Astakhov, and Vladimir Dyakonov. Magnetic field and temperature sensing with atomic-scale spin defects in silicon carbide. *Scientific reports*, 4(1):1–8, 2014.

[138] Lance L Snead, Yutai Katoh, Takaaki Koyanagi, and Kurt Terrani. Stored energy release in neutron irradiated silicon carbide. *Journal of Nuclear Materials*, 514:181–188, 2019.

[139] Kun Xue, Li-Sha Niu, and Hui-Ji Shi. Mechanical properties of amorphous silicon carbide. *Silicon carbide-materials, processing and applications in electronic devices*, 2011.

[140] Mun Teng Soo, Kuan Yew Cheong, and Ahmad Fauzi Mohd Noor. Advances of sic-based mos capacitor hydrogen sensors for harsh environment applications. *Sensors and Actuators B: Chemical*, 151(1):39–55, 2010.

[141] Mutsunori Uenuma, Kiyoshi Takahashi, Sho Sonehara, Yuta Tominaga, Yuta Fujimoto, Yasuaki Ishikawa, and Yukiharu Uraoka. Influence of carbon impurities and oxygen vacancies in al2o3

film on al2o3/gan mos capacitor characteristics. *AIP Advances*, 8(10):105103, 2018.

[142] M. D. Groner, F. H. Fabreguette, J. W. Elam, and S. M. George. Low-temperature al2o3 atomic layer deposition. *Chem. Mater*, 16(4):639–645, 2004.

[143] Emanuela Schilirò, Patrick Fiorenza, Giuseppe Greco, Francesca Monforte, Guglielmo Guido Condorelli, Fabrizio Roccaforte, Filippo Giannazzo, and Raffaella Lo Nigro. Early growth stages of aluminum oxide (al2o3) insulating layers by thermal-and plasma-enhanced atomic layer deposition on algan/gan heterostructures. *ACS Appl. Electron. Mater.*, 4(1):406–415, 2022.

[144] Katsuyuki Matsunaga, Tomohito Tanaka, Takahisa Yamamoto, and Yuichi Ikuhara. First-principles calculations of intrinsic defects in al 2 o 3. *Phys. Rev. B*, 68(8):085110, 2003.

[145] Zhendong Guo, Francesco Ambrosio, and Alfredo Pasquarello. Oxygen defects in amorphous al2o3: A hybrid functional study. *Appl. Phys. Lett.*, 109(6):062903, 2016.

[146] Gonzalo Gutierrez and Börje Johansson. Molecular dynamics study of structural properties of amorphous al 2 o 3. *Phys. Rev. B*, 65(10):104202, 2002.

[147] Priya Vashishta, Rajiv K Kalia, Aiichiro Nakano, and José Pedro Rino. Interaction potentials for alumina and molecular dynamics simulations of amorphous and liquid alumina. *J. Appl. Phys.*, 103(8):083504, 2008.

[148] Matthias J Young, Nicholas M Bedford, Angel Yanguas-Gil, Steven Letourneau, Matthew Coile, David J Mandia, Bachir Aoun, Andrew S Cavanagh, Steven M George, and Jeffrey W Elam. Probing the atomic-scale structure of amorphous aluminum oxide grown by

atomic layer deposition. *ACS Appl. Mater. Interfaces*, 12(20):22804–22814, 2020.

[149] Philip Warren Anderson. Localized magnetic states in metals. *Physical Review*, 124(1):41, 1961.

[150] Antonino La Magna and Ioannis Deretzis. Phonon driven nonlinear electrical behavior in molecular devices. *Phys. Rev. Lett.*, 99(13):136404, 2007.

[151] AS Alexandrov and AM Bratkovsky. Memory effect in a molecular quantum dot with strong electron-vibron interaction. *Physical Review B*, 67(23):235312, 2003.

[152] IG Lang and Yu A Firsov. Kinetic theory of semiconductors with low mobility. *Sov. Phys. JETP*, 16(5):1301, 1963.

[153] Lewis S Ramsdell. Studies on silicon carbide. *American Mineralogist: Journal of Earth and Planetary Materials*, 32(1-2):64–82, 1947.

[154] Xu She, Alex Q Huang, Oscar Lucia, and Burak Ozpineci. Review of silicon carbide power devices and their applications. *IEEE Transactions on Industrial Electronics*, 64(10):8193–8205, 2017.

[155] Alexander Lohrmann, BC Johnson, JC McCallum, and Stefania Castelletto. A review on single photon sources in silicon carbide. *Reports on Progress in Physics*, 80(3):034502, 2017.

[156] Joel Davidsson, Viktor Ivády, Rickard Armiento, NT Son, Adam Gali, and Igor A Abrikosov. First principles predictions of magneto-optical data for semiconductor point defect identification: the case of divacancy defects in 4h–sic. *New Journal of Physics*, 20(2):023035, 2018.

[157] Krisztián Szász, Viktor Ivády, Igor A Abrikosov, Erik Janzén, Michel Bockstedte, and Adam Gali. Spin and photophysics of carbon-antisite vacancy defect in 4 h silicon carbide: A potential quantum bit. *Physical Review B*, 91(12):121201, 2015.

[158] Matthias Widmann, Matthias Niethammer, Dmitry Yu Fedyanin, Igor A Khramtsov, Torsten Rendler, Ian D Booker, Jawad Ul Hassan, Naoya Morioka, Yu-Chen Chen, Ivan G Ivanov, et al. Electrical charge state manipulation of single silicon vacancies in a silicon carbide quantum optoelectronic device. *Nano letters*, 19(10):7173–7180, 2019.

[159] WM Witzel and S Das Sarma. Quantum theory for electron spin decoherence induced by nuclear spin dynamics in semiconductor quantum computer architectures: Spectral diffusion of localized electron spins in the nuclear solid-state environment. *Physical Review B*, 74(3):035322, 2006.

[160] Wang Yao, Ren-Bao Liu, and LJ Sham. Theory of electron spin decoherence by interacting nuclear spins in a quantum dot. *Physical Review B*, 74(19):195301, 2006.

[161] SK Saikin, Wang Yao, and LJ Sham. Single-electron spin decoherence by nuclear spin bath: Linked-cluster expansion approach. *Physical Review B*, 75(12):125314, 2007.

[162] Mykyta Onizhuk, Kevin C Miao, Joseph P Blanton, He Ma, Christopher P Anderson, Alexandre Bourassa, David D Awschalom, and Giulia Galli. Probing the coherence of solid-state qubits at avoided crossings. *PRX Quantum*, 2(1):010311, 2021.

[163] Elliott Fraval, MJ Sellars, and JJ Longdell. Dynamic decoherence control of a solid-state nuclear-quadrupole qubit. *Physical review letters*, 95(3):030506, 2005.

[164] Budaraju S Murty, P Shankar, Baldev Raj, BB Rath, and James Murday. *Textbook of nanoscience and nanotechnology*. Springer Science & Business Media, 2013.

[165] Lei Fan, Jin Xu, and Yihong Hong. Defects in graphene-based heterostructures: topological and geometrical effects. *RSC advances*, 12(11):6772–6782, 2022.

[166] Krishnendu Chatterjee, Sreerupa Sarkar, K Jagajjanani Rao, and Santanu Paria. Core/shell nanoparticles in biomedical applications. *Advances in colloid and interface science*, 209:8–39, 2014.

[167] Antonio Minopoli, Adriano Acunzo, Bartolomeo Della Ventura, and Raffaele Velotta. Nanostructured surfaces as plasmonic biosensors: A review. *Advanced Materials Interfaces*, 9(2):2101133, 2022.

[168] Loïc Rondin, Jean-Philippe Tetienne, Thomas Hingant, Jean-François Roch, Patrick Maletinsky, and Vincent Jacques. Magnetometry with nitrogen-vacancy defects in diamond. *Reports on progress in physics*, 77(5):056503, 2014.

[169] Georg Kucsko, Peter C Maurer, Norman Ying Yao, MICHAEL Kubo, Hyun Jong Noh, Po Kam Lo, Hongkun Park, and Mikhail D Lukin. Nanometre-scale thermometry in a living cell. *Nature*, 500(7460):54–58, 2013.

[170] Ettore Bernardi, Richard Nelz, Selda Sonusen, and Elke Neu. Nanoscale sensing using point defects in single-crystal diamond: recent progress on nitrogen vacancy center-based sensors. *Crystals*, 7(5):124, 2017.

[171] Vibhu Jindal and Fatemeh Shahedipour-Sandvik. Theoretical prediction of gan nanostructure equilibrium and nonequilibrium shapes. *Journal of Applied Physics*, 106(8):083115, 2009.

[172] LD Marks and L Peng. Nanoparticle shape, thermodynamics and kinetics. *Journal of Physics: Condensed Matter*, 28(5):053001, 2016.

[173] Christina Boukouvala, Joshua Daniel, and Emilie Ringe. Approaches to modelling the shape of nanocrystals. *Nano convergence*, 8(1):1–15, 2021.

[174] Michelle L Personick, Mark R Langille, Jian Zhang, and Chad A Mirkin. Shape control of gold nanoparticles by silver underpotential deposition. *Nano letters*, 11(8):3394–3398, 2011.

[175] Bo Li, John Lowengrub, Andreas Ratz, and Axel Voigt. Geometric evolution laws for thin crystalline films: modeling and numerics. *Communications in Computational Physics*, 6(3):433, 2009.

[176] Marco Salvalaglio, Rainer Backofen, Roberto Bergamaschini, Francesco Montalenti, and Axel Voigt. Faceting of equilibrium and metastable nanostructures: a phase-field model of surface diffusion tackling realistic shapes. *Crystal Growth & Design*, 15(6):2787–2794, 2015.

[177] Marco Albani, Lea Ghisalberti, Roberto Bergamaschini, Martin Friedl, Marco Salvalaglio, Axel Voigt, Francesco Montalenti, Gözde Tütüncüoglu, Anna Fontcuberta i Morral, and Leo Miglio. Growth kinetics and morphological analysis of homoepitaxial gaas fins by theory and experiment. *Physical Review Materials*, 2(9):093404, 2018.

[178] Marco Albani, Roberto Bergamaschini, Marco Salvalaglio, Axel Voigt, Leo Miglio, and Francesco Montalenti. Competition between kinetics and thermodynamics during the growth of faceted crystal by phase field modeling. *physica status solidi (b)*, 256(7):1800518, 2019.

[179] Emilie Ringe, Richard P Van Duyne, and Laurence D Marks. Kinetic and thermodynamic modified wulff constructions for twinned

nanoparticles. *The Journal of Physical Chemistry C*, 117(31):15859–15870, 2013.

[180] Sergey N Filimonov. Ab initio calculations of absolute surface energies of clean and hydrogen covered 3c-sic (001),(110) and (111) surfaces. In *Materials Science Forum*, volume 821, pages 363–366. Trans Tech Publ, 2015.

[181] Henrik Andersen Sveinsson, Anders Hafreager, Rajiv K Kalia, Aiichiro Nakano, Priya Vashishta, and Anders Malthe-Sørenssen. Direct atomic simulations of facet formation and equilibrium shapes of sic nanoparticles. *Crystal Growth & Design*, 20(4):2147–2152, 2020.

[182] J-C Jaskula, Kasturi Saha, Ashok Ajoy, Daniel J Twitchen, Matthew Markham, and Paola Cappellaro. Cross-sensor feedback stabilization of an emulated quantum spin gyroscope. *Physical Review Applied*, 11(5):054010, 2019.

[183] Jens M Boss, KS Cujia, Jonathan Zopes, and Christian L Degen. Quantum sensing with arbitrary frequency resolution. *Science*, 356(6340):837–840, 2017.

[184] Georgios D Barmparis, Zbigniew Lodziana, Nuria Lopez, and Ioannis N Remediakis. Nanoparticle shapes by using wulff constructions and first-principles calculations. *Beilstein journal of nanotechnology*, 6(1):361–368, 2015.

[185] Jianxun Xu, Yoshitaka Shingaya, Yuliang Zhao, and Tomonobu Nakayama. In situ, controlled and reproducible attachment of carbon nanotubes onto conductive afm tips. *Applied Surface Science*, 335:11–16, 2015.

[186] Sumin Choi, Victor Leong, Gandhi Alagappan, and Leonid Krivitsky. Enhancing optical readout from diamond afm tips for quantum nanosensing. *ACS Photonics*, 5(11):4244–4248, 2018.

[187] Shaorong Du and Yangmin Li. Micromanipulation based on afm: Probe tip selection. In *2007 7th IEEE Conference on Nanotechnology (IEEE NANO)*, pages 506–510. IEEE, 2007.

[188] Mykyta Onizhuk and Giulia Galli. Pycce: A python package for cluster correlation expansion simulations of spin qubit dynamics. *Advanced Theory and Simulations*, 4(11):2100254, 2021.

Acknowledgements

I would like to thank my Tutors for their help and guidance throughout the PhD. I thank my parents for their empathy and comprehension, and in general all of my friends and family. Last but not least, I sincerely thank my girlfriend for her continuous support and love through these years in CT.

We acknowledge the Italian Ministry for University and Research (MUR) in the framework of the National Project PON EleGaNTe (Electronics on GaN-based Technologies, n. ARS01_01007) for partial financial support. T.F. acknowledges a fruitful conversation and exchange of emails with Mykyta Onizhuk from the group of Giulia Galli. A special thank you goes also to Dr. Davide Ceresoli, from the CNR-SCITEC institute, for his clarification on the calculation of the ^{29}Si and ^{13}C hyperfine parameters through the QE-GIPAW code.